STRAIN RELAXATION AND SOLID PHASE EPITAXIAL REGROWTH IN ION IMPLANTED STRAINED SILICON AND STRAINED SILICON GERMANIUM

By

MICHELLE S. PHEN

A DISSERTATION PRESENTED TO THE GRADUATE SCHOOL
OF THE UNIVERSITY OF FLORIDA IN PARTIAL FULFILLMENT
OF THE REQUIREMENTS FOR THE DEGREE OF
DOCTOR OF PHILOSOPHY

UNIVERSITY OF FLORIDA

2008

In loving memory of my grandfather and fellow engineer, Jack A. D'Sousa

ACKNOWLEDGMENTS

I acknowledge the Semiconductor Research Corporation (SRC) and Intel/SRC scholarship for financial support for this work and my graduate studies. To all of my industrial liaisons who have played a vital role in my professional development and have extended assistance with acquisition of materials and implants, I extend the utmost gratitude to Lenny Rubin, Hans Weijtmans, and Karuppanan Sekar. I am also indebted to A.N. Larsen and J.L. Hansen at the University of Aarhus, Denmark for growing the strained Si on relaxed SiGe films. I also thank my committee member, Kevin Jones, Mark Law, Stephen Pearton, Valentin Craciun, and Ant Ural for their support.

I extend my appreciation to all the member of the SWAMP group whom were always willing to assist and nurture me as a young researcher. I thank Scott Thompson for many helpful discussion regarding industry and future prospects. I especially thank Robert Crosby for mentoring me, Renata Camillo-Castillo for her friendship and assistance with perfecting my WBDF imaging skills, Erik Kuryliw and Mark Clark with assistance in developing my first research project. I also thank Ljubo Radic for his friendship and assistance with Floops, Chad Lindfors and Jian Chen for teaching me how to use the Hall system, Heather Randall, Nicole Staszkiewicz, Jeannette Jacques, and Diane Hickey for their friendship and encouragement during the most challenging years of my studies. Furthermore, I thank Tony Saavedra and Danny Zeenberg for many helpful discussions and their support along the way. I also thank Sam Moore for editing this document and for his support, encouragement, and friendship throughout the years. I thank the current members of the group who have fostered a pleasant working environment both in the lab and the office. These members include David Horton, Saurabh Morarka, Nick Rudawski, Leah Edelman, Nicole Rowsey, Sidan Jin, Ray Holzworth, and Lucia Romano.

During the course of my studies, I held two internships with Texas Instruments, Inc. I meet a number of people there who have influenced me and have contributed to my professional growth. I thank the following who work for the High Performance Analog (HPA) packaging group: Tony Coyle and Jeffrey Holloway for mentoring me and teaching me so much about both package development and time management, and KK for his encouragement and inspiration. I also thank my former co-worker at Silicon Technology Development (SiTD). They include Hans Weijtmans and Mark Visokay for being great mentors, and Elizabeth Marley-Koontz and Majid Mansoori for many helpful discussions regarding future experiments and techniques.

In the course of my experiments I used a variety of characterization methods at Major Analytical Instrumentation Center (MAIC). The MAIC staff has always been very helpful and I extend my deepest appreciation. I especially thank, Amelia Dempere, the director of MAIC, Kerry Siebein for assistance and training on the TEMs, Jerry Bourne for assistance with the FIB, Valentin Craciun for many helpful discussion and training on new analysis methods using the X'Pert system, and finally, Rosabel Ruiz for assistant with administrative matters at MAIC.

Finally, I thank my family for their love and encouragement, especially my parents for always believing that I could accomplish anything.

TABLE OF CONTENTS

APPENDIX

LIST OF TABLES

LIST OF FIGURES

Abstract of Dissertation Presented to the Graduate School
of the University of Florida in Partial Fulfillment of the
Requirements for the Degree of Doctor of Philosophy

STRAIN RELAXATION AND SOLID PHASE EPITAXIAL REGROWTH IN ION IMPLANTED STRAINED SILICON AND STRAINED SILICON GERMANIUM

By

Michelle Phen

May 2008

Chair: Kevin Jones
Major: Materials Science and Engineering

The relaxation process of ion-implanted strained silicon films and strained $Si_{1-x}Ge_x$ alloys was studied to determine the magnitude of critical strain necessary for the breakdown of solid phase epitaxial regrowth in both biaxial tension and compression. Tensile strained silicon layers 50 nm thick were grown via Molecular Beam Epitaxy on relaxed $Si_{1-x}Ge_x$ virtual substrates. Substrate alloy compositions ranged from 10 to 30% Ge. Compressively strained 50 nm $Si_{1-x}Ge_x$ layers were grown on Si substrate via Chemical Vapor Deposition with Ge compositions ranging from 16 to 26%. All samples underwent a 5, 12, or 18 keV Si^+ implant at a fluence of $1x10^{15}$ atoms/cm^2 to generate amorphous layers ~15, 30, or 40 nm thick, confining them within the strained layers. The regrowth process, defect morphology, and the effect of implant damage proximity to the Si/SiGe interface was then studied between 500 and 800 ºC.

Strain relaxation of the layers post processing was quantified by High-Resolution X-Ray Diffraction rocking curves and reciprocal space maps. Upon annealing, the solid phase epitaxial regrowth (SPER) process broke down for the highest level of tensile strain and for all levels of compressive strain. Additionally, regrowth related defects were observed in the relaxed samples using cross-section and plan-view Transmission Electron Microscopy (TEM). In tension,

regrowth related defects were nucleated as the amorphous-crystalline front advanced to the surface. Once regrowth was complete, the regrowth related defects propagated down to the strained interface and formed stacking faults which promoted further relaxation. In compression, the advancing amorphous-crystalline front roughened and nucleated an extended dislocation network. The density of these dislocations were stable and did not depend on temperature or duration of anneals.

The results from this study conclude that the SPER process can be achieved without strain loss or defect nucleation for moderate strain values in tension. However, in compression all strain levels in this study nucleated defects and exhibited strain relaxation.

CHAPTER 1
INTRODUCTION

The semiconductor industry, encompassing both silicon and compound materials, has sales in excess of $200 billion dollars per year. While compound semiconductors, specifically III-V technologies, show superior performance to silicon, silicon still dominates the market due to its abundance and low manufacturing costs [Mil05]. Decreasing the manufacturing cost to improve both capability and profit margins has driven the miniaturization of transistor size, which, in turn, decreases the cost per chip while improving device performance. This trend has doubled the number of transistors on a chip every 18 to 24 months, following the prediction of Moore's Law [Moo65]. Until recently, this trend has been satisfied by decreasing (scaling down) the transistor in size. The limit of scaling, however, is being approached and other options to improve device performance must be investigated. One such option is the use of strain engineering in the channel region of the devices. The limitations of strain technology, though, and the impact of strain on the individual fabrication steps are not fully understood. These limitations will be explored in this work.

Motivation

The processing limits of strained silicon technology, which was introduced in the 90 nm technology node, are of great interest to researchers and industry alike. Strained silicon technology improves performance by increasing carrier mobility in the channel of the device through decreases in both the average effective mass and inter-band scattering [Nay96]. Strain can be introduced using two main approaches, substrate-induced and process-induced. The focus of this work will be mainly on process-induced strain.

The strain in the P-type Metal Oxide Semiconductor (PMOS) channel is created by using $Si_{1-x}Ge_x$ Source/Drain (S/D) wells. Alternatively, in N-type Metal Oxide Semiconductor

(NMOS) devices, the strain is induced by silicon nitride overlays forming tensile in the channel region. Examples of both devices are shown in Figure 1-1. Strain can also be process-induced via Stress Memorization Techniques (SMT). This utilizes conventional fabrication processing of amorphizing the S/D region. In the stress memorization process, the activation and recrystallization anneal is carried out post deposition of a nitride tensile stressor capping layer over the gate region. During the regrowth process, the stress induced by the nitride capping layer is "memorized" [Cha05]. The nitride layer is then removed and silicidation is carried out. The degree of stress is dependent on the thickness of the capping layer; the drive current improvement can be increased up to 15% by increasing the nitride thickness [Che04]. Also, because of the simplicity of the SMT and no added etch steps or mask levels it can be easily incorporated into current Si and Silicon-On-Insulator (SOI) transistor fabrication at low fabrication cost [Hor05, Sin05, Sin06]. Additionally, in conjunction with other process-induced strain such as dual-stress liners and SiGe or SiC source-drain regions, the device performance benefits are additive [Hor05].

Once strained, these device structures must undergo additional processing, in particular the final activation anneal. Subsequent thermal processing can cause the strain energy in the heterostructures to decrease and cause strain relaxation by propagation of threading dislocations and formation of misfits [Koe01, Sam99, Sug01]. Additionally, relaxation can also be caused by Ge diffusion from the $Si_{1-x}Ge_x$ into the strained region. Ge interdiffusion and ensuing strain relaxation has shown to be dramatic when the collision cascade of an amorphizing implant overlaps a Si/ $Si_{1-x}Ge_x$ interface [Van05]. In any case, as the level of strain in the structure decreases due to relaxation and dislocation nucleation, the mobility enhancements provided by strained silicon technology also decreases. The defects created in the relaxation process also

decreases device performance by acting as scattering sites. Thus, it is important to understand the exact response of strained regions due to subsequent processing.

Objective

The effects of performing an amorphizing implant contained within a strained layer have not yet been studied, nor has the degree of relaxation, regrowth quality, or thermal stability of such an amorphized region been investigated. These effects may be important for future device structures, as arsenic and phosphorus, both self-amorphizing implants, are often used to create channel extensions in NMOS devices. Additionally, any effects may also be important for stress memorization techniques as they carry out recrystallization of amorphous regions under strain. The purpose of this work, therefore, is to study the effect of an amorphizing implant contained within a strained layer as a function of strain, especially concerning the degree of relaxation, stability after amorphization and recrystallization, crystalline quality of the regrown layer, and proximity of implant to the heterostructure interface.

Dissertation Organization

The contents of this work are organized into seven chapters and three appendixes. This chapter, Chapter One, outlines the motivation and objectives of this work as well as provides a literature review of pertinent topics. Chapter Two provides an overview of material deposition and characterization techniques utilized to carry out the experiments in this work. The next four chapters discuss experimental results. Chapters Three and Four discuss the work carried out under biaxial tensile strain using structures with strained Si on relaxed SiGe virtual substrates. The third chapter discusses the critical strain necessary for SPER breakdown and the mechanism of defect nucleation once the critical strain has been met. The experiments in this chapter discuss results for samples solely implanted with 12 keV Si^+ implants. The fourth chapter discusses the effect of the proximity of the implant to the Si/SiGe interface and how the proximity affects

strain relaxation and defect nucleation. Samples in this chapter were implanted with varying energies of 5, 12, and 18 keV to alter the implant damage proximity to the Si/SiGe interface. Chapters Five and Six mirror the previous two chapters with the exception that the implanted material is under biaxial compressive strain using SiGe on Si structures. Chapter Seven summarizes the results from all experiments and compares the tensile and compressive cases. There are three appendices in this work. The first provides a conversion between stress and strain for the heterostructures used in this work. The second presents the results of using a low temperature pre-anneal to planarize and relax the a-c interface of implanted samples prior to regrowth. The third appendix discusses an experiment carried out on the highest strained tensile and compressive films. In this experiment, the end-of-range damage from conventional beam-line implants was eliminated with the use of octadecaborane cluster implants to generate amorphous layers with the strained epilayer.

Background and Literature Review

Ion Implantation

For the past 50 years, ion implantation has been used by the semiconductor industry as the preferred method for incorporating dopants into silicon. The process offers advantages including reliability, reproducibility and control of dopant dose and distribution. In this non-equilibrium process, ions bombard the host lattice and, through nuclear and electronic interactions, lose energy until they come to rest. This process introduces primary defects consisting of a vacancy rich region near the surface and an interstitial rich region deeper within the substrate where the implanted ions come to rest. For the implanted dopants to be electrically active, a high temperature anneal is required; this process also allows Frenkel pairs, which are interstitial and vacancy pairs, to recombine. At lower implant doses the host lattice can maintain its integrity with isolated regions of defects around Rp, the projected range of the incoming ion. However, at

higher doses when more than 10% of the host atoms are displaced, the implanted region undergoes a first order crystalline-to-amorphous transition, termed amorphization [Chr81]. The amorphized region is completely damaged and no periodic lattice exists. The defective region in this case lies just beyond the amorphous-crystalline (a-c) interface.

Point defects

Point defects are categorized into native defects and impurity related defects. Native defects exist in the crystalline lattice above the absolute zero temperature. Impurity related defects arise from the incorporation of foreign atoms as can be the case in ion implantation processing. There are two types of native point defects: vacancy and interstitial. The simplest of the point defects is a vacant lattice site normally occupied by an atom, termed a vacancy. An interstitial is an atom that occupies a site in the lattice that under ordinary circumstance is not occupied, i.e. a void between host atoms. Diffusion in semiconductors is mediated via point defects; primarily by either an interstitial mechanism or vacancy mechanism.

Amorphization

Amorphization takes place when a sufficient level of fluence and ion mass has been reached. Si and Ge atoms are often used to create amorphized regions in Si substrates [Dea73]. The incoming implanted ions and recoil ions from the surface act as point defects within the host lattice. Upon annealing, these point defect agglomerate into {311} defects and dislocation loops which are located just beyond the amorphous/crystalline (a/c) interface. These are termed End-Of-Range (EOR) defects or type II defects [Jon88].

There are some advantages of amorphizing the substrate prior to dopant incorporation. In particular, boron implants for p-type devices are usually performed after a pre-amorphizing step to avoid channeling effects. The amorphized region, however, must be then be regrown to restore the host lattice as well as activate the dopants by placing them in substitutional sites.

Other dopants, such as arsenic and phosphorus for n-type devices, are self-amorphizing due to their large size. Regions implanted with these ions will also need to be regrown to restore the lattice and activate the dopants.

Solid phase epitaxial regrowth

The recrystallization process of an amorphous layer in contact with a crystalline substrate is termed Solid Phase Epitaxial Regrowth (SPER). This process requires thermal energy for the rearrangement of the atoms in the amorphous region onto the template provided by the crystalline substrate. Rearrangement of the atoms begins at the a/c interface and progresses towards the surface of the material. The regrowth velocity is influenced by and dependent on temperature [Cse78, Ols88], substrate orientation [Cse78], and type of dopant incorporated [Ols88]. Typically, SPER in Si commences around 450 ºC and proceeds up to temperatures just below the melting point [Poa84].

Use of a SPER process is advantageous in that it yields more abrupt junctions, less transient enhanced diffusion effects, and higher activation at a relatively lower temperature. Disadvantages include poor electrical characteristics of the junction, specifically higher leakage current [Bul79, Lin03].

Substrate orientation. Several experiments were carried out by Csepregi et al. [Cse76, Cse78] to study the temperature and substrate orientation dependence of regrowth rate in silicon substrates. Amorphous layers were created by implantation of Si^+ ions at energies ranging from 50 to 250 keV. The samples were annealed and growth velocities were measured via backscattering yield. The growth velocity was found to follow Arrhenius relations and was dependent on the substrate orientation, as show in Figure 1-2 [Cse78]. The growth rate at all orientations was found to have identical activation energies of 2.35 eV over the temperature range of 450-575 ºC. Csepregi found that an <100> orientation resulted in the fastest growth

velocity, <110> growth was approximately three times slower and <111> was the slowest [Cse78]. He proposed a model to explain the orientation dependence. The model proposed a bond-breaking mechanism which transferred atoms at the a/c interface to regular lattice sites. The model also suggested that the transference required at least two nearest-neighboring atoms to be on regular lattice sites.

Later similar experiments were carried out by Olson et al. using more accurate measurement techniques [Ols85, Ols88]. These experiments were carried out by Time Resolved Reflectivity (TRR) measurements which allowed simultaneous measurement of the amorphous layer depth. This experiment found the activation energy to be 2.68 eV and is the most accepted value for SPER in Si.

Extended defects

Extended defects such as dislocations loops, stacking faults and microtwins have been noted after recrystallization [Cse76]. Dislocation loops were observed beyond the a/c interface for <100> and <110> oriented substrates whereas microtwins and stacking faults were observed throughout the regrown layer in the <111> oriented substrates after recrystallization.

End of range defects. End-of Range defects (EOR) defects result after an amorphizing implant and form just below the a-c interface. These defects consist of {311}s at low thermal budgets and dislocations loops at higher thermal budgets. EOR defects are extrinsic in character and have been studied extensively [Cof00, Eag94, Mau94, Pan96]. The main sources of these defects are transmitted ions that stop below the a-c interface and the recoil of excess interstitials as a result of ion bombardment. Excess interstitials exist after SPER because they were unable to undergo Frenkel pair recombination, since the shallower depth of the implant where excess vacancies reside is amorphized. The evolution of these defects at various annealing temperatures and under various ambient atmospheres has also been widely studied [Gil99, Liu95]. At

annealing temperatures below 800 ºC, EOR defects coarsen and decrease in density at the expense of smaller loops through a process called Ostwald ripening [Bon98]. Above 800 ºC, these loops become unstable and dissolve releasing trapped interstitials [Liu95]. The release of these interstitials may lead to enhanced dopant diffusion, known as Transient Enhanced Diffusion (TED) which can drive an implanted junction deeper than desired [Cow94, Fah89, Hof74, Sto95].

Regrowth-related defects. Imperfect regrowth of the amorphous layer leads to the formation of hairpin dislocations or microtwins, also termed type III defects. Hairpin dislocations, found in {100} oriented substrates, nucleate when the a/c growth front encounters misoriented microcrystalline regions and forms a perfect dislocation segment. This segment then wraps around the misoriented material forming a half loop which consists of the base of the hairpin. As annealing continues, the hairpin arms diverge as they advance past the microcrystal regions forming a "V" shape dislocation [San84]. These defects have been shown to be easily avoidable [Jon88, San84]. On the other hand, microtwin formation is observed in {111} oriented substrates during amorphous regrowth. Various models have been proposed to explain the formation of these defects [Cse78, Dro82, Nar82]. Most of these models are based on the bond arrangements of the different orientations. The formation of two distorted bonds defines the difference between an atom in the amorphous and crystalline phase. On the {100} surface, an atom can add anywhere and form two undistorted bonds. However, the {111} surface requires simultaneous addition of three adjacent atoms. These three atoms can either add in the correct positions or with a twin orientation, forming a microtwin [Jon88].

Si/SiGe Heterostructures

Heterostructures offers the ability to construct a variety of device configurations and has become the basis behind bandgap engineering [Cap83]. At first, this field was dominated by III-

V materials. However, compared to silicon these materials are ten times more costly. The obvious solution was to apply the benefits of heterostructures junctions to silicon technology with the use of germanium. The silicon-germanium system offers many advantages such as the ability to alter strain and bandgap by addition of germanium to silicon. The use of this technique has opened the SiGe/Si system to be applied to a variety of applications such as photodetectors, modulation-doped transistors, and heterojunction bipolar transistors. Complimentary metal oxide semiconductor (CMOS) devices dominate the industry and the use of Si/SiGe to this field will be the focus of this work.

The use of strained silicon in PMOS devices offers enhanced hole mobility due to a decrease in the average effective mass and decreased inter-valley scattering [Nay96]. Both biaxial tensile and longitudinal compressive strain can be used to lift the degeneracy in the valence band causing it to shift and become light hole like, as illustrated in Figure 1-3 [Tho04]. This decreases the hole effective mass thereby, increasing mobility. This can be implemented in the CMOS flow by the use of epitaxially deposited B-SiGe S/D wells in p-type transistors. Additionally, in situ boron deposition with SiGe growth allows higher dopant activation without the need of high temperature activation anneal because B occupies substitutional sites upon deposition. A higher activation concentration of B also leads to lower contact resistance [Raa99].

Strained Structures

The Si/SiGe system possesses several attractive properties. First, Ge and Si have similar properties including crystal structure, atomic size factor, valence, and electronegativity which allow a complete solid solution to be formed when they are mixed. The phase diagram of Si-Ge is presented in Figure 1-4. Second, the lattice parameter of SiGe is a function of Ge composition that shows a slight deviation from the linear function stated in Vegard's law [Dis64]. Therefore,

since epitaxial growth of pseudomorphic films causes the lattice constant of the film and substrate to be in perfect atomic registry, Figure 1-5, a variable amount of strain can be created in the system by varying the SiGe composition. Biaxial tensile strained silicon is obtained by using $Si_{1-x}Ge_x$ to serve as a "virtual substrate." Additionally, by growing $Si_{1-x}Ge_x$ on Si substrates one can grow a biaxial compressive strain material. The maximum mismatch between the layers is based on the difference between the equilibrium lattice spacing of Si (5.43 Å) and Ge (5.66 Å) and has a maximum value of approximately 4.2%. The amount of Si that can be grown on top of a SiGe virtual substrate or SiGe on Si, however, must be kept below a critical thickness to prevent relaxation [Mat74, Peo85]. Below this critical thickness, the strain is stored in the film elastically. Above this thickness, the strain is accommodated by strain-relieving defects, termed misfit dislocations, causing relaxation.

Misfit Dislocations

The elastic strain which is stored in the pseudomorphic film can cause the formation of interfacial misfit dislocations, which act to relieve the elastic strain after sufficient annealing or critical magnitude of strain. The generation, propagation, and velocity of these dislocations have been studied extensively [Bea87, Dod88, Dod89, Fri87, Hou91,Hul89, Hul92, Kas75, Peo85, Tsa87,Van63]. The following sections will summarize the prior work involving misfit dislocation microstructure, mechanism of strain relief, and calculation of the critical thickness.

Microstructure. Si, Ge, and $Si_{1-x}Ge_x$ alloys all have diamond cubic lattice structures in which dislocations are known to glide primarily on {111} planes. Geometrically, a dislocation cannot terminate within the bulk of a crystal. Instead, it must terminate upon itself, with another defect, or at the nearest free surface. Most commonly, misfit dislocations terminate by forming threading arms that extend to the surface, as shown in Figure 1-6. Misfit dislocations are perfect dislocations with a Burgers vector of a/2<110>. The dislocations are energetically unstable and

are hence known to dissociate into Shockley partials [Hir68, Rea53], according to the reaction in Equation 1-1.

$$a/2\langle 110\rangle = a/6\langle 1\text{-}12\rangle + a/6\langle 211\rangle \qquad (1\text{-}1)$$

The Shockley partials (right side of equation) are mutually repulsive and glide away from each other on the {111} glide plane. This causes formation of a stacking fault. The equilibrium partial spacing, s_o, is determined by the balance of the repulsive energy between the interacting partials and the energy of the stacking fault. The glide motion on the {111} plane also results in an angle, θ, between the Burgers vector and the dislocation line direction. For the a/2<110> type misfit dislocation the angle is 60º, and for the two Shockley partials, 90º and 30º. The lattice-mismatch stress is resolved differently onto these two partials [Mar87]. Thus, the critical resolved shear stress is different for each case; the stress is higher on the 90º partial than the 30º partial. For a case where the (100) interface is under compressive strain, the 30º partial leads and the 90º partial trails. The trailing partial experiences a greater resolved shear stress than the 30º, thus, reducing the partial separation, s_o, and may result in zero separation. For the tensile case, the 90º partial leads and the 30º trails, increasing s_o to levels which can approach infinity. In this case, the separation causes the misfit dislocations to consist of 90º a/2<211> type partials, which leave stacking faults behind as they propagate through the crystal; this has been observed in the SiGe/Ge (100) system [Weg90].

Nucleation. Misfit dislocation nucleation mechanism in the SiGe/Si system is still debated among researchers. There are three generic mechanisms for nucleation of misfit dislocations discussed in literature: homogeneous, heterogeneous, and dislocation multiplication events.

Homogeneous nucleation occurs when intrinsic strain is high enough to allow finite rate of dislocation loop nucleation within the epilayer, or half-loop nucleation at the free surface. This

requires higher strains to produce a significant nucleation rate. The earliest calculation of activation energy for homogeneous dislocation loop nucleation goes back several decades [Hir68]. For the case of the strained layer, activation energy is the sum of the self energy of the dislocation loop and the strain energy relaxed by it. For the free surface half-loop, the energy is a function of loop radius. The activation barrier for half-loop calculated by researcher [Hul89, Weg90] is about 5 eV at 600 ºC for strain values in excess of 0.02 or a 50% Ge.

Heterogeneous nucleation must be considered for lower levels of strain where homogeneous nucleation is not possible. Heterogeneous nucleation occurs at a local site within the crystal where strain is higher thus; the probability of dislocation nucleation is higher. Such sites correspond to defects such as precipitates, grain boundaries, contamination, etc. The predominant nucleation source can differ within a given material system, growth condition, and/or growth techniques.

Lastly, dislocation multiplication nucleation is recognized as the dominant nucleation mechanism at relatively low and high epilayer thicknesses. This type of dislocation nucleation concept goes back to Frank-Read sources [Hir68] and the first documented source in strained (Ge/GaAs) layers [Hag78]. In recent years, several works have reported multiplication event in the SiGe/Si system [Alb95, Cap92, Tup90]. Typically, the sources for this mechanism require thick epilayers which translate to relatively low strain. Tuppen et al. [Tup90] used layers with minimum thickness of 700 nm and strain of 0.005 ($Si_{0.87}Ge_{0.13}$). LeGoues and Mooney's group [LeG93, Moo94] determined a Frank-Read-like multiplication source activation energy of 4-5 eV for in SiGe/Si layers with Ge concentrations from 5 to 20% and a thickness of 380 nm.

In summary, homogeneous mechanism is thought to dominate at higher strains and dislocation multiplication at lower strains with greater epilayer thicknesses. For relatively low

strain and lower thicknesses, only heterogeneous sources are available and misfit dislocations become nucleation limited. Experimentally, there is still a small collection of misfit nucleation mechanism data in the SiGe/Si system. A wider range of strain and epilayer thicknesses data is necessary to fully understand the regime in which each of the nucleation mechanisms occur.

Propagation. The mechanism of misfit propagation in the SiGe/Si heterostructure systems have been well researched and is accepted to be mediated via dislocation glide. Dislocation glide in bulk Si and Ge crystals from plastic deformation is also well documented [Ale68, Far86, Ima83, Pat66]. Pure intrinsic Si and Ge crystals have activation energies of 2.2 and 1.6 eV, respectively, at low stress (up to 100 MPa). The pre-exponential factor for both materials is the same and thus dislocation glide is much faster in Ge than Si. Additionally, glide activation energy in SiGe alloys is expected to decrease with increasing Ge while glide velocity is expected to increase with increasing Ge content.

In addition, dislocation glide in bulk SiGe alloys of low Ge or Si concentrations have been reported [Yon96, Yon99] and agree with extrapolation of experiment from the elemental compounds. Comparatively, an activation energy for glide has been documented for a $Si_{0.7}Ge_{0.3}$ on Si thin film relaxation with a value around 1.1 eV [Hul89, Dod88] and 1.38 eV [Lei01], all values are lower than the 1.8 eV determined for SiGe bulk material. The lower activation energy observed in thin film versus bulk materials could be caused by lower formation energy due to the close proximity of the interface and free surface [Hul89]. Since activation energy is the sum of the formation and migration energies, it is reduced. An alternative explanation by Hull et al. [Hul89] to be more likely in their work, is that as the dislocation density and anneals temperature increases, the propagating dislocations have to cross more and more orthogonal dislocations in a given length. These intersecting events are observed to impede propagation. Thus, the low

observed activation energy would be a function of reduced velocity at high temperatures rather than an enhancement at low temperatures [Hul89].

Dislocation kink model. The Si lattice is periodic and dislocations tend to follow the low index, low energy "Peierls valleys" of the crystal. Ideally, dislocations are linear; however, dislocation interactions cause curvature. Two straight dislocation segments in the same glide plane lying in neighboring Peierls valleys are connected by a kink where the dislocation jumps the Peierls barrier. Thus, dislocation glide is controlled by the Perierls-Nabaro mechanism, such that a dislocation can move from one Peierls valley to a neighboring one by nucleation and migration of kink pairs along the dislocation. Essentially, this results in the kink formation and migration determining the dislocation velocity [Hir68]. Hirth and Lothe describe a double kink model based on Perierls-Nabaro mechanism which is the generally accepted model for dislocation motion in Si/SiGe heterostructures [Hir68]. Furthermore, this model also predicts a lowering of the activation energy with increased driving stress which has been observed experimentally.

Critical thickness

Pseudomorphic epilayers are obtained when the thickness of the strained overlay is below a critical thickness and the atoms are arranged in perfect registry on either side of the heterostructure interface [Mat74, Peo85]. This prevents performance-degrading and strain relaxing misfit dislocations with a Burgers vector of a/2 <110> from forming at the interface. Many researchers have undertaken work to understand the limitations of strained layer epigrowth.

Previous work has shown that there exists a critical thickness at which no misfit dislocations are generated and the strain is accommodated completely by the elastic strain energy. The first to propose a theory for critical thickness for mismatch layers was Van der

Merwe [Van63]. His theory was based on an energy balance criteria in which the stability is described by relative energies of two competing interfacial structures. First, the lattice mismatch is accommodated by elastic strain only and the second, accommodated by both elastic strain and misfit dislocations. The balance of these two energies can yield a critical thickness. The energy to generate a dislocation is described in Equation 1-2.

$$E_{dislocation} = \frac{Gb^2}{4\pi(1-\sigma)}\frac{2}{\lambda}\ln\left(\frac{h}{b}\right) \tag{1-2}$$

G is the shear modulus, assumed to be the same in the film and substrate, b is the Burger's vector, s is Poisson's ratio and 2/l is the dislocation length per unit area of the epilayer. The energy stored in strained layer is presented in Equation 1-3.

$$E_{strain} = Mh\varepsilon^2 \tag{1-3}$$

Where M is the biaxial elastic modulus of the epilayer, e is the strain and h is the thickness of the epilayer.

Matthews and Blakeslee based their calculation on the energy balance criteria of Van der Merwe with one exception. They stated that misfit dislocations are generated through the glide of threading dislocations from the underlying substrate [Mat74]. Additionally, they made some assumptions about the two material's properties: crystal structures are cubic, elastically isotropic and they both have similar elastic constants. The critical thickness data can, therefore, be applied to either Si on SiGe or vice versa. Figure 1-7 shows the critical thickness of strained silicon on SiGe calculated using Matthews-Blakeslee theory which is similar to the SiGe/Si system based on the material property assumption. These calculations can be applied to silicon on $Si_{1-x}Ge_x$ according to these assumptions.

For metal films, the theoretical critical thickness agrees well with the predictions of Matthews-Blakeslee [Kuk83]. This is not the case in semiconductors. Jain et al. [Jai90] offered

two possible explanations for this discrepancy. The first, due to the lack of resolution of the measuring technique and the second suggested that equilibrium is not reached under experimental conditions. These two explanations will be discussed below.

Fritz compared the experimental values of the critical thickness in InGaAs/GaAs and GeSi/Si systems by photoluminescence and XRD rocking curve measurements [Fri87]. He found that the critical thickness determined by photoluminescence was in good agreement with theoretical values, whereas, the XRD rocking curves (sensitivity of 10^{-3} strain) yielded higher critical values [Bir03]. They also found that relaxation is slow in its initial stage and a high resolution measurement technique would be needed to measure the onset of relaxation which can occur as low as 10^{-7} strain.

People and Bean [Peo85] made the first attempt to calculate critical thickness taking into account the extra strain energy needed to overcome the barrier to relaxation in order to explain the large observed values of critical thickness experimentally. By equating the strain energy to the dislocation energy at critical thickness and assuming the dislocation width to be 5b, they obtained an equation that describes their experimental results well. Their results are plotted in Figure 1-8 along with the predictions of other theories. Furthermore, it is theorized by many that the larger observed values are due to non-equilibrium growth carried out at relatively low temperatures.

Extensive research and various models have been proposed to provide explanation of the discrepancy in the calculation of the critical thickness [Dod87, Jai90, Kas75, Mat74]. The discrepancy lies mostly in growth temperature and measurement technique yielding different critical thicknesses. However, the Matthews-Blakeslee mechanical equilibrium theory is the most accepted among researchers today.

Morphology during growth

Different growth modes have been observed during epitaxially film growth of mismatched materials. Frank Van der Merwe growth consisting of layer by layer growth, Volmer-Weber consisting of island growth, and Stranski-Krastanov growth consisting of layer then island growth. Prior work has shown that the type of growth observed is dependent on the relative interfacial energy and strain energy contributions. In the case, of an epitaxially growth film on a substrate with mismatched lattice constants such as SiGe on Si or vice versa, the strain in the film is the given as $(a_s-a_f)/a_f$. An energetic analysis shows the expected instability of the film due to strain [Sro89]. Consider a step wave surface morphology where the sample is stressed in the in-plane direction. The change in energy going from the flat surface to the rough morphology is given by:

$$\Delta F = \frac{-\sigma^2}{2E}\frac{c\lambda}{2} + 2\gamma_c \qquad (1.4)$$

Where E is the elastic modulus, λ is the wavelength of wave morphology, c is the amplitude of the wave, σ is in-plane stress, and γ is the surface energy. Equation 1.3 shows that forming a rough surface will lower the overall energy of the system provided that the wavelength, $\lambda > 8\ \gamma E/\sigma^2$ [Sro89]. This crude estimate by Srolovitz demonstrates why surface roughness is observed in stressed films.

Thermal stability

The stability of strained silicon epilayers after thermal processing alone has been investigated by many [Koe01, Sam99, Sug01]. Strain loss has been observed after high thermal processing, above 950 ºC, through threading dislocation propagation and misfit formation. This relaxation behavior shows both a temperature and time dependence. It also strongly depends on the initial level of strain set by the thickness of the silicon cap. Additionally, relaxation can be

caused by Ge diffusion into the strained overlay. Ge diffusion into the strained layer, termed interdiffusion, becomes significant after 950 ºC for 1 hour [Sug01].

SPER and Strain

Since the introduction of strain into the CMOS process, the effect of SPER under strain has been a great topic of interest. SPER has been used to produce strain by strain memorization techniques by regrowing the amorphized layer post deposition of a strained capping layer to "memorize" the strain produced by the cap. Also, strain has been induced by implantation of high dose Ge or C ions to induce strain by changing the lattice parameter within the projected range of the implant. This section will discuss previous work conducted using SPER to produce residual strain within the implanted substrate.

Strained silicon SPER

The effects of an amorphizing implant on strained silicon structures yield more detrimental results to the strained layers than thermal processing alone. Chilton et al. amorphized a heterostructure with 33 nm Si on 30-35 nm $Si_{1-x}Ge_x$ deposited by MBE on a (001) Si substrate. The structure was amorphized to a depth of 130 nm with a 120 keV As^+ implant. Coherent epitaxial growth was observed if the Ge fraction was below x = 0.16, however, at x = 0.29 after a 600 ºC anneal the regrown layer exhibited a 75% reduction in strain. The silicon on this now "relaxed" $Si_{0.69}Ge_{0.29}$ exhibited 15% relaxation. The relaxation was measured using Rutherford backscattering spectroscopy and no defect density analysis was performed [Chi89]. It is important to note that no graded buffer layer was used to relax the SiGe layer.

Vandervorst et al. [Van05] implanted arsenic with varying energies of 2 to 15 keV through a 10 nm Si cap grown on relaxed $Si_{0.78}Ge_{0.22}$ and monitored Ge diffusion using secondary ion mass spectrometry. He showed that Ge interdiffusion and ensuing strain relaxation was more dramatic when the collision cascade of an amorphizing implant overlaps the Si/ $Si_{1-x}Ge_x$

interface. Therefore, the implant should be contained in the capping layer in order to avoid Ge redistribution, which can ultimately cause relaxation. Again, the defect microstructure was not characterized.

Strained silicon germanium SPER

A great deal of work has been performed using structures containing strained silicon germanium grown on silicon. This section, however, will focus on the stability of these structures after an amorphizing implant. Pseudomorphic $Si_{1-x}Ge_x$ structures with epilayer thicknesses that exceeded the critical thickness but maintained atomic registry due to non-equilibrium low-T growth are among the structures that have been studied. Lee and Hong both studied SPER in metastable $Si_{1-x}Ge_x$ layers, x < 12 at% [Hon92, Lee93]. The amorphous layer, in both cases, was generated through the $Si_{1-x}Ge_x$ /Si interface using Si^+ implants. Upon annealing, as the a/c front translated through the interface and the amorphous layer regrew defect-free until the critical thickness [Mat74] was reached. Beyond this thickness the film reached an energy state where defects were energetically favorable. The energetically favorable state caused defects to nucleate and grow within the remaining regrown layer. Paine et al. conducted similar experiments with germanium compositions up to 17 % [Pai91]. Paine analyzes the preferred defect configuration using Matthew-Blakeslee [Mat74] and Freund [Fre87] criteria. He concludes that beyond a critical thickness, the strained crystalline portion of the alloy can fully relax via stacking fault bounded by a 90º partials.

Some SPER experiments were conducted in nearly stable SiGe layers and conducted amorphizing implants through the Si/SiGe interface. Rodriguez et al. conducted an experiment using 30nm CVD grown SiGe with concentrations of 21, 26, and 34% Ge. An amorphous layer was generated using a 200keV Ge^+ implant at a fluence of $1x10^{15}$ atoms/cm^2 which extended through the Si/SiGe layer. Half of the samples were also implanted with B^+ 5-20 keV at a

fluence of $7x10^{15}$ atoms/cm^2 and annealed at 600 ºC. The samples regrew defect free for the undoped case as follows: 18-20 nm for 21%, 12-15 nm for 26%, and 0 nm for 34%. The doped samples regrew with a thicker defect free layer than the undoped case, 30 nm, 18-20 nm, and 0 nm for the 21, 26, and 34 % Ge respectively [Rod97]. The defects were in good agreement with the calculation done by Paine et al. consisting of the 90º partial accompanied with a stacking fault as described by Paine et al. [Pai91]. During annealing B^+ is competing for a substitutional site and thus reduces the overall strain in the material. By decreasing the strain the critical thickness of the system is increased as observed. Chilton et al. conducted similar experiment using 30-35 nm SiGe with concentrations ranging from 16-29% [Chi89]. Amorphization was conducted using 120 keV As^+ implant. Strain recovered for the lowest case, 16%, however, coherency was destroyed in the 29% Ge case. Characterization was carried out using RBS and no finding of the defect microstructure was discussed.

Prior work has also shown instability in the advancing amorphous-crystalline (a-c) front, mostly under compressive strain. This roughening effect has been observed in compressively strained Si films [Bar04] and in metastable strained SiGe films [Ang07, Cor96] during SPER and in high dose Ge^+ implants into Si to form SiGe [Cri96, Ell96]. A defect-free planar a-c interface, however, has been shown in relaxed SiGe films with up to a 38% Ge concentration [Kri95]. Therefore, the a-c interface morphology is connected to strain and not due to alloying with germanium. Additionally, Antonell et al. [Ant96] showed that incorporating C into SiGe prior to amorphization delayed the onset of dislocation formation and promoted planar a-c interface growth due to strain compensation effects.

Relaxed silicon germanium SPER

Defects. Defects were observed after amorphization and regrowth in some cases with strained SiGe. However, the relaxed SiGe case is quite different. Relaxed psuedomorphic SiGe

grown using graded layers on Si substrate was used to study the SPER rate and crystalline quality post regrowth. In each case, regrowth was observed to be defect-free [Hay95, Kri95a]. A defect-free regrown layer and a planar advancing a-c interface has been shown in relaxed SiGe films with up to a 38% Ge concentration [Ell95, Kri95]. Therefore, we concluded that SPER breakdown observed in the metastable strained SiGe is a strain effect and not a chemical effect.

Velocity. Several researchers have reported SPER rates of strained and unstrained SiGe with respect to pure Si. Haynes et al. [Hay95] studied SPER rate in unstrained alloys 8 μm thick with germanium compositions varying from 2 to 87%, including pure Si and Ge. Amorphous layers 300-400 nm thick were produced using Si^+ implants. For each composition, the measured SPE rates span two orders of magnitude and are related to the pure elements. The Si-rich alloys displayed activation energies for SPER higher than pure Si and same to be true for Ge-rich alloys and pure Ge. The a-c interface of high germanium alloys was confirmed to be planar using XTEM. Lee at al. [Lee93] measured SPER rates of strained SiGe with germanium composition of 12%. Rates were measured using Time Resolved Reflectivity (TRR) and real-time measurements demonstrate SPER rate is not constant over a fixed temperature but varies with the position of the a-c interface. The activation barrier is higher than pure Si and ranges from 2.94 to 3.11 eV for temperatures between 503 and 603 ºC. Paine et al. [Pai91] reported an activation energy of 3.2 eV independent of germanium using in situ TEM. Structures used in this experiment were 200 nm SiGe grown via CVD with germanium compositions of 5.4, 11.6, and 17%.

Outstanding Questions

It is important to note that prior experiments observed regrowth related defects for structures that were thermodynamically metastable with film thicknesses exceeding 200 nm. Also, most implants carried out were conducted through the $Si_{1-x}Ge_x$ /Si interface. Crosby et al.

[Cro04], however, has shown that implants conducted through-the-layer and within-the-layer impact the overall strain state of the material post anneal. Thus, there is a gap in understanding the effect of SPER within a strained layer vs. through a strained layer and how the proximity of the a-c to interface to the heterostructure interface affects relaxation. Also, the microstructure and stability of regrowth related defects have not been well studied. This work aims to understand the impact of both proximity and strain level on defect nucleation and strain relaxation. This work also aims to explore the relationship of the critical thickness with defect-free regrowth under biaxial compressive and tensile strain.

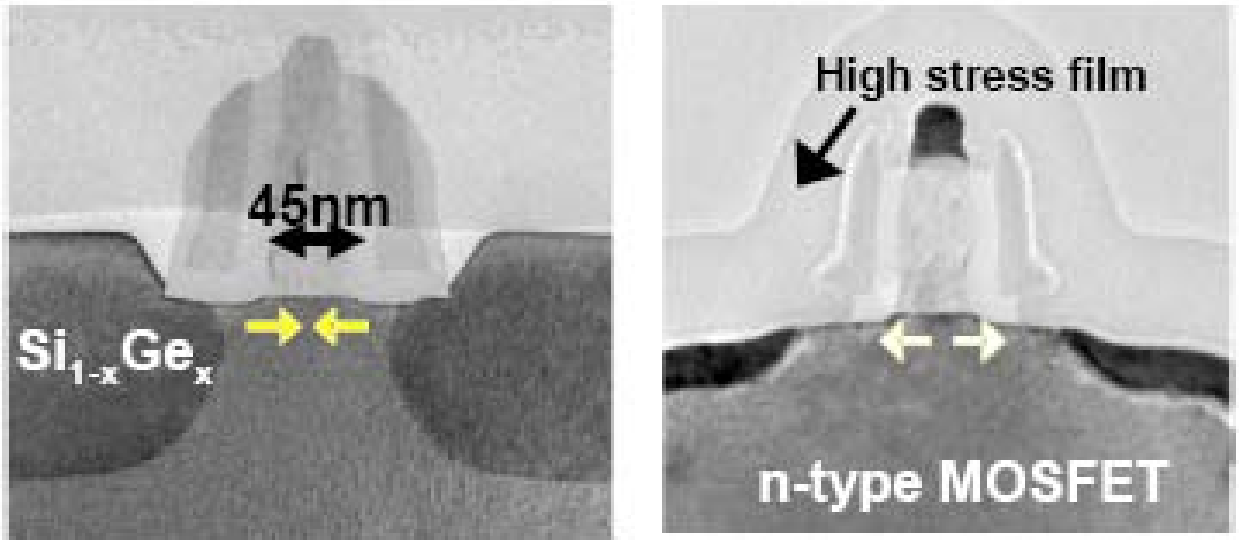

Figure 1-1. XTEM image of P-type and n-type MOSFET channel [Tho04].

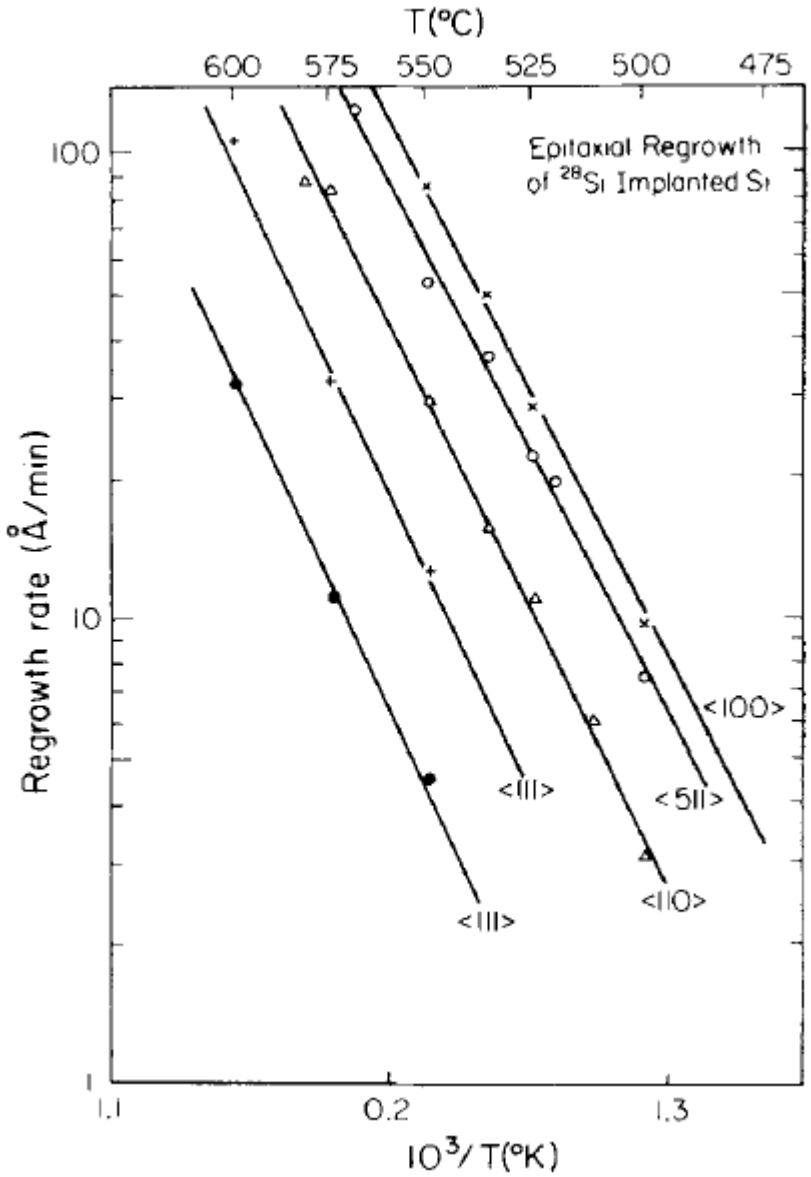

Figure 1-2. Arrheiuns plot of regrowth rate for Si samples oriented along <111>, <110>, <100> directions [Cse78].

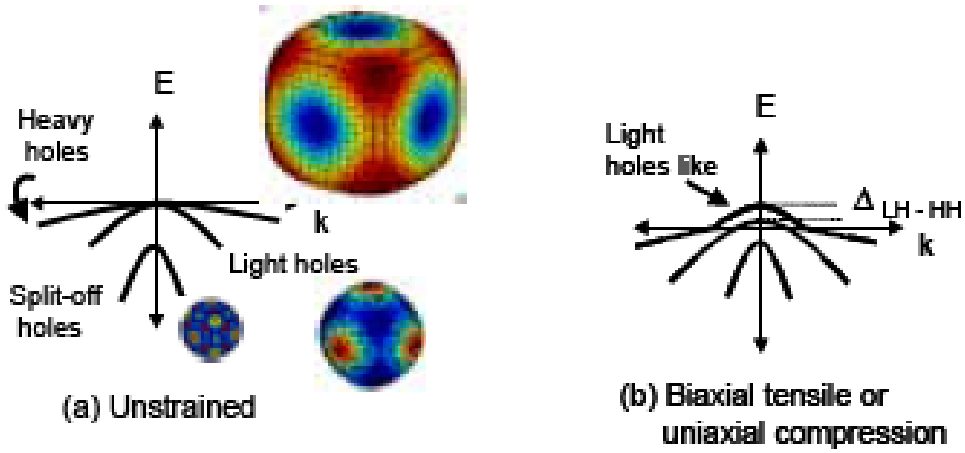

Figure 1-3. Valence band of (a) unstrained and (b) strained Si showing decreased in light hole effective mass for strained case [Tho04].

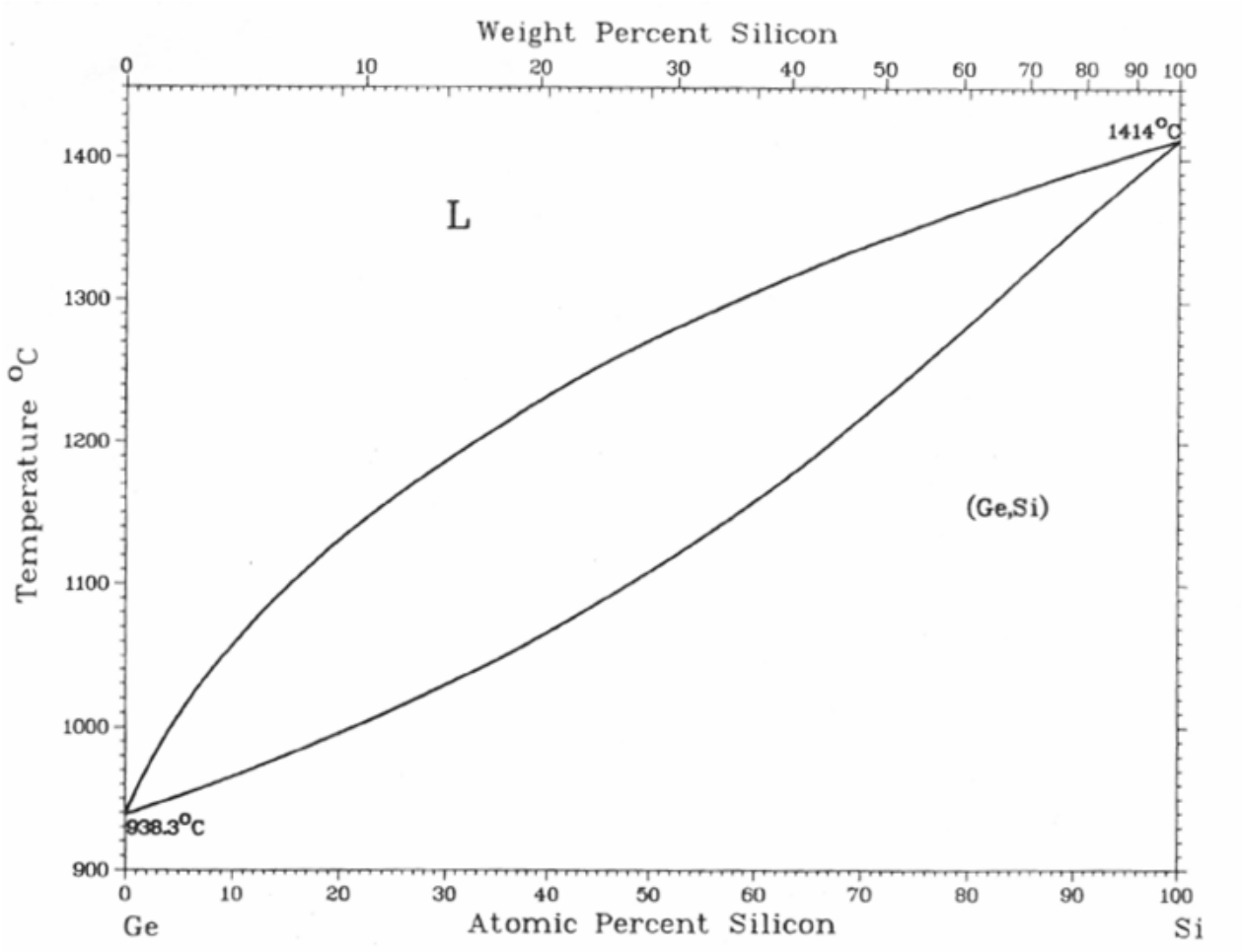

Figure 1-4. Binary phase diagram of Si-Ge system showing complete solid solubility [Mas90].

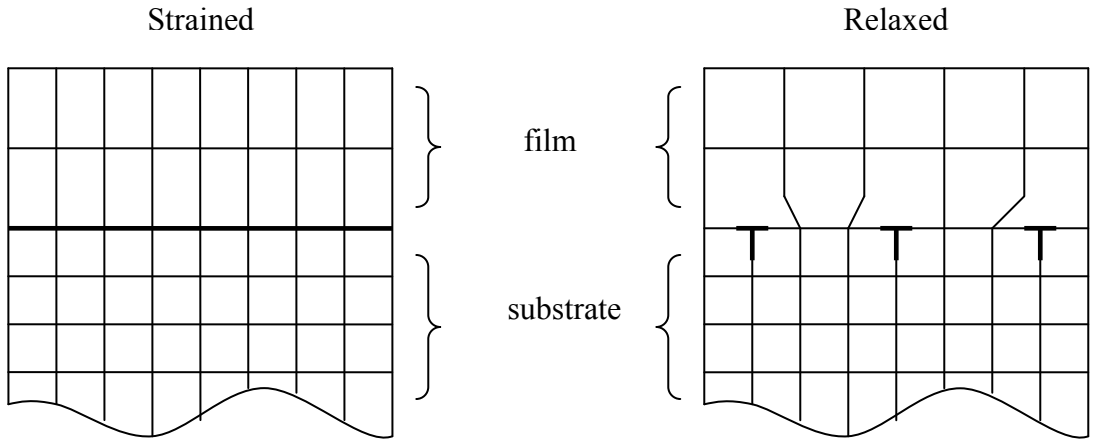

Figure 1-5. Schematic representation of strained film interface versus a relaxed film interface.

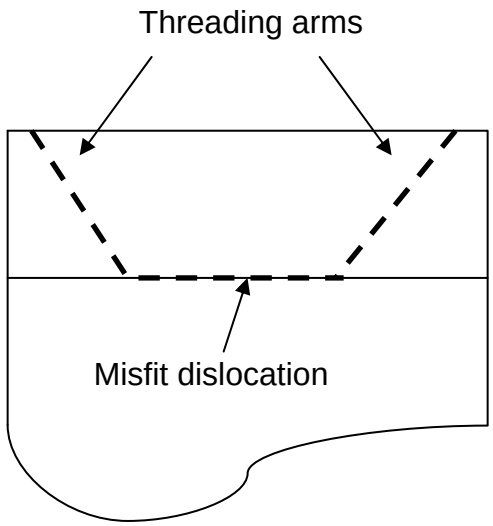

Figure 1-6. Microstructure of misfit dislocation with threading arms in cross-section.

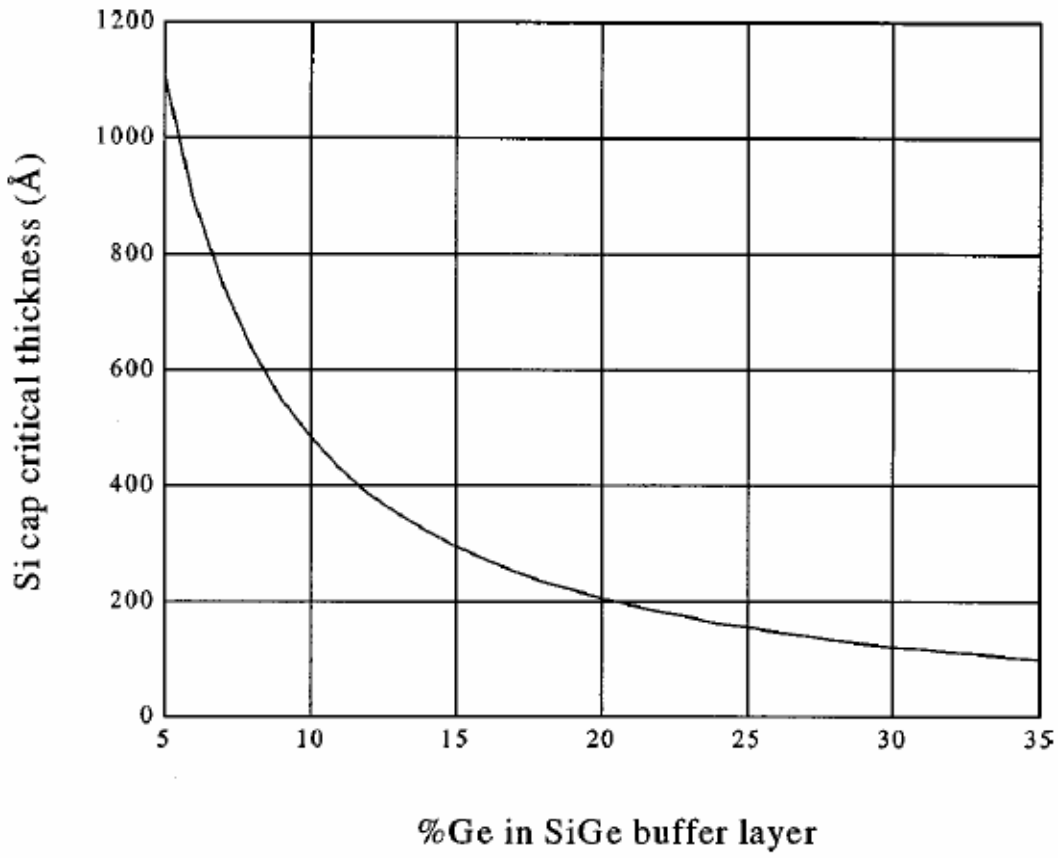

Figure 1-7. Si cap critical thickness as a function of Ge% in the uniform SiGe layer [Sam99].

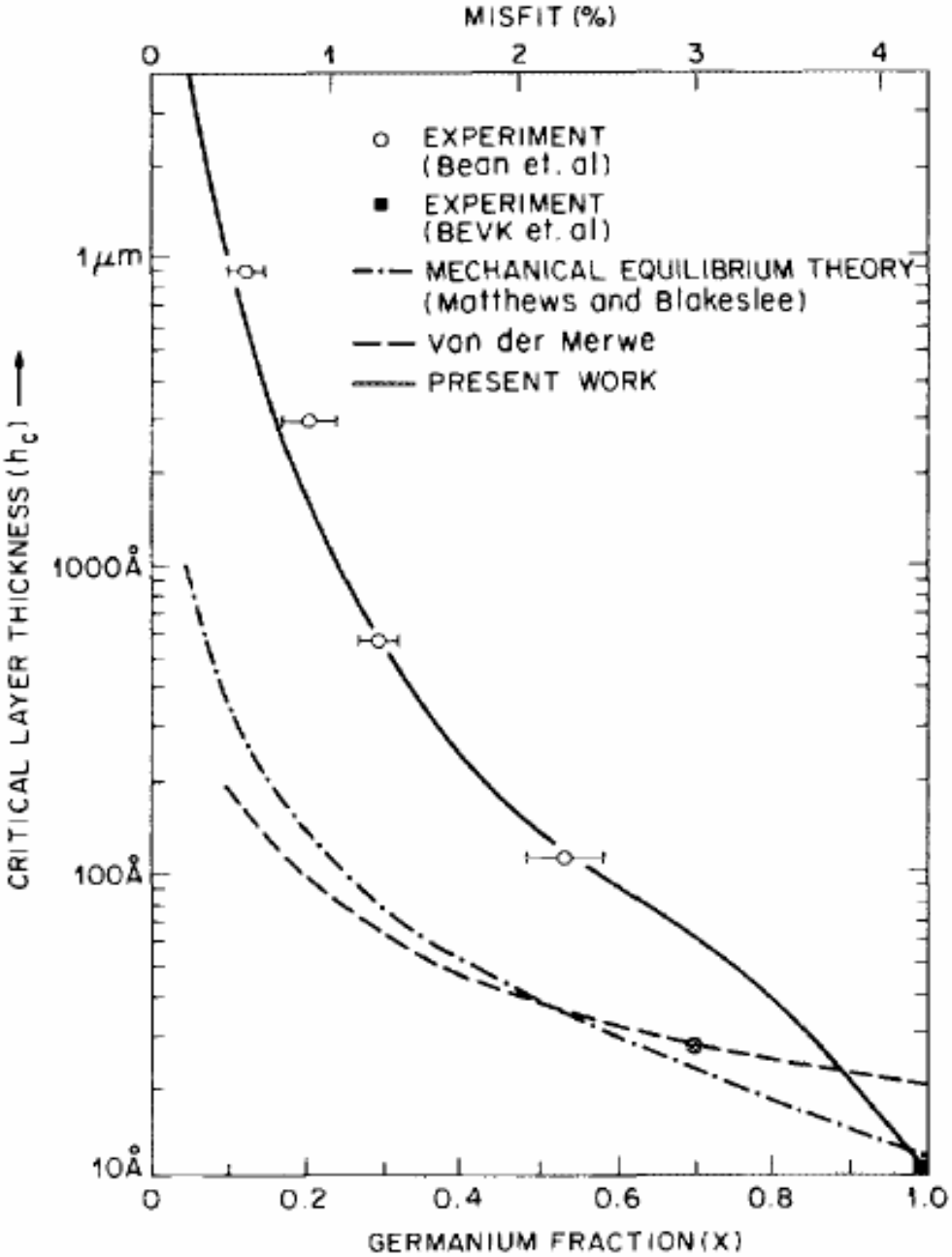

Figure 1-8. Critical thickness as a function of Ge concentration [Peo85].

CHAPTER 2
EXPERIMENTAL METHODS

The experiments carried out in this work required application of different processing and growth techniques. A brief description of these techniques will be discussed in this chapter. The strained films and alloys were grown by Molecular Beam Epitaxy (MBE) and Chemical Vapor Deposition (CVD) techniques. Post deposition, the strained layers were then implanted and annealed. The film morphology and strain relaxation post processing and anneal were studied and characterized using Transmission Electron Microscopy (TEM) and High-Resolution X-Ray Diffraction (HRXRD) techniques.

Material Processing

Growth Conditions: Strained Si on Relaxed SiGe

The structure with Si in biaxial tensile strain were grown using a Molecular Beam Epitaxy (MBE) chamber at the University of Aarhus in Denmark. MBE is a deposition technique that uses a ultra-high vacuum chamber. Material is deposited by heating the solid source until it evaporates using an electron-beam. The evaporated material then condenses on the substrate, which spins during deposition to promote uniformity. The chamber walls are cooled with liquid N_2 to reduce outgassing.

The experimental structures were grown with compositionally graded buffer layers at 750 ˚C incorporating Ge at a rate of 10 at.% per micrometer on silicon substrates to compositions of 0, 10, 20 and 30 at.% Ge with low threading dislocation densities of $1x10^5$ cm^2. A 630 nm thick fully relaxed SiGe layer of corresponding composition was then grown on top of the buffer layer at 550 ºC, followed by a pseudomorphically strained silicon capping layer 50 nm thick. A schematic of the multi-layered structure is shown in Figure 2-1. The details of the growth conditions and threading dislocation density are presented by Gaiduk et al. [Gai00].

Growth Conditions: Strained SiGe on Si

The structures with SiGe in biaxial compressive strain structures were grown using a reduced pressure Chemical Vapor Deposition (CVD) chamber at Texas Instruments, Inc. Specifically, a RP-CVD tool from ASM, the Epsilon 3200, was used to grow all samples. The gaseous precursors used for silicon and germanium were dichlorosilane and germane. Hydrogen was used as the carrier gas at a flow of 40 standard liters per minute. The growth was carried out at 700 °C and a fixed pressure of 10 Torr. Prior to deposition, an HF clean and a pre-bake of 1050 °C 3 minutes was carried out to remove oxide and all contaminants on the wafer surface. Strained 50 nm $Si_{1-x}Ge_x$ was deposited on Si (001) substrate with alloy compositions of 0, 16, 22, and 26 at% germanium. A schematic of the structure is shown in Figure 2-2.

Ion Implantation and Annealing

Ion implantation has been used by the semiconductor industry as the preferred method for incorporating dopants into silicon. The process offers advantages including reliability, reproducibility and control of dopant dose and distribution. In this non-equilibrium process, ions bombard the host lattice and, through nuclear and electronic interactions, lose energy until they come to rest. This process introduces primary defects consisting of a vacancy rich region near the surface and an interstitial rich region deeper within the substrate where the implanted ions come to rest. For the implanted dopants to be electrically active, a high temperature anneal is required; this process also allows Frenkel pairs, which are interstitial and vacancy pairs, to recombine. At lower implant doses the host lattice can maintain its integrity with isolated regions of defects around Rp, the projected range of the incoming ion. However, at higher doses when more than 10% of the host atoms are displaced, the implanted region undergoes a first order crystalline-to-amorphous transition, termed amorphization [Chr81]. The amorphized region is completely damaged and no periodic lattice exists. The defective region in this case

lies just beyond the amorphous-crystalline (a-c) interface. Annealing is required post implantation to repair the damaged lattice.

All Si^+ implants were carried out at Axcelis Technologies in Beverly, Massachusetts. First, the ions are accelerated to a potential of 100 keV before being mass analyzed by a magnet. The analyzed ions are ejected into the accelerator stage where they are accelerated further. For energies below 100 keV, the implant is operated in acceleration /deceleration mode. During this mode, a N_2 stripper gas canal is evacuated such that the ions do not exchange charges while passing through the accelerator. The ions are accelerated into the terminal potential and then decelerated. The ions then exit the acceleration stage at the energy desired. The implant energy used in this work were 5, 12, and 18 keV at a fluence of $1 \times 10^{15}/cm^2$ which generated continuous amorphous layers 15, 30, and 40 nm, respectively.

Material Characterization

Transmission Electron Microscopy

Sample preparation. The morphology of the samples was monitored using TEM. Post implantation and regrowth damage can be determined in three dimensions with the use of plan-view and cross-sectional sample preparation. In order for the samples to be imaged using the TEM, it is imperative to polish them to a thickness such that electron transmission occurs (~200 nm).

Plan-view (PTEM) samples were prepared cutting a 3 mm disc from the sample using a Gatan ultrasonic disc cutter with the aid of SiC cutting slurry. The disc was then thinned down to approximately 100 micrometers using 15 μm particle size Al_2O_3 slurry on a glass plate. The implanted side was next coated with paraffin wax and the sample is then mounted on a Teflon mount termed "Johnny." The sample was subsequently jet etched with an acid solution consisting of 25%HF:75% HNO_3 [Ste07] until a small hole appeared. The sample is removed

from the Johnny and placed in a beaker filled with heptane left to soak overnight. Heptane is used to dissolve and remove the wax off the sample. Regions of the sample in proximity of the hole are electron transparent and can be imaged using TEM. These plan-view samples allow planar observation of the dislocations and the ability to quantify them.

Cross-sectional (XTEM) samples were prepared using a FEI Strata DB 235 Dual-beam Focused Ion Beam (FIB). The sample was mounted on a FIB stub using conductive carbon paint and then coated with 50 nm of puttered carbon film prior to FIB milling. The sample was then put into the FIB chamber and the chamber pumped down to vacuum. A strip of GIS Pt was deposited on the area of interest to protect it from beam damage. Two wedges were then milled on either side of the Pt strip using 5000 pA beam current. The Pt protected area was next thinned with consecutively smaller beam currents until a final thickness of about 150 nm was achieved. The sample was extracted using an ex-situ micromanipulator system attached to a light microscope. Finally, the sample was placed onto a carbon film on a Cu grid array, ready for imaging. Cross-section TEM analysis primarily allows observation of the depth of the epitaxial layers and defects.

Imaging conditions. A JEOL 2010F high-resolution transmission electron microscope (HRTEM) and a JEOL 200CX TEM operating at 200 kV were used to analyze the defects in the regrown layer. XTEM measurements were used to confirm the amorphous layer depth and layer thicknesses. PTEM samples were prepared and imaged to quantify dislocation density. TEM is the only technique that allows analysis to determine if a defect is extrinsic/intrinsic in nature and determine Burgers vector.

Imaging of the extended defects post implantation using diffraction contrast [Edi75, Wil96] was employed to determine the position and quantity of the defects. For the implant dose

used in this study, end-of-range (EOR), also known as type II defects, will form. Also, type III or regrowth related defects are probable after annealing. Diffraction contrast theory states that defects are visible if $g \cdot b \times u \neq 0$ where g is the reciprocal lattice vector corresponding to diffracting plane, b is the Burgers vector for a dislocation, and u is the line direction of the dislocation. The Burgers vector for dislocation loops in Si are a/2<110> and a/3<111> type, and for {311} defects it is a/24<116> type. A two-beam bright field (BF) condition with s > 0, s is deviation from Bragg condition, is used to image the PTEM and XTEM. The g_{220} reflection is used to image dislocation loops and regrowth related defects in plan-view and cross-section because the defect contrast is greatest for this reflection. The resolution of the defects was increased using weak-beam dark field (WBDF) imaging, where the sample is tilted such that s (deviation from Bragg condition) is large, the planes in most of the specimen is titled away from Bragg condition. However, as seen in Figure 2-3, the planes near the core of the dislocation are bent back into Bragg condition to yield contrast [Wil96]. This technique is termed Weak-Beam Dark-Field (WBDF) and was taken at g.3g condition. This imaging condition was used to image all PTEM samples in this work.

Regrowth related defect density analysis. PTEM quantification was carried out to obtain dislocation density in both Strained Si and Strained SiGe samples. Strained Si samples exhibited misfit dislocations that span in the <110> direction and Strained SiGe samples exhibited dislocation networks in the form of a large connected array rather than individual dislocations. In order to quantify both types of dislocations in a similar manner, a linear (rather than area) quantity was measured.

PTEM images were taken under g.3g WBDF mode. Each sample was imaged ten times in different areas of the specimen, in order to get a good statistical account of the defect density.

Each sample condition was taken at the same magnification of 20,000X, 50,000X, 100,000X, or 150,000X, depending on the density of the dislocations. The images were printed out on 8 x 10 inch sheets. For the strained Si samples, a ruler was placed in the <110> directions, both parallel and perpendicular to the g vector, the number of defects intersecting the ruler was counted over a length and recorded. This was done for all ten images. Each of the ten micrographs was counted three times to include variation within a single micrograph. The average of these 30 observations was used to calculate the value of linear defect density for each sample condition. Error bars equal to one standard deviation for all observations was applied to each data point. For the strained SiGe samples, the measurements were taken perpendicular to the g vector. The dislocation network was imaged using g_{220} and the images show a stronger linear alignment along one direction. A ruler was placed perpendicular to this direction and the number of defects intersected with the ruler was then counted per unit length. The results and error bars were determined in similar manner as for the strained Si samples. For clarification, it should be noted that the defect density quantified for the strained Si was misfit dislocations while the strained SiGe the defects were regrowth related defects. The misfit dislocations in the strained SiGe were not visible due to the high density of regrowth related defects. This is discussed further in Chapter Five.

Trapped interstitial concentration analysis. PTEM were used to image end of ranges defects consisting of dislocation loop and {311}s. The trapped interstitials content in both of these defects can be quantified by the following method. First, the quantification of the dislocation loops will be discussed followed by the {311} defects.

End-of-range loops are most commonly images using WBDF g_{220} imaging mode. The images were taken at 150,000X and printed on 8 x 10 inch sheets. A grid consisting of 0.5 cm

squares were printed out on a transparency and used to determine the area fraction of loops. This transparency was superimposed onto the printed out image and used to count the defect. The number of nodes that intersect a loop were counted and divided by the total number of nodes to yield an area fraction occupied by individual loops. The area fraction is then multiplied by the planar atomic density of the {111} plane (~1.5×10^{15} atoms/cm^2) will give the concentration of trapped interstitials in (atoms/cm^2) bound by dislocation loops. The error of this measurement can be reduced by using finer grid size and choosing multiple areas and averaging the concentration of loops. Three areas per sample were counted and determined to have a 10% error within a sample set.

Next, the {311} defects are counted in a different manner. Again, the g_{220} WBDF condition was used to image the PTEMs. However, some families of these defects will be invisible for g parallel to their length. Only using the g_{220} reflection will lead to lower defect count and higher error in calculation roughly 30%. The images were taken at 150,000X and printed out on 8 x 10 inch sheets. A transparency was placed over the image and the length of the {311} was traced with a fine-tipped marker. Note that the {311}s parallel to the sample surface are actual length and the {311}s that are not parallel are projected lengths (45º to the surface). The length of the defects that are not parallel to the surface will be multiplied by 1.4 and then added to the rest to yield total length of interstitials in the sampling area. Assuming 26 atoms per nm of the {311}s, the total number of trapped interstitials/cm^2 can be determined. The total trapped interstitial concentration in this work is the sum of both dislocation loops and {311}s. Note that there were no end-of-range defects observed in the strained SiGe samples. Therefore, this calculation was only done for the strained Si samples.

X-Ray Diffraction

X-Ray diffraction (XRD) is a versatile, non-destructive analytical technique used to study crystallographic properties, chemical composition, and physical properties of thin film and bulk materials. XRD was used in this work to monitor the change in strain magnitude post processing.

The strained layers in this work are pseudomorphically grown with the substrate lattice continuing into the thin film. This continuation of substrate lattice parameter into the film (different equilibrium lattice parameter) is associated with incorporation of strain into the film layer. A measure for strain in the material is the difference in lattice parameter of the layer and substrate. The adaptation of the layer's lattice parameter to match the parameter of the substrate will cause a tetragonal distortion in the film unit cell. The layer unit cell extends or shrinks from its original value of a_L to $a_\perp$ in the out-of-plane direction and a_L to $a_\parallel$ in the in-plane direction, depending on whether a_L is larger or smaller than a_S, as shown in Figure 2-4. The degree of relaxation of the film is described by Equation 2-1.

$$\text{Strain Relaxation} = (a_\parallel - a_S) / (a_L - a_S) \tag{2-1}$$

Bragg's Law. In XRD, diffraction of the beam occurs when Bragg's Law is satisfied. Bragg's Law states that parallel planes with a distance of d will constructively interfere when the distance traveled is equal to n times the x-ray's wavelength, this relationship is presented in Equation 2-2.

$$n\lambda = 2d \sin \theta \tag{2-2}$$

A substrate containing epitaxial layers will result in additional peaks corresponding to the difference in lattice parameter to the substrate. The positions of these peaks are used to determine the d spacing for the layer and substrate. The lattice parameter can then be calculated

using the relation of d spacing to lattice parameter, a, shown by Equation 2-3. The miller index of the reflection is h, k, and l.

$$d_{hkl} = a/\sqrt{(h^2 + k^2 + l^2)} \quad (2\text{-}3)$$

The degree of relaxation can be calculated using the relationship shown in Equation 2-1. The quantified strain relaxation in the proceeding chapters are always made with reference to the as-grown state of the sample and not the theoretical strain state. Most of the materials were partially relaxed with misfit dislocation linear density of 5 x 10^4/cm equal to less than 1% strain relaxation as received.

Instrument and setup. A Pananalytical MRD X'Pert was used to obtain rocking curves and reciprocal space maps. Previous studies have also employed rocking curves to study the strain relaxation observed in the strained silicon capping layer using pseudomorphic Si/ $Si_{1-x}Ge_x$ structures [Cro04, Phe05] and strained SiGe on Si [Few82, Mat91]. XRD rocking curves and reciprocal space maps scan across a range of $\omega/2\theta$ angles and report the angle where diffraction occurs, called the Bragg angles.

The x-rays have a wavelength of 1.54 Å ($Cu_{K\alpha 1}$ transition) and are directed through a series of (220) Ge crystals to produce a monochromatic beam. The incident angle of the x-ray to the sample is ω and the diffracted beam is 2θ relative to the incident beam. For both rocking curves and space maps, the Hybrid Mirror is used as the primary optic. It gives the best resolution and monochromates the beam such that only Cu $K_{\alpha 1}$ radiation is used. Only single crystals will give any detectable intensity using this setup. For the strained Si sample measurement, the secondary optics used were the rocking curve attachment with the triple axis. The triple axis mode places a channel cut germanium analyzer crystal before the detector. Under this configuration, the diffracted beam undergoes three (022) reflections before entering the detector. The acceptance

angle of the germanium analyzer crystal is 12 arcseconds. For the strained SiGe samples measurement, the secondary optics consisted of the open detector of the rocking curve attachment and the brass slit.

Rocking curves. Rocking curves (RC) are acquired by rocking the sample through the incident angle, ω, while moving the detector, 2θ. Doing so allows the diffracted peaks of the substrate and film to be distinguished. The peak positions and intensity are dependent on the material's composition, crystalline quality, and thickness. The peak width is broadened by imperfections in the crystal such as faults and defects. Thus, the peak width can account for the film thickness in the case of a pseudomorphic layer. The peak width is observed to decrease with increasing thickness. Additionally, for very thin layers fringing is observed to the left and right of the main peak. The fringing is due to x-ray interference reflected from surface of the film and the substrate-film interface. The distance of the fringes can also be used to determine the layer thickness and were observed in the strained SiGe samples. These fringes can be washed out if crystalline disorder associated with faults, dislocations, or surface roughness exceeds a critical level. The thickness, Ge concentration, and roughness of the layers can be simulated using the Epitaxy software designed for the X'Pert system. To simulate these parameters accurately, the degree of relaxation of the film must be known and measured using a different technique.

Q scattering vector. The XRD scans are presented in terms of scattering vectors, Q. A symmetric θ/2θ scan, rocking curve scan, and radial scan is represented in Figure 2-5. The symmetric θ/2θ scan only has a nonzero component for the scattering vector normal to the substrate surface. A rocking curve, however, also has nonzero in-plane component, Q_x, for all ω angular positions except when ω = 2θ/2. The last scan type, radial scan, the Q vector has the

same tilt with respect to the sample surface during the entire measurement. It is sometimes convenient to report analysis in Q vector notation because it is more directly translatable for comparison with other measurement methods. The relation between instrumental coordinates, ω and 2θ, and the scattering vectors, Qx and Qz, is presented in Equation 2-4.

$$Q_x = K\,[\cos(\theta - \omega) - \cos(\theta + \omega)]$$
$$Q_z = K\,[\sin(\theta - \omega) + \sin(\theta + \omega)] \qquad (2\text{-}4)$$

The Q notation and the reciprocal space map combined in one plot is shown in Figure 2-6. The region that is accessible for data collection can be represented by a hemisphere in Q space having $-2K \leq Q_x \leq 2K$ and $0 \leq Q_z \leq 2K$ and obeying $Q_x^2 + Q_z^2 \leq 4K^2$. The region of reflection is divided from region of transmission by two smaller hemispheres of radius K (shaded in gray) that are centered at $Q_x = -K$ and K. These two gray areas cannot be accessed because they lie in the transmission region. In this figure there are point labeled by the Miller indices of the Bragg reflections that are observed for the alignment of Si (001). The 00l reflections are allowed and occur along the Qz axis and can be measured only with a symmetric θ/2θ scan. This combination plot can be generated for any substrate with orientation (*hkl*) using the instrument software. The set of Miller indices that are observed will depend on both the substrate orientation (*hkl*) and the direction of alignment of the sample with the x axis of the diffractometer.

Reciprocal space map. Reciprocal Space Maps (RSM) was used for samples with lower film peak intensities such that the peak position from the substrate can be distinguished. RSM are subsequent ω/2θ rocking curves over a range of ω angles or subsequent radial scans, presented in Figure 2-7. The RSM obtained in this study were from subsequent rocking curves. RSM is performed such that the investigated Bragg reflection is fully mapped in Q space. In other words, it is not only monitored by one rocking curve crossing it rather the entire vicinity of

the Bragg reflection is measured. RSM can provide further structural information of epilayers than a rocking curve alone. RSM measurements were preferred over RC for the asymmetric reflections for the strained Si samples for two main reasons. First, the X-ray intensities for the strained peak post processing were too low to determine the exact position of the peak. Second, if relaxation process also induced some tilt or twist within the layer, the position of the strained layer peak will no longer be accessible using RC. The RC measurements are aligned to the substrate peak due to its high intensity and known Bragg reflection position. If the layer does undergo some change in twist or tilt angle, the direction of elongation of Bragg reflection will also change in reciprocal space with respect to the substrate and may not lie in the area of the RC measurement.

The RSM are generally plotted in terms of the scattering vector, Q. An example of a RSM plot, presented in Figure 2-8, shows the position of the layer with respect to the substrate in terms of the layer being in a fully strained or fully relaxed state. One can draw a line between the fully strained (R=0) and fully relaxed (R=1) peak positions, this line is called the Relaxation line. The layer will appear within the area of this line depending on the degree of relaxation observed. The percent strain relaxation observed by the layer can also be determined by the position of the peak within the relaxation line by taking the ratio of the change in position from fully strained over the full length of the relaxation line. The as-grown (113) RSM for Si on $Si_{0.7}Ge_{0.3}$ is presented in Figure 2-9. The figure indicates the position of each layer's peak. The out-of-plane lattice misfit appears as a peak separation between the layer and substrate along Q_z. and the in-plane lattice misfit is measured along Q_x [Pie04]. Thus, the strained film is fully strained when the strained Si and relaxed SiGe peak are aligned vertically, as indicated by the

vertical line. Strain relaxation post processing is observed by movement of the strained Si peak towards the Si substrate peak.

Errors. The errors associated with X-ray measurement are dependent on the user, measurement step size, peak broadening and variation within the wafer. Before acquiring any data, all axes of the instrument must be aligned, usually to the substrate peak or sample surface. One can introduce a large error if the instrument is misaligned. This is especially true for measurements during an absolute scan. However, the RC and RSM measurements are relative scans. The RSM and RC measurements carried out used the Si substrate Bragg position as reference and all axes of the instrument were aligned to it. Thus, the epilayers were always measured relative to the Si substrate peak. The error of measurement due to user variability and alignment variations were tested. The variation between users was less than ±1% Ge which roughly translates to a 0.03% strain relaxation error. The error introduced by the step size for the RSM measurement was less than 0.5% strain relaxation. Another error to consider is the determination of the peak position when the peaks are relative broad. Thus, the degree of relaxation was also measured by average misfit spacing using PTEM micrographs, discussed in Chapter Three, and compared to the XRD measurements. There exists a ~1% strain relaxation difference between the two measurement techniques. Additionally, there was a 0.5% Ge distribution across the wafer which was also considered. Finally, taking all the errors into considering an error of ±2% strain relaxation was estimated for the XRD measurements.

Sensitivity of measurement. Epitaxial thin films exhibit a high degree of crystalline perfection. However, deviations from a perfect crystalline lattice do occur and the sensitivity of the measurement of this deviation is the focus of this section. In order for accurate measurement of closely spaced peaks that occur in the diffraction of epilayer-substrate materials, special

experimental equipment must be introduced. Crystal monochromators and analyzers have to be introduced in the beam path which allow selection of x-rays that are only Bragg reflected from a single crystal or a set of them. Figure 2-10 clearly shows the need for achieving higher resolution to investigate thin films used in electronics [Bar83]. The highest resolution possible for the measurement setup used in this work is 10^{-4} for measured d-spacings. However, for onset of relaxation to be measured a sensitivity of 10^{-7} is needed. Therefore, it should be noted that X-ray measurement cannot determine very low changes in strain relaxation nor can it be used to determine the onset of relaxation.

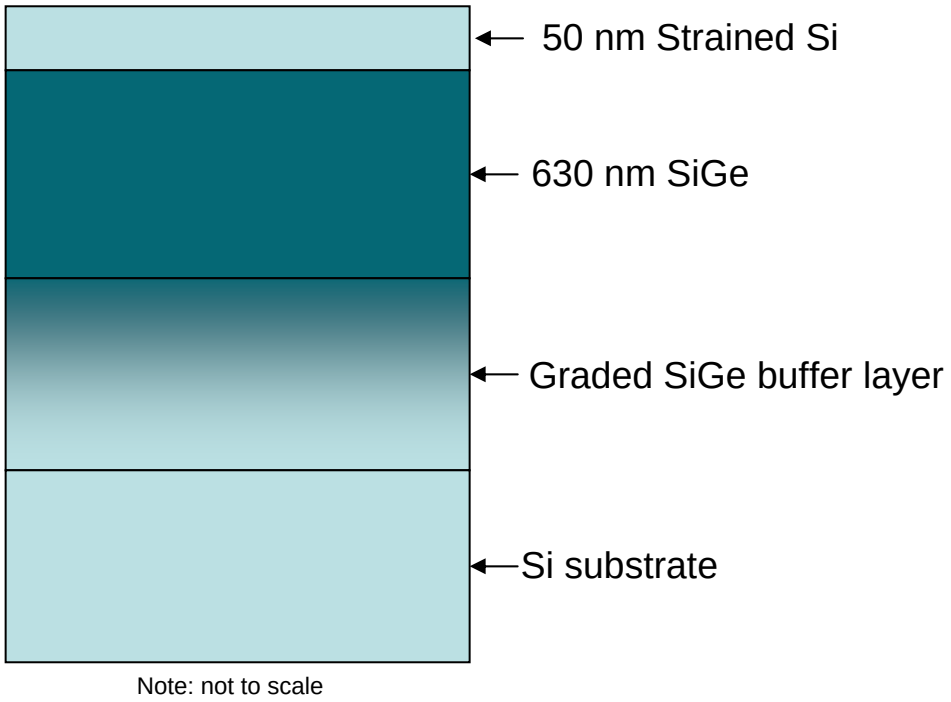

Figure 2-1. Schematic representation of biaxial tensile strain structure used in this work.

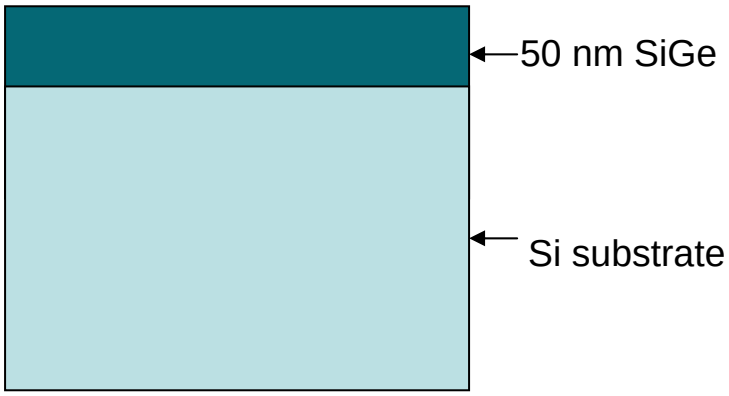

Note: not to scale

Figure 2-2. Schematic representation biaxial compressive strain structure used in this work.

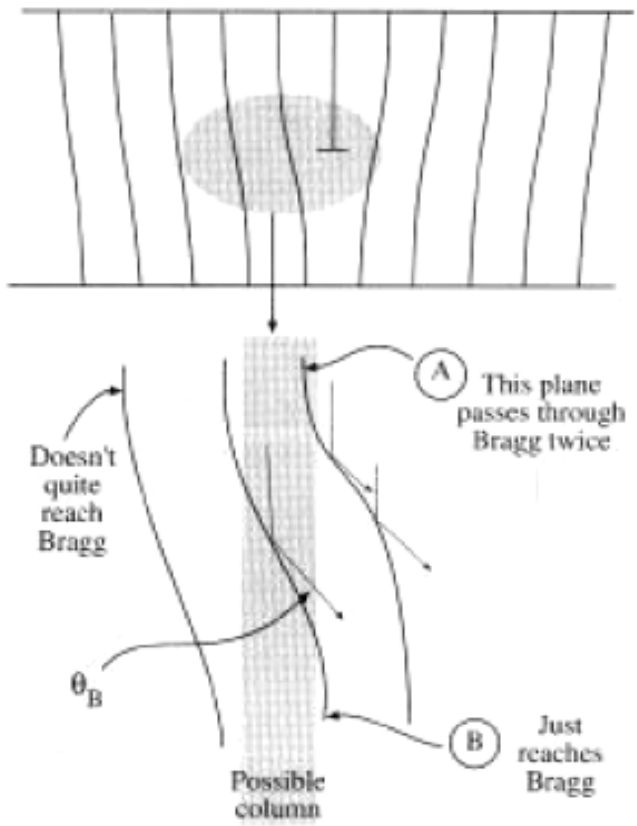

Figure 2-3. Principle behind weak beam dark field imaging technique in TEM for an edge dislocation. High intensity occurs close to dislocation core because planes are bent back to Bragg condition [Wil96].

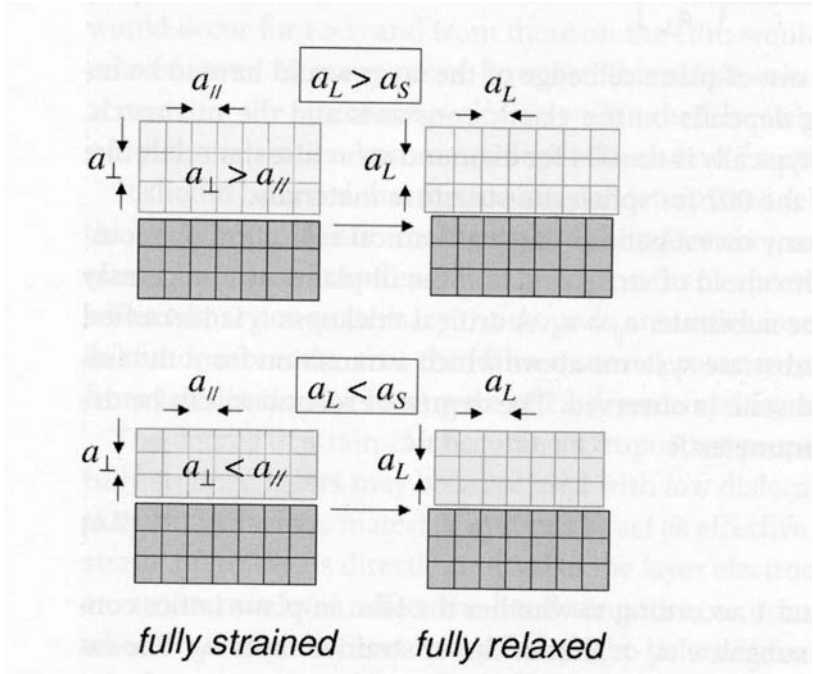

Figure 2-4. Strained (left) and relaxed (right) layers for film layer in compression (top) and in tension (bottom) [Bir03].

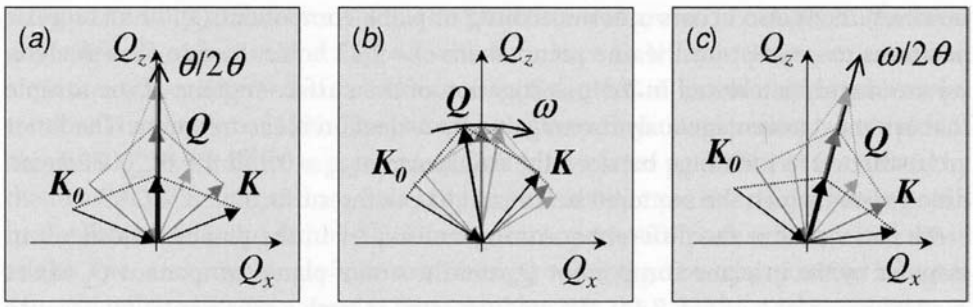

Figure 2-5. Schematic representation of (a) symmetric θ/2θ scan, (b) rocking curve scan and (c) radian scan in plane of momentum transfer [Bir03].

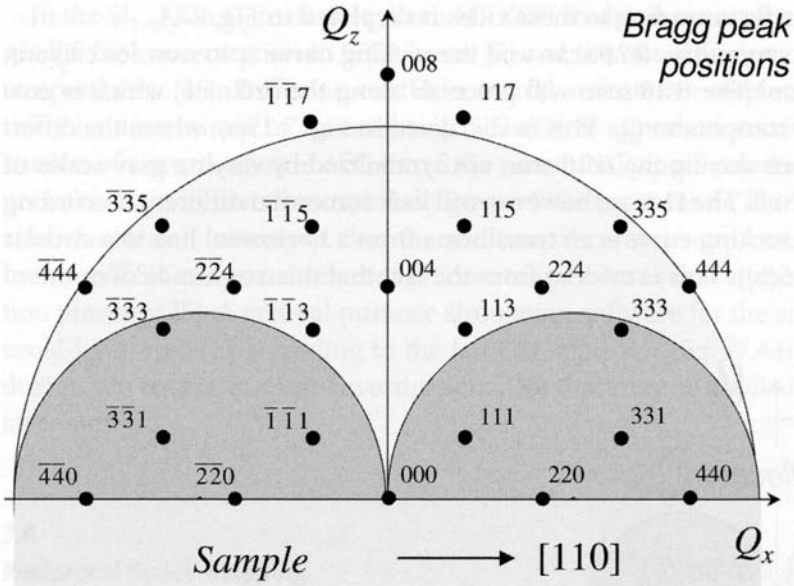

Figure 2-6. Combined plot of Qx,Qz plane and position of Bragg peaks for an epitaxial film on Si (001) substrate [Bir03].

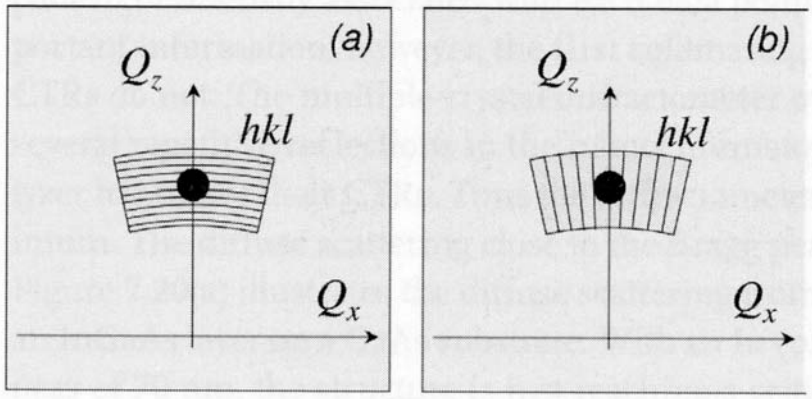

Figure 2-7. Two ways by which reciprocal space maps may be recorded are by either (a) subsequent rocking curves or (b) subsequent radial scans [Bir03].

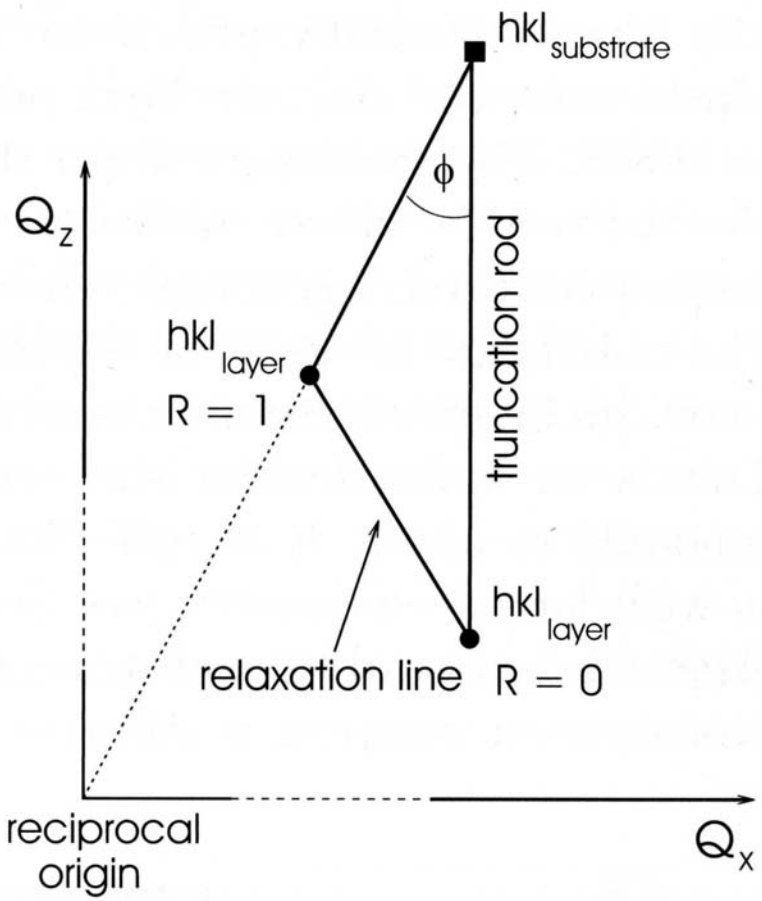

Figure 2-8. Representation of a reciprocal space map shows the relative positions of the layer with respect to the substrate for fully strained and completely relaxed system in reciprocal space [Pie04].

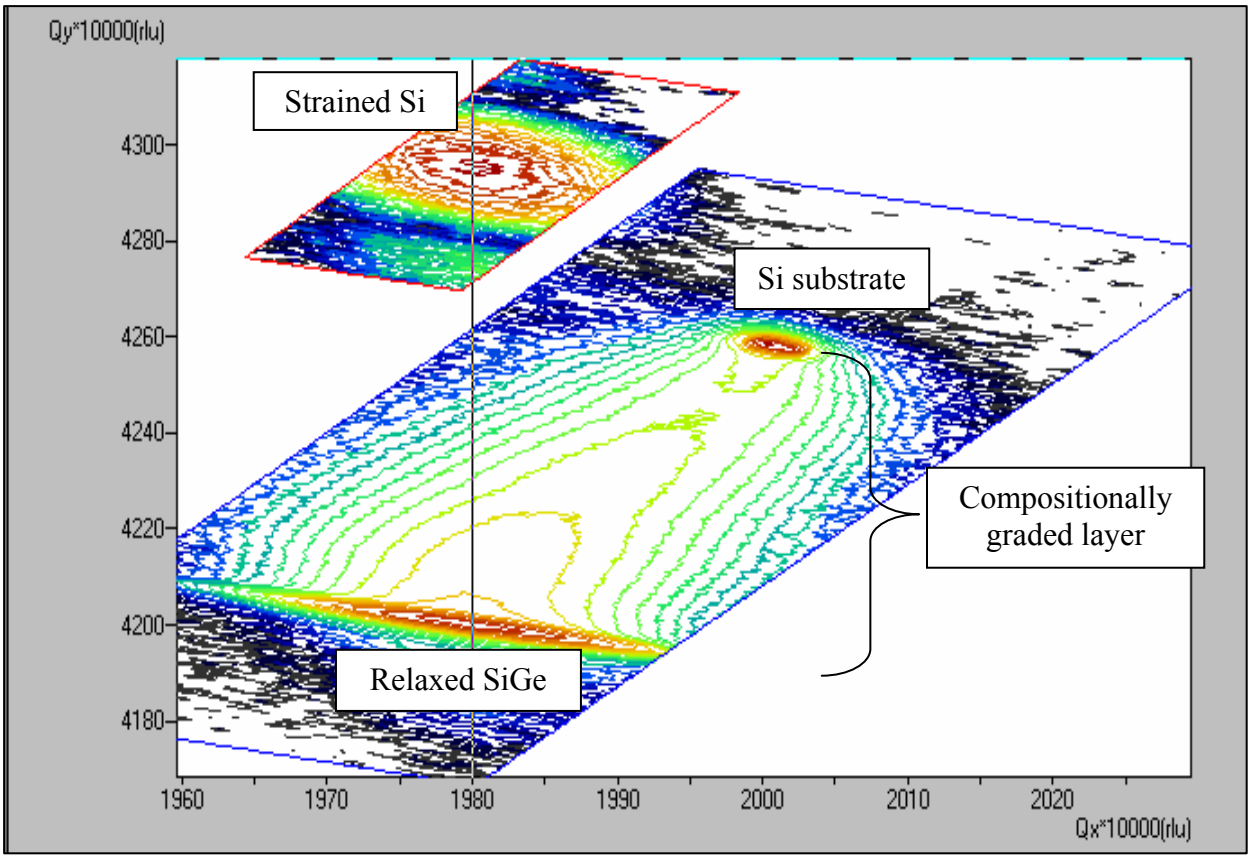

Figure 2-9. (113) Reciprocal space map of as-grown Si on $Si_{0.7}Ge_{0.3}$ indicating the location of each peak.

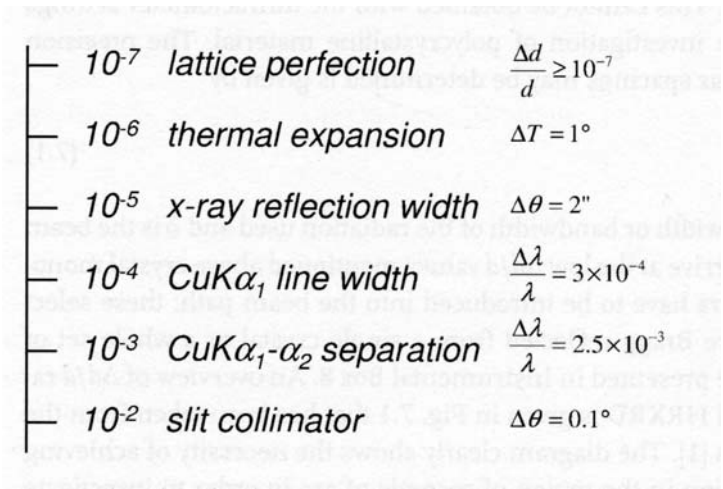

Figure 2-10. Relative d spacings and precision according to Bartel [Bar83, Bir03].

CHAPTER 3
TENSILE STRAIN: DEFECT NUCLEATION AND TEMPERATURE DEPENDENCE

Strained silicon technology offers enhanced hole mobility due to a decrease in the average effective mass and decreased inter-valley scattering [Nay96]. Strain can be induced in a Si capping layer through lattice mismatch between a $Si_{1-x}Ge_x$ virtual substrate and the silicon film, provided the strained overlay is grown less than the critical thickness [Peo85]. Obeying this criterion, the interface will be in perfect atomic registry and maximum strain will be present. After thermal processing, however, the strain energy in some heterostructures can decrease through strain relaxation via the propagation of threading dislocations and formation of misfits [Koe01, Sam99, and Sug01]. Additionally, relaxation can also be caused by Ge diffusion into the strained overlay during thermal processing. While numerous studies have reported results on silicon recrystallization and regrowth in $Si_{1-x}Ge_x$ and Si bulk systems [Atz94, Pai91, Sug04], the stability of strained silicon after amorphization and recrystallization is not well understood. Ge interdiffusion and ensuing strain relaxation has been shown to be especially dramatic when the collision cascade of an amorphizing implant overlaps the $Si/Si_{1-x}Ge_x$ interface. Previous studies suggest that the implantation through the heterostructure interface process creates point defects which act as nucleation sites for relaxation-induced dislocations and/or may assist Ge interdiffusion by an interstitial mediated mechanism [Van05].

The behavior of strained structures where the implant is constrained within the strained layer, however, is not well known. This experiment focuses on determining the stability and degree of relaxation after amorphization and recrystallization within a strained silicon layer. This knowledge will assist in defining the process window for Stress Memorization Technique (SMT) and other process-induced strain applications.

Several variables are likely to affect the degree of strain relaxation. Some of these variables include point defect population, initial strain, critical strain for enhanced strain relaxation, and proximity of point defects to heterostructure interface. This chapter will discuss the effect of initial strain and point defect population on strain relaxation. The next chapter will discuss the effect of implant proximity to the heterostructure interface on relaxation.

The experiments in this chapter will determine if there is a critical strain for Solid Phase Epitaxial Regrowth (SPER) breakdown and, if so, by what mechanism. The primary concern centers on the effect of the EOR on the relaxation process. Thus, an isochronal study was carried out at a temperature at which the evolution of excess interstitials into dislocation loops was sampled. By monitoring the quantity of EOR damage in the strained vs. unstrained layers and corroborating the measurement with the relaxation defects known as misfits the role of the extended defects on strain relaxation could be understood. Second, how any defects present were nucleated. Finally, the thermal behavior of the dislocations was explored.

Experimental Design

Strained Si structures were grown on relaxed $Si_{1-x}Ge_x$ (Ge fractions of 0, 10, 20, and 30) virtual substrates via Molecular Beam Epitaxy (MBE) at the University of Aarhus, Denmark. 100mm 0.005-0.020 ohm-cm (100) n-type Czochralski-grown silicon wafers were used for substrate wafers. Virtual substrates with low threading dislocation densities were grown with compositionally graded buffer layers which incorporated Ge at a rate of 10 at.% per micrometer at temperatures of 750 °C to 800 °C [Fit91]. A 630 nm thick fully relaxed $Si_{1-x}Ge_x$ layer of corresponding composition was then grown on top of the buffer layer, followed by a 50 nm strained silicon capping layer. The strain of the structures was experimentally determined using the in-plane lattice parameters, $a_{Si\text{-}cap}$ and a_{SiGe}, obtained from HRXRD. The change of strain is reported in terms of % strain relaxation, obtained by the relationship in Equation 3-1.

$$\% \text{ Strain Relaxation} = (a_{Si\text{-}cap} - a_{SiGe}) / a_{Si} - a_{SiGe} \times 100\% \quad (3\text{-}1)$$

The silicon results from this analysis show that the capping layers grown on $Si_{1-x}Ge_x$ with Ge fractions of 0, 10, 20 and 30 correspond to a Si layer strain of 0, 0.37, 0.74, and 1.1% strain, respectively. XTEM analysis was also used in order to verify proper growth of strained films.

The structures were then implanted with Si^+ at an energy of 12 keV and a fluence of $1x10^{15}$ atoms/cm^2 to generate a 30 nm continuous amorphous layer confined within the strained layer. Next, isothermal and isochronal anneals were performed in a quartz-tube furnace under an inert N_2 ambient environment. Three experiments were designed to study specific factors that may affect the relaxation process.

The first experiment consisted of 30 minute isochronal anneals performed at 500, 650, and 800 ºC and isothermal anneals at 800 ºC for 5, 30 and 300 minutes. In implanted Si, the supersaturation of interstitials leads to the evolution and agglomeration of extended defects when annealed above 650 °C. This experiment studied the effect of the evolution of these extended defects within a strained structure. This experiment was also used to determine the critical strain necessary for breakdown of SPER.

The second experiment consisted of an isothermal study at 500 ºC which was performed to investigate defect nucleation and propagation in the strained film during the regrowth process. Anneal times for this study were 15, 30, and 45 minutes. For these times and temperature, the regrowth velocity was slow enough that the amorphous-crystalline (a-c) interface could be captured before complete regrowth had taken place. This allowed observation of defects as they nucleated and grew with the use of XTEM and PTEM.

The third experiment consisted of a 30 minute isochronal study to investigate the thermal behavior of the relaxation process and how it compared to bulk processes. Temperatures of 500,

575, 650, 725 and 800 ºC were used for this experiment. The highest strained sample, 30% Ge, was used in this isochronal study as it would show the maximum effect, if any.

For all experiments, a Pananalytical MRD X'Pert was used to obtain HRXRD rocking curves and reciprocal space maps to study the strain relaxation. Previous studies have also employed rocking curves to study the strain relaxation observed in the strained silicon capping layer using pseudomorphic Si/ $Si_{1-x}Ge_x$ structures [Cro04, Phe05]. However, further investigation determined space maps to be a preferable technique for the measurement of annealed samples. Reciprocal Space Map (RSM)s are compilations of rocking curves taken at a range of ω positions to create a 2D map of intensity in the vicinity of the Bragg reflection. The RSMs allows the observation of very low intensity peaks from the strained silicon layer that rocking curves do not clearly obtain. Using these maps, the relaxation of the layer can be directly observed by monitoring the shift of the strained silicon peak toward the silicon substrate. Additionally, the crystalline integrity of the layer can also be monitored by observing any broadening of the peak that would indicate a disordered or defected layer [Pie04]. Therefore, space maps are preferred for multilayered structures because the lattice parameters can be obtained from peak position and the degree of relaxation obtained directly from the relaxation line (refer to Chapter Two).

A JEOL 2010F high-resolution transmission electron microscope (HRTEM) and a JEOL 200CX TEM were used to study cross-sections of the regrown layers (XTEM). Samples for XTEM were prepared using a Dual-Beam FEI Strata DB 235 Focused Ion Beam. XTEM measurements were used to confirm the amorphous layer depth and layer thicknesses as well as identify defects present. Plan-view (PTEM) samples were also prepared and imaged using a

JEOL 200CX operating at 200kV using g_{220} weak-beam dark-field imaging to quantify dislocation density and type.

Results and Discussion

As-Grown and As-Implanted Sample Analysis

The HRXRD (004) rocking curves for the as-grown structures are shown in Figure 3-1. The position of the diffraction peak depends on Ge composition and strain relaxation in the layer. The strained silicon peak appears on the right of the high intensity silicon peak and the relaxed $Si_{1-x}Ge_x$ is to the left. The plateau between the Si and the relaxed $Si_{1-x}Ge_x$ peaks is caused by the superposition of peaks from the compositionally graded buffer layer. The HRXRD results obtained indicate proper growth and strain levels for the heterostructures. However, PTEM investigation observed the presence of misfit dislocations corresponding to a relaxation of less than 0.01% strain, for all as-grown sample conditions. Therefore, the samples are only partially pseudomorphic. The strain relaxation observed in these as-grown samples, however, is below the detection limit of the X-Ray measurement technique and was not accurately measured using X-Ray methods [Bir03]. The sensitivity of the XRD measurements is discussed in Chapter Two. Note that the initial strain magnitude of the as-grown samples was used as reference to calculate the relative degree of relaxation post annealing and implantation.

As-Implanted Sample Analysis

All samples discussed in this chapter were implanted with a 12 keV Si^+ implant at a fluence of $1x10^{15}$ atoms/cm^2. The implant was tailored to generate a continuous amorphous region confined within the strained layer as shown in Figure 3-2. XTEM of as-implanted Si on SiGe and Si control samples confirmed that amorphous depth did not vary with %Ge for this implant condition. The amorphous depths were within ± 1 nm for all samples within the error of XTEM measurement.

Critical Strain: SPER Breakdown Study

The relaxation behavior of all strained samples implanted with 12keV Si^+ was studied using a series of 30 minute isochronal anneals at 500, 650, and 800 ºC and isothermal anneals at 800 ºC. This experiment was used to determine the critical strain necessary for breakdown and the thermal behavior of relaxation (if observed).

The thermal stability of the highest strained as-grown (not implanted) $Si_{0.7}Ge_{0.3}$ structure was studied by subjecting samples to a 500 or 800 ºC anneal for 30 minutes. In both cases, no strain relaxation was observed. This result is in agreement with previously reported results [Koe01, Sam99, Sug01]. However, post-implantation and anneal, relaxation is observed for the highest strain structure as observed in the rocking curve spectra. Figure 3-3 shows a sequence of rocking curves for the as-grown, as-grown annealed and implanted annealed sequence for the $Si_{0.7}Ge_{0.3}$ structure at 500 ºC. Note that the rocking curves for the strained silicon peak post-implant and anneal have a weak signal, therefore, samples were further investigated with reciprocal space maps. The reciprocal space maps confirm that the rocking curves were only collecting the shoulder of the peak, or in the asymmetrical geometry cases, not collecting it at all. This is shown in the reciprocal space map in Figure 3-4, where the strain silicon peak is not in the area of the rocking curve and therefore gives a poor signal. Accordingly, lattice parameters were extracted from the peaks on the reciprocal space maps using Bragg's Law. From these lattice parameters, the percent relaxation is calculated and is shown in Figure 3-5.

The $Si_{0.9}Ge_{0.1}$ and $Si_{0.8}Ge_{0.2}$ samples showed 100% retention of the original strain for all thermal conditions. However, after the 500 ºC anneal the $Si_{0.7}Ge_{0.3}$ sample showed partial relaxation in the (224) map and no relaxation in the (113) map. Thus, this observation indicates that the relaxation process is not homogeneous at 500 ºC. The average between these results was taken to calculate the percent relaxation. The PTEM analysis of the highest strained sample

($Si_{0.7}Ge_{0.3}$) showed regrowth related defects as well as confirming the results from HRXRD. After the 650 and 800 ºC anneals, the $Si_{0.7}Ge_{0.3}$ samples showed a clear trend of higher anneal temperatures yielding a higher degree of relaxation. The strained silicon peak also broadened significantly with higher temperature anneals indicating higher defect density.

The crystalline quality of the regrown layer was further studied using XTEM. After the 500 ºC 30 minute anneal it was found that 10 nm of amorphous material remained in the strained layer. This may have attributed to the varying results in the (113) and (224) reciprocal space maps for the $Si_{0.7}Ge_{0.3}$ sample. An assessment of a fully regrown layer at 500 ºC would give a better indication of its true degree of relaxation. After the 650 and 800 ºC anneals, the TEM micrographs indicate a fully regrown layer for all samples. XTEM analysis for all conditions of the $Si_{0.9}Ge_{0.1}$ and $Si_{0.8}Ge_{0.2}$ samples show that the regrown layer was of good crystalline quality. This confirms the HRXRD results. However, the $Si_{0.7}Ge_{0.3}$ samples show defects as a result of relaxation and SPER breakdown. The XTEM images, taken under g_{220} WBDF condition, and PTEM images taken at g_{220} BF for the $Si_{0.9}Ge_{0.1}$ and $Si_{0.8}Ge_{0.2}$ sample and WBDF for the 30% Ge sample are shown in Figure 3-6. All samples were annealed at 650 ºC for 30 minutes. Note that the PTEM magnification for the $Si_{0.7}Ge_{0.3}$ sample is different than the other samples to better show defect morphology (refer to scale bars). The $Si_{0.9}Ge_{0.1}$ and $Si_{0.8}Ge_{0.2}$ samples exhibit misfit dislocations (as seen in the as-grown and anneal alone, not shown) in plan-view and a defect-free regrown layer in cross-section. The $Si_{0.7}Ge_{0.3}$ sample, however, shows the regrown layer full of defects which, using PTEM analysis, appear to be stacking faults. The XTEM micrograph show that these stacking faults extend between the surface and the heterostructure interface.

PTEM was used to study the strain relieving defects, specifically misfit dislocations, for both un-implanted and implanted samples post annealing to differentiate between the thermal

and implant contributions to relaxation. PTEM images, taken under g_{220} bright field, of the as-grown, as-grown anneal, and implant plus anneal samples are presented in Figure 3-7. The corresponding linear misfit dislocation densities are presented in Figure 3-8. The 10 and 20% Ge samples exhibit similar misfit dislocation densities for both the anneal only case and the implant plus anneal case. However, after implant plus anneal, the 30% Ge sample displayed misfit dislocation spacing much smaller than the equivalent anneal only case, this concludes that further relaxation took place after ion implantation. Upon relaxation, stacking faults are also observed in conjunction with an increase in misfit dislocations indicating further strain relaxation of the strained film than annealing alone. The nucleation of these defects will be discussed in the next section.

XRD/TEM discrepancy. Comparing the HRXRD results to the PTEM quantitative results for the anneal case only, a relative difference of 1-2 % relaxation is observed. Further analysis of these results sheds light on the cause of this discrepancy. The quantitative relaxation observed via HRXRD is shown in Figure 3-9. These results can be compared to the relaxation quantified using misfit spacing from PTEM analysis in Figure 3-8. The relaxation observed via PTEM is on the order of 1-2% of the initial strain for all samples after anneal only. The relative discrepancy between the HRXRD and the PTEM misfit spacing calculations are explained by both the manner in which these defects affect the X-ray spectra and relative sampling area. The quantitative HRXRD results in this work are calculated using the relative peak positions of the SiGe and strained Si peaks. Additionally, the presence of misfit dislocations may also be observed in the spectra via broadening of the peak which was observed for all annealed samples. Due to excessive peak broadening from the presence of misfit dislocations an additional margin of error is introduced into the HRXRD measurement technique. Also, the sampling area of the

PTEM and HRXRD differ greatly. The HRXRD results are an average of the lattice spacing over a cm^2 range whereas the PTEM results are site specific (a few μm^2). Thus, PTEM results are more susceptible to local variations in the wafer. Therefore, it should be noted that even though the HRXRD measurements indicate no relaxation, all samples undergo ~ 1-2% strain relaxation of the initial strain after annealing only. Additionally, for the 10 and 20% Ge samples post implant and anneal, the relaxation observed is also on the order of 1-2% decrease in strain. Thus, implantation related relaxation cannot be concluded to have occurred. The results from both TEM and HRXRD, however, conclude that the strain relaxation observed for the 30% sample is much greater than 1-2% of the initial value and is hence due to the break down of SPER via nucleation of stacking faults and a related increase in misfit dislocation density. Furthermore, by comparing the quantitative analysis of both techniques in Figures 3-8 and 3-9 similar trends between defect density and degree of strain relaxation is observed.

EOR evolution in the presence of tension. Further analysis of the PTEM samples at higher magnification indicates the presence of EOR damage in the strained samples similar to that seen in pure Si samples post implantation and anneal. The EOR evolution and population, however, does seem to be affected by strain. Figure 3-10 shows an anneal series at 800 ºC for Si control, 20% and 30% Ge samples. After similar anneal conditions, the EOR damage is observed to be much smaller in both size and number in the strained sample than the Si control. The total interstitial concentration trapped by both {311} defects and dislocation loops are quantified and presented in Figure 3-11. The Si control and unrelaxed Si on 20% Ge have similar concentration of trapped interstitials initially then deviate as seen in the figure. The {311} defects appear to be stabilized under tension but do not lead to dislocation loop formation, as seen by comparing the EOR evolution in Figure 3-10 for the pure Si and the Si on 20% Ge.

Tension seems to suppress the {311} to dislocation loop process which causes the deviation of trapped interstitial density from the initial concentration at 5 minutes. However, for the relaxed Si on 30% Ge, a lower number of interstitials are initially trapped indicating that some of the excess interstitials may be contributing to the relaxation process. These excess interstitials, a result of the implant, may be providing a source for the generation of extrinsic stacking faults which then nucleate more misfit dislocation. If this hypothesis is true, the proximity of the implant damage to the interface should affect relaxation by acting as a sink for the excess interstitials. As the implant damage is placed closer to the Si/SiGe interface, relaxation will increase and a higher density of misfit dislocation should be observed. This hypothesis was further analyzed by varying implant energy to change the proximity of the implant damage to the Si/SiGe interface and will be further discussed in the next chapter.

In summary, this study suggests that strained silicon can be amorphized and regrown without strain relaxation for all $Si_{1-x}Ge_x$ compositions up to $Si_{0.8}Ge_{0.2}$ for anneal temperature up to 800 ºC for 30 minutes. For the $Si_{0.7}Ge_{0.3}$ strained sample, the solid phase regrowth of the amorphous layer breaks down and results in the formation of regrowth related defects within the amorphous region and extending back down to the strained Si/ $Si_{1-x}Ge_x$ interface. This is the first observation of regrowth related defects extending below the original amorphous/crystalline interface in amorphized silicon. Furthermore, these defects are found to be primarily stacking faults rather than the traditionally observed hairpin dislocations. Since relaxation was only observed when the regrowth related defects were present, the results also suggest that the defects are contributing to the relaxation of the strained layer. Additionally, the EOR evolution seems to be altered in the presence of tensile strain when compared to Si control; the evolved dislocation loops in the strained structures are smaller in size and number. This indicates that, in

conjunction with a certain level of strain, excess interstitials, a result of the implant, are providing a source for the generation of extrinsic stacking faults which then nucleate misfit dislocations. The additional misfit dislocations then promote further relaxation than annealing alone. The possibility of excess interstitials acting as a source for misfit dislocation nucleation will be further explored in the next chapter. In conclusion, these results indicate that a critical misfit strain between 0.74% and 1.1% results in a breakdown of the SPER process and the formation of extended regrowth related defects that promote further relaxation.

Defect Nucleation Study

Strain relaxation and defect nucleation post SPER were observed solely for the highest strained samples. The mechanism of defect formation and the morphology of the amorphous-crystalline interface was studied using a series of isothermal anneals performed at 500 ºC. At this temperature, the regrowth velocity is slow enough such that images of the a-c interface at various stages prior to complete regrowth can be captured. $Si_{0.7}Ge_{0.3}$ samples were annealed for 15, 30, and 45 minutes and XTEM was used to observe the progression of SPER.

XTEM images of the samples are presented in Figure 3-12 in both bright and dark-field imaging mode. SPER at higher strain results in relaxation by nucleating regrowth related defects which propagate towards the surface with the advancing a-c interface. These defects are then observed to extend towards the Si/SiGe interface once SPER is complete. At 30 minutes, presented in Figure 3-12 (a) and (b), the a-c interface is observed to be planar and the regrowth related defect is located above the original a-c interface. At 45 minutes, as seen in (c) and (d), these defects begin to extend down to the epilayer interface promoting further strain relaxation. At higher anneal temperatures, these regrowth defects are determined to be stacking faults via XTEM and PTEM imaging. Figure 3-13 (a) and (b) show high-resolution XTEM images of

these faults extending from the surface to the epilayer interface. However, after a 500 ºC 45 minute anneal when regrowth is complete, no stacking faults were seen in PTEM micrographs.

The absence of stacking faults immediately after regrowth and presence of them after further annealing suggests that 30º and 90º Shockley partial misfit dislocation pairs are nucleated upon SPER to promote relaxation. These partials can then extend down to the epilayer interface via point defect diffusion. Upon further annealing, these partials glide apart and leave a fault between them. These faults are observed in PTEM to be relatively wide in length after anneals around 650 ºC. After further annealing at 800 ºC, the width of these faults is observed to decrease in conjunction with an increase in the 60º misfit dislocation. This observation suggests that the presence of stacking faults is promoting further misfit dislocation nucleation. The decrease in the width of the stacking fault in conjunction with increased perfect misfit density indicates that this process in conservative. The generation of partial misfit dislocation to provide strain relaxation in other strained bicrystal systems have been previously reported [Gut98, Gut01a, Hwa91] and were first theorized and observed by Cherns [Che74, Mat75]. Relaxation via partial dislocation generation usually occurs at higher misfit strain than the strain magnitude sampled in this work. Furthermore, the transformation of partial misfit dislocation to perfect misfit dislocations has been reported experimentally by Tamura in the GaAs on Si system [Tam96].

Plastic deformation in bulk Si via partial dislocations is well known. The deformation behavior has been studied using two different techniques [Rab00]. The first is microindentation, the drawbacks of this technique are that the stress tensor is unknown and the plastic region is localized in a small area making TEM analysis difficult. The second is deformation under a confining pressure which allows control of deviatoric and hydrostatic pressure. Both techniques

induce a compressive stress. At the lowest temperature of 500 ºC used in this work, the yield stress is ~400 MPa. For the highest temperature of 800 ºC this value drops significantly to ~20 MPa. According to this data, one might expect the thin films in this work to deform via dislocation at lower strain levels. However, from prior work in thin films it is known that higher stress in the films can be attained than predicted by the stress-strain studies in bulk silicon. The heteroepitaxy system is more complex and have other factors that contribute to the strain relaxation i.e. deformation. In bulk Si under ~500 MPa uniaxial stress induced by 4-point bend, plastic deformation was observed at low temperature (~550 ºC) [Phe04]. This results correlates well with the prior deformation studies carried out.

In summary, this experiment showed that regrowth related defects are observed for the highest strain case only. These regrowth related defects are confirmed to be stacking faults above 500 ºC. These defects are nucleated due to excess stress in the film that cannot support the SPER process. At lower anneal temperature and times; the regrowth related defects are observed to extend between the original a-c interface and the surface. After further annealing (at higher temperatures and/or longer times), the defects appear to extend from the surface down to the heterostructure interface and promote strain relaxation. Propagation of defects below the initial a-c interface has not been previously reported. Furthermore, it should be noted that the result in this work confirm prior work indicating that regrowth velocity is not affected by biaxial tensile strain [Phe05].

Relaxation: Thermally Activated Glide Process Study

The relaxation behavior of 30% Ge, 12keV Si^+ implanted samples was studied using a series of 30 minute isochronal anneals performed at 500, 575, 650, 725 and 800 ºC. Additional anneal times were carried out at the low and high temperatures to confirm that the relaxation process is linear at constant temperature. This experiment was designed to study the thermally

activated glide process of the SPER related defects and compare it to dislocation glide observed in bulk Si. Since this process is being measured via XRD it should be noted that the misfit dislocation propagation via glide is being indirectly measured through monitoring of degree of strain relaxation. Prior work has used in situ TEM measurements to determine the activation energy for glide [Hul89].

Prior studies pertaining to the plastic deformation of Si show that dislocation propagation follows Arrhenius behavior and occurs via dislocation glide. The activation energy for plastic deformation via dislocation glide process is 2.2 eV for pure Si [Ale68]. The activation energy for relaxation in strained Si measured via XRD is presented in Figure 3-14 as rate of relaxation versus 1/kT. The activation energy is found to be 0.7 ± 0.2 eV. This is much lower than the activation energy for plastic deformation in bulk Si. Comparatively, an activation energy for glide has been documented for a $Si_{0.7}Ge_{0.3}$ on Si thin film relaxation after an anneal only with a value around 1.1 eV [Hul89, Dod88] and 1.38 eV [Lei01], lower than the 1.8 eV determined for SiGe bulk material. The explanation proposed by Hull et al. [Hul89] is that as the dislocation density and anneal temperature increase, the propagating dislocations have to cross more and more orthogonal dislocations in a given length. These intersecting events are observed to impede propagation.

Activation energies for glide are the sum of kink formation and migration energies. The lower activation energy in thin films versus bulk material has been attributed to lower formation energies of kinks, due to the close proximity of the free surface and the relaxing interface. For the work presented here, since the nucleation of the defect is a result of the SPER breakdown, the activation energy may be dominated by the migration term. The formation energy term is thought to be negligible due to the defects forming as a result of SPER breakdown. This is

especially true since the activation energy is being measured by the relaxation rate which, in turn, depends on the rate at which misfit dislocations propagate. In conclusion, the relaxation observed is determined to be a result of dislocation nucleation and propagation initiated by the SPER breakdown with activation energy of 0.7 ± 0.2 eV.

Conclusion

The results in this chapter have shown three main points. First, under biaxial tension there is a critical strain for SPER breakdown that lies between 0.74 and 1.1% strain. Thus, strained silicon can be amorphized and regrown without strain relaxation for all $Si_{1-x}Ge_x$ compositions up to $Si_{0.8}Ge_{0.2}$ (0.74% strain). For the 1.1% strained ($Si_{0.7}Ge_{0.3}$) sample, the solid phase regrowth of the amorphous layer breaks down and results in the formation of regrowth related defects within the amorphous region. These defects then extend back down to the strained Si/ $Si_{1-x}Ge_x$ interface. This is the first observation of regrowth related defects extending below the amorphous/crystalline interface. Additionally, the EOR evolution and population seems to be altered in the presence of tensile strain; the evolved dislocation loops are fewer in number especially in the relaxed Si on $Si_{0.7}Ge_{0.3}$ sample. This indicates that, in conjunction with a certain level of initial strain, excess interstitials, a result of the implant, are providing a source for the generation of extrinsic stacking faults which then nucleate misfit dislocation. Thus, implantation increases misfit dislocation density and promotes further relaxation than annealing alone. The possibility of excess interstitials acting as a source for misfit dislocation nucleation will be further explored in the next chapter. In summary, these results indicate that a critical misfit strain between 0.74% and 1.1% results in a breakdown of the SPER process and the formation of extended regrowth related defects.

Second, defects are nucleated as the a-c interface progresses towards the interface during SPER, forming regrowth related defects. Once fully regrown, these defects propagate down to

the interface, promoting enhanced strain relaxation of the layer than annealing alone. The regrowth related defects are primarily stacking faults rather than the traditionally observed hairpin dislocations. Since strain relaxation was only observed when these regrowth related defects were present, the results suggest that these defects are contributing significantly to enhanced relaxation of the strained layer.

Finally, the relaxation process is a thermally activated glide process with activation energy of 0.7 eV. This value is significantly less than the 2.2 eV glide energy observed in bulk Si. The difference is theorized to be due to the formation term in this work being negligible since the defects are formed as a result of SPER breakdown. Thus, the activation energy in this work is dominated by the migration term. Overall, the relaxation process is concluded to be a result of dislocation nucleation and propagation via dislocation glide initiated by the SPER breakdown.

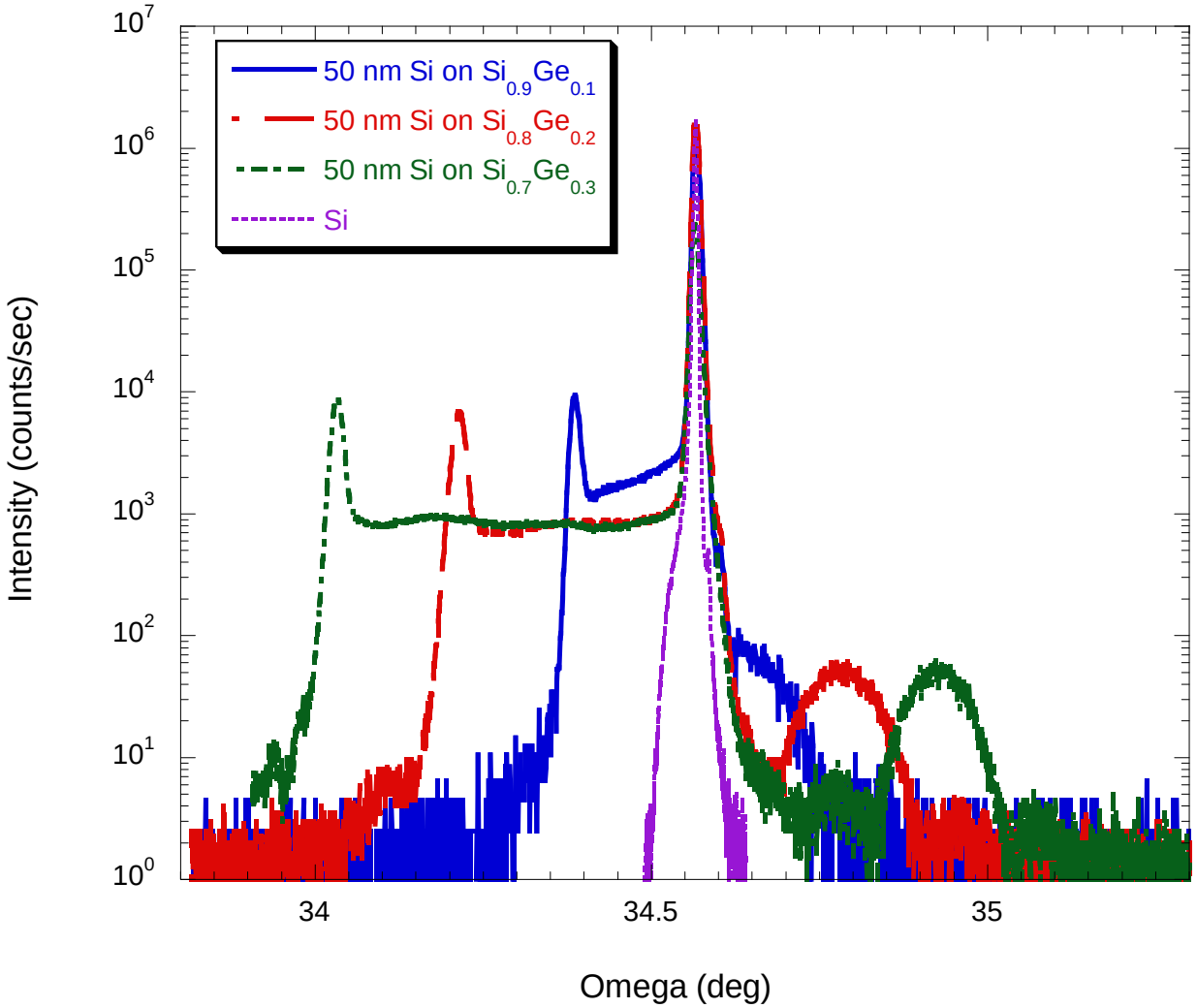

Figure 3-1. HRXRD (004) rocking curve of all as-grown strained Si on relaxed $Si_{1-x}Ge_x$ samples.

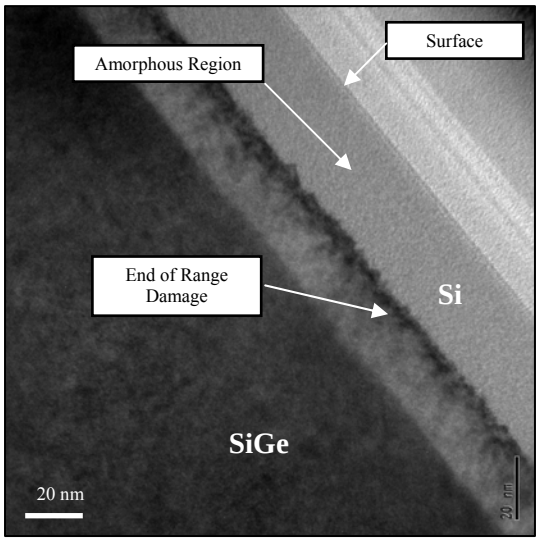

Figure 3-2. XTEM of as-implanted strained Si/ $Si_{0.7}Ge_{0.3}$ sample implanted with 12 keV Si^{+}.

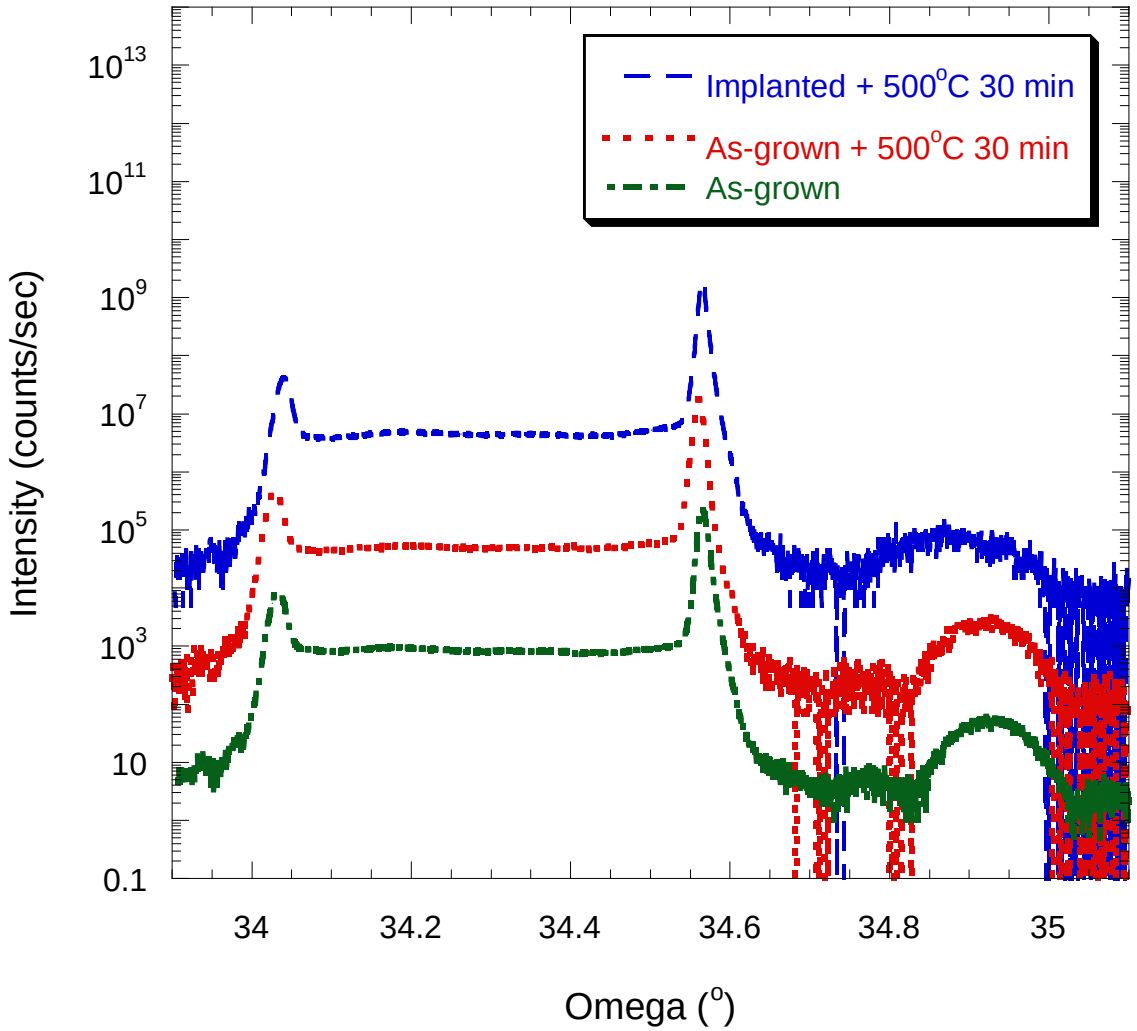

Figure 3-3. HRXRD (004) rocking curves of strained $Si/Si_{0.7}Ge_{0.3}$ structures annealed at 500 ºC for 30 minutes.

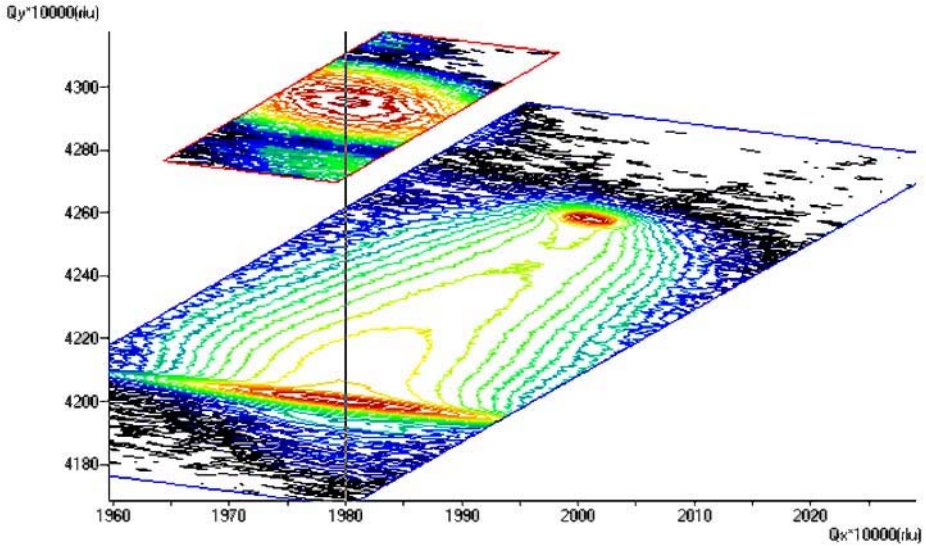

Figure 3-4a. HRXRD (113) reciprocal space map of as-grown strained $Si/Si_{0.7}Ge_{0.3}$ structure.

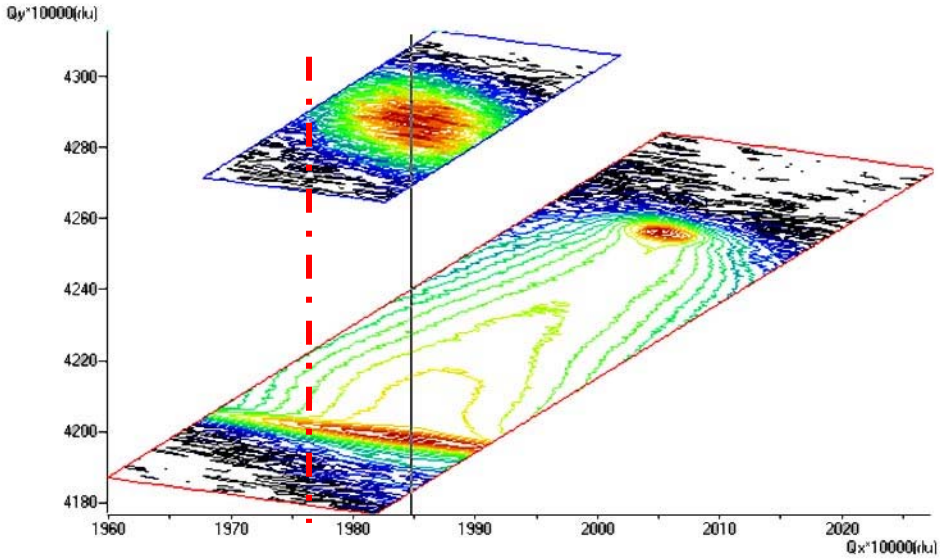

Figure 3-4b. HRXRD (113) reciprocal space map of strained $Si/Si_{0.7}Ge_{0.3}$ structure implanted with 12 keV Si^+ and annealed at 500 ºC for 30 minutes.

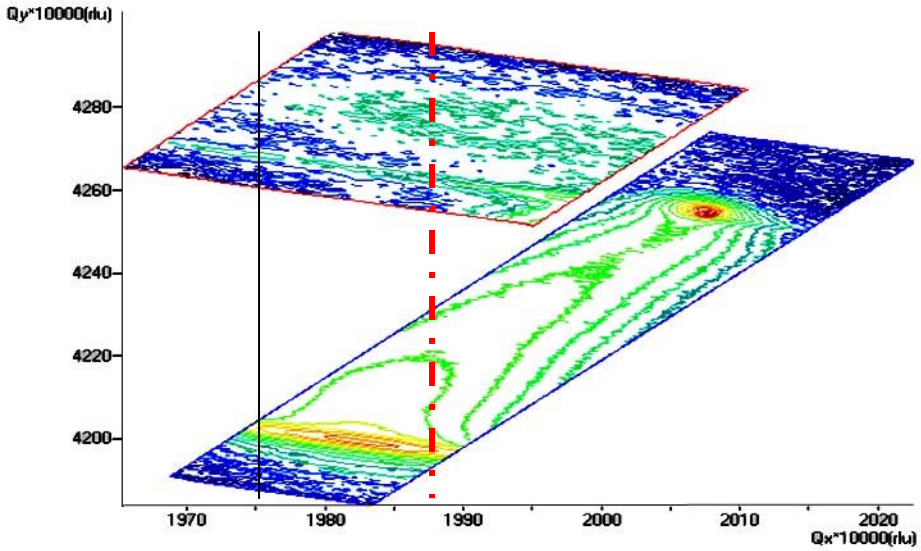

Figure 3-4c. HRXRD (113) reciprocal space map of strained $Si/Si_{0.7}Ge_{0.3}$ structure implanted with 12 keV Si^+ and annealed at 800 ºC for 30 minutes.

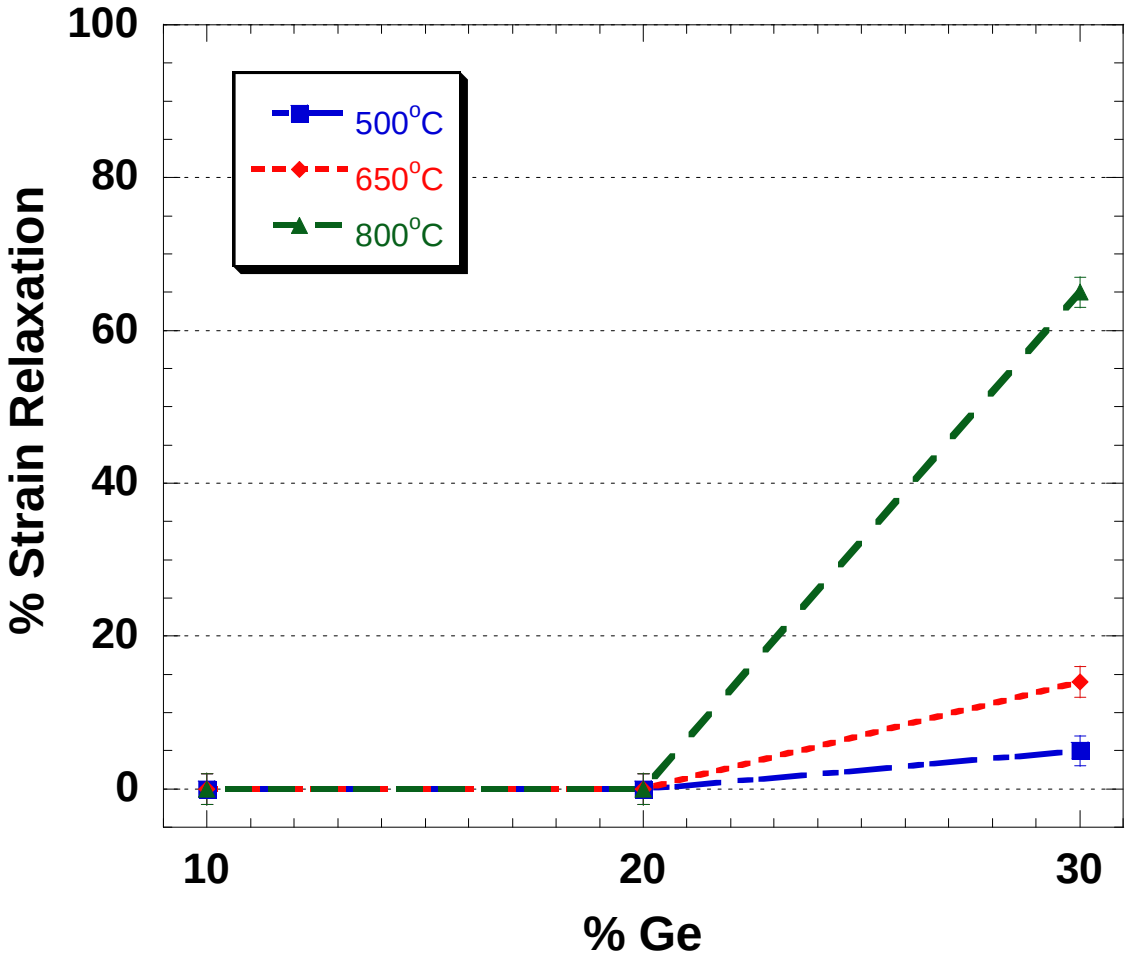

Figure 3-5. Strain Relaxation calculated via HRXRD RSM for strained Si on relaxed $Si_{1-x}Ge_x$ samples implanted with 12 keV Si^+ and annealed for 30 minute at temperatures indicated.

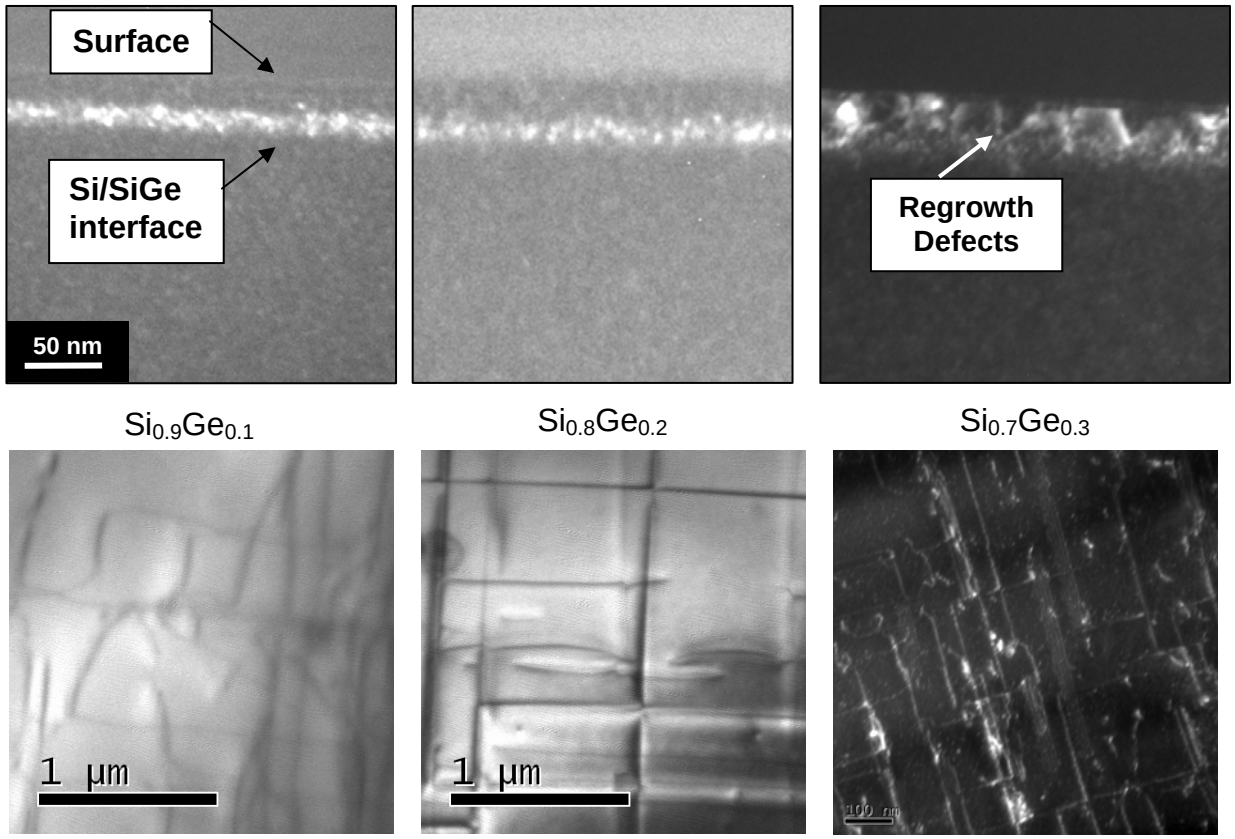

Figure 3-6. XTEM (top row) and PTEM (bottom row) for all strained Si on relaxed $Si_{1-x}Ge_x$ samples implanted with 12 keV Si^+ and annealed for 30 minutes at 650 °C.

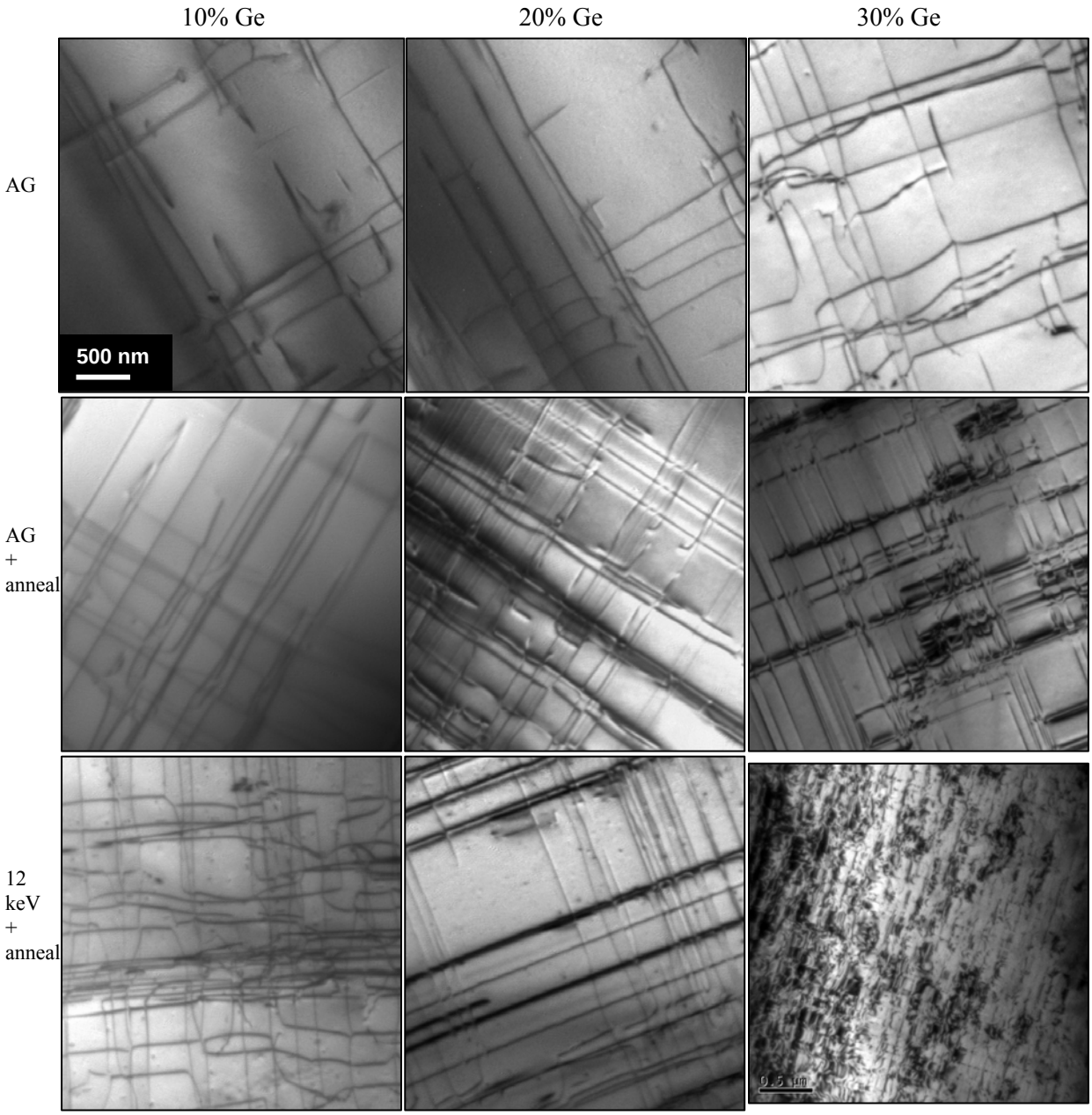

Figure 3-7. PTEM images for AG, AG plus anneal, and implanted with 12 keV Si^+ plus anneal for all strained Si on relaxed $Si_{1-x}Ge_x$ samples. All anneals carried out for 30 minutes at 800 °C.

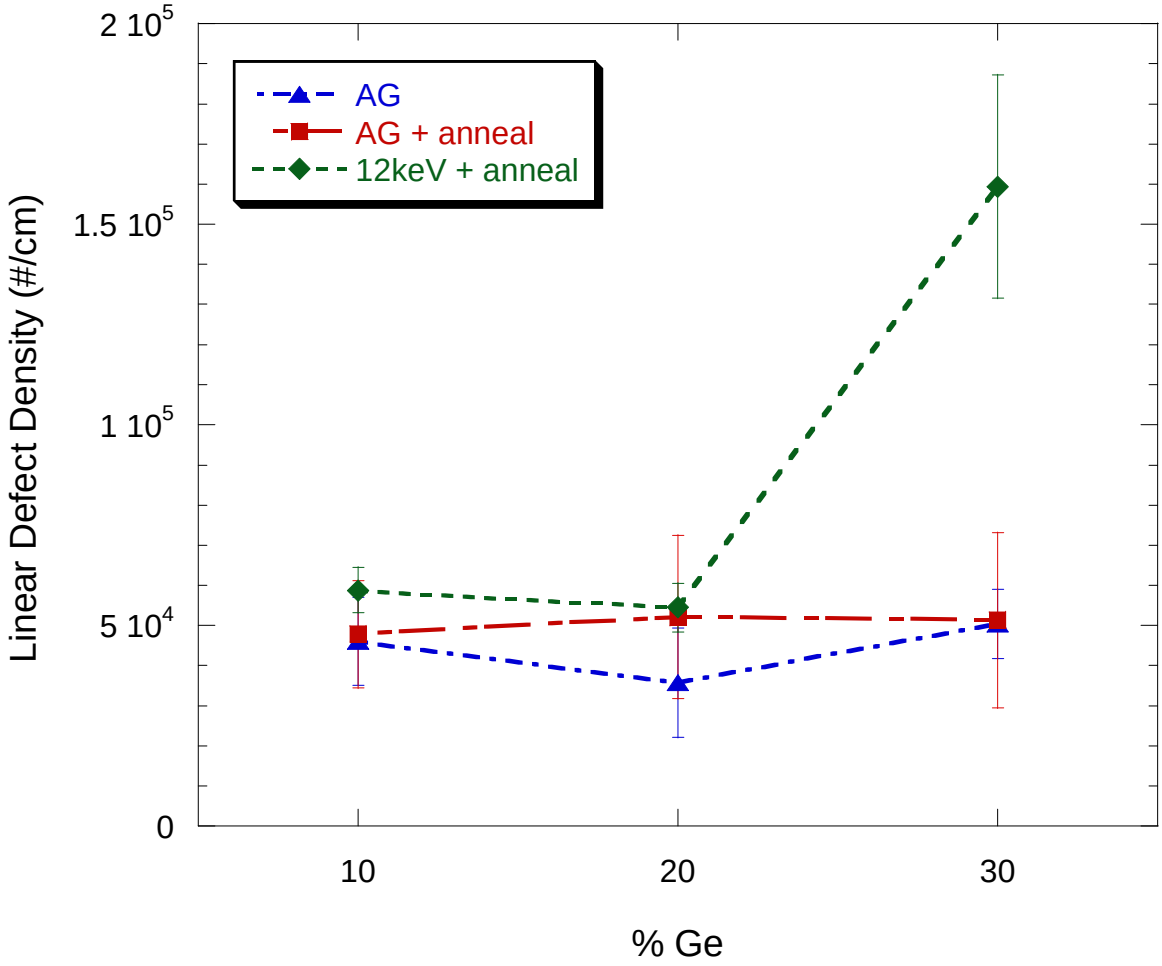

Figure 3-8. Linear defect density quantified using PTEM as a function of Ge concentration after 30 minute anneal at 800 °C.

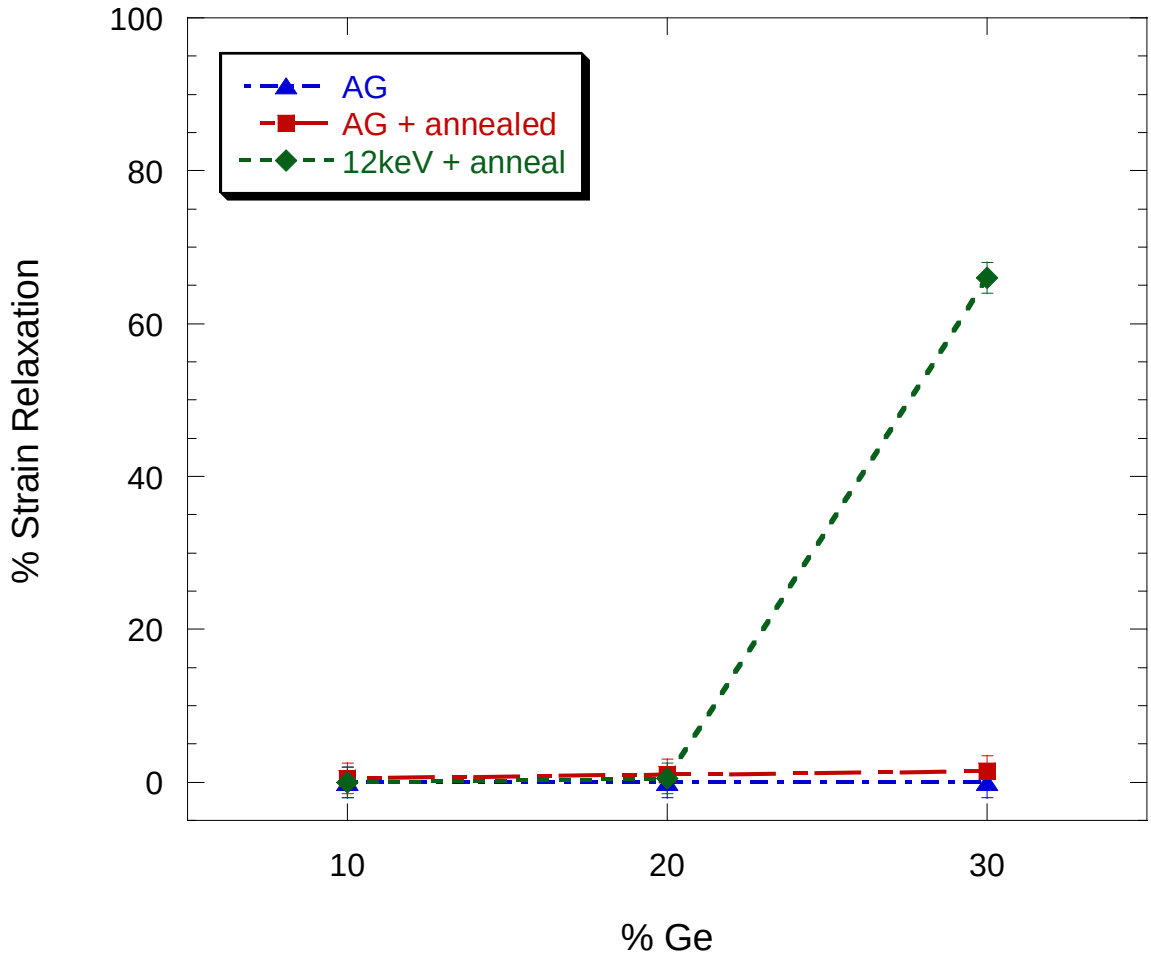

Figure 3-9. Percent strain relaxation quantified using HRXRD SM measurements as a function of Ge concentration after a 30 minute anneal at 800 °C.

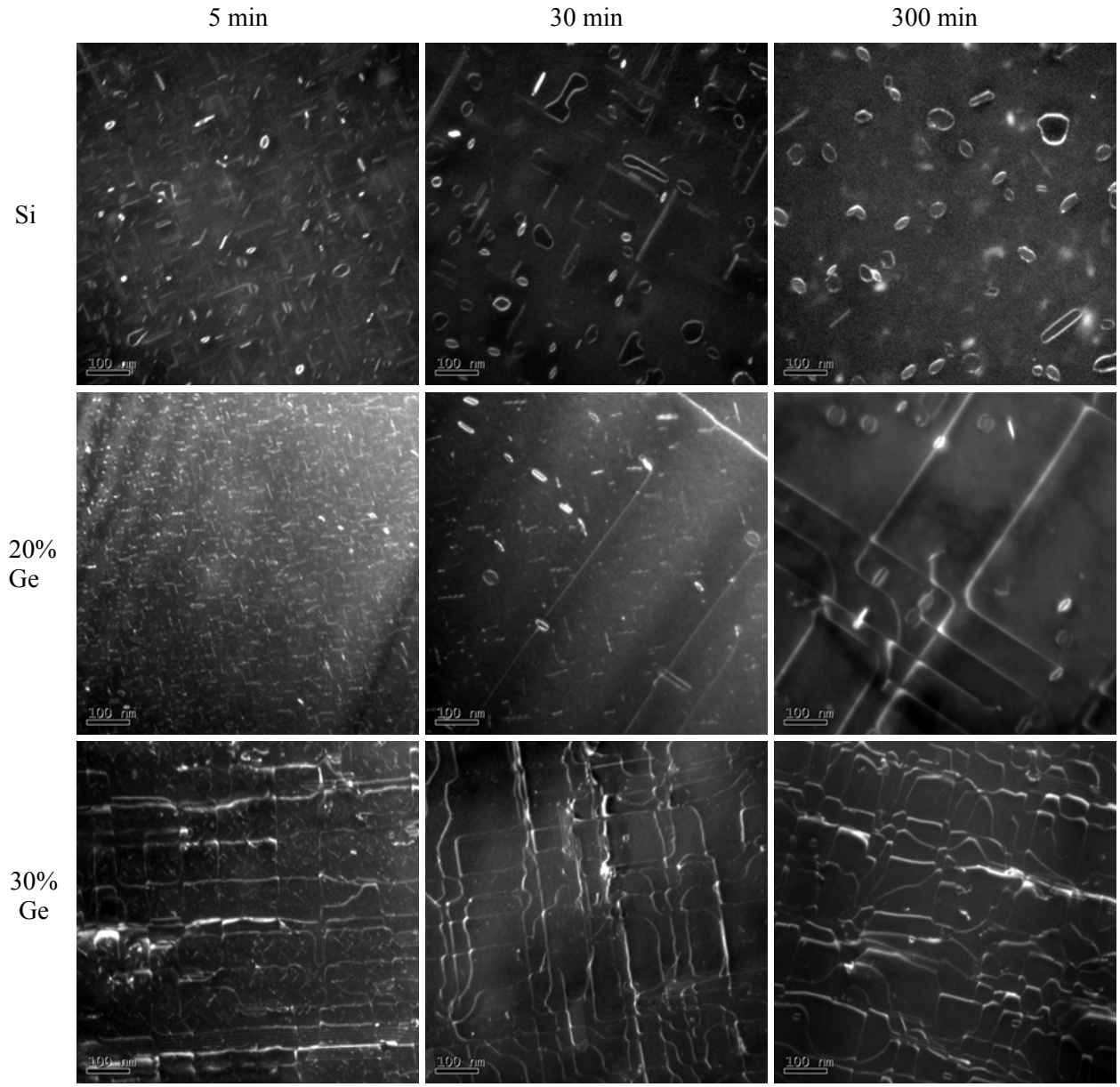

Figure 3-10. PTEM images for Si control and strained Si on relaxed $Si_{1-x}Ge_x$ samples implanted with 12 keV Si^+ and annealed for 5, 30, and 300 minutes at 800 °C.

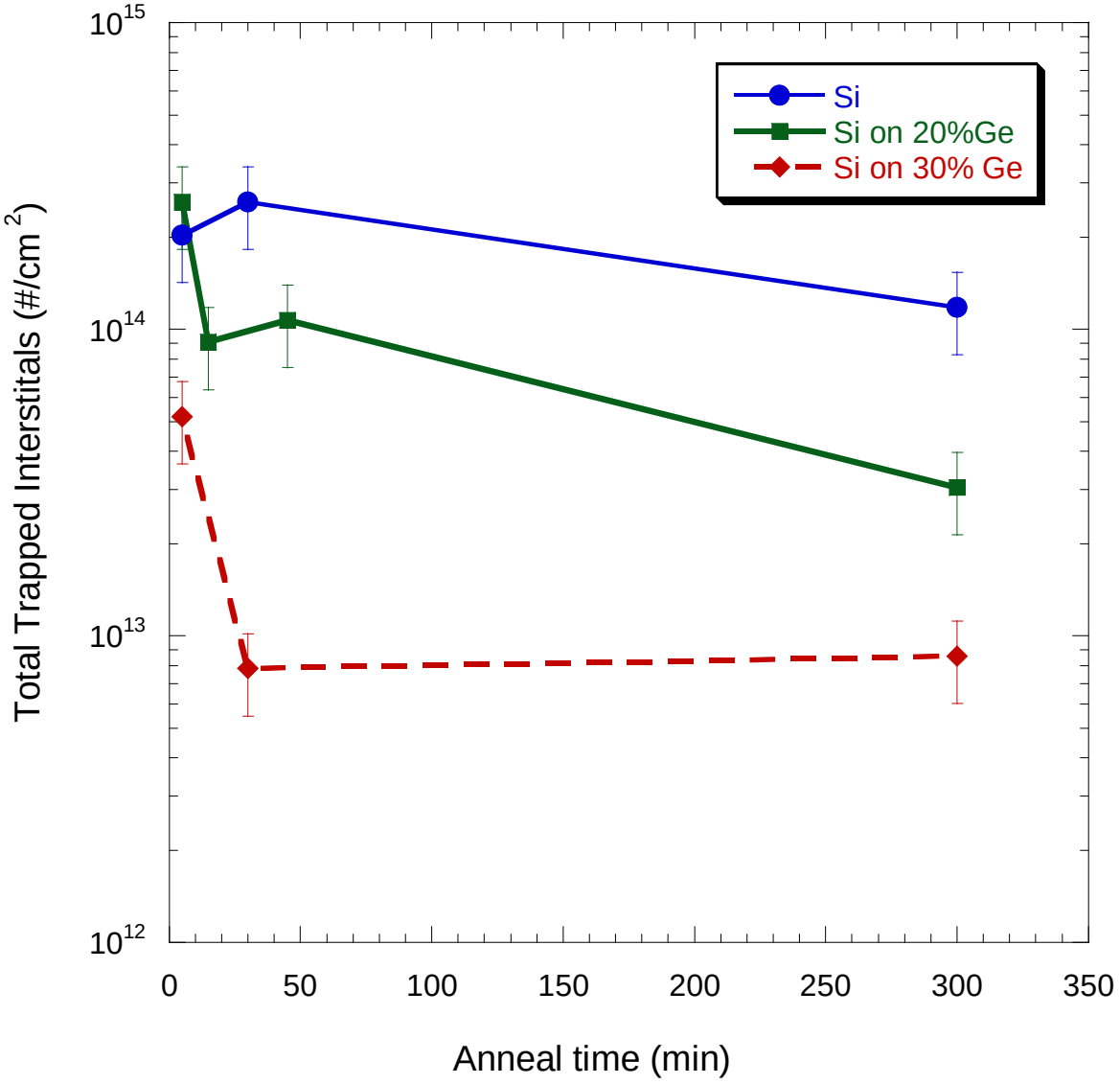

Figure 3-11. Trapped interstitial concentration as a function of anneal time for Si, Si on $Si_{0.8}Ge_{0.2}$, and Si on $Si_{0.7}Ge_{0.3}$ implanted with 12 keV Si^+ and annealed at 800 ºC.

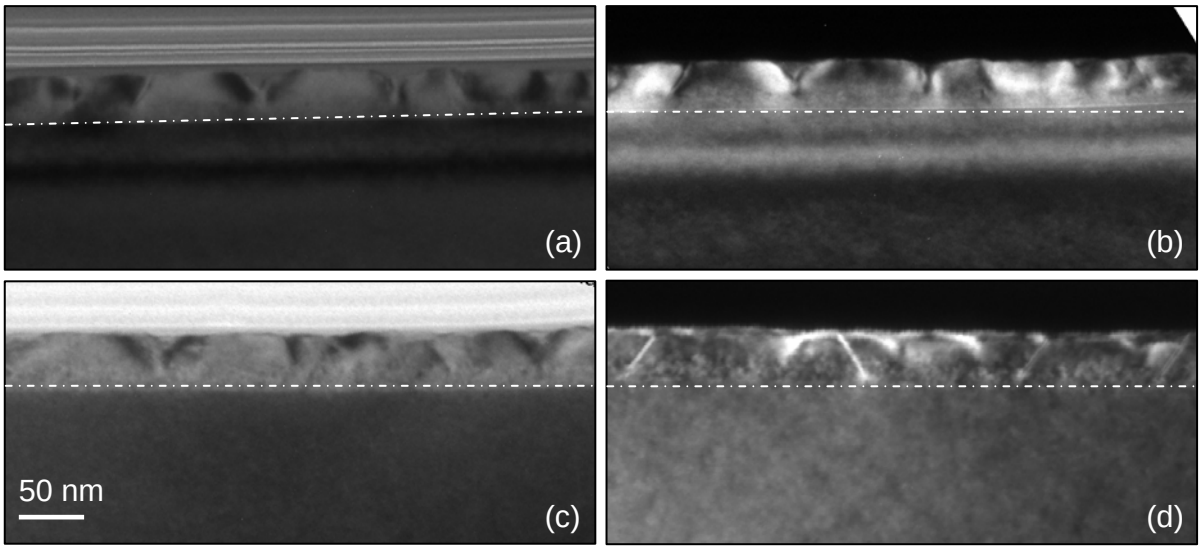

Figure 3-12. XTEM of strained silicon layer of the $Si_{0.7}Ge_{0.3}$ implanted with 12keV Si+ and annealed at (a) and (b) 500 ºC for 30 minutes and for (c) and (d) 45 minutes. XTEM are imaged using (a) and (c) bright-field and in (b) and (d) dark-field mode.

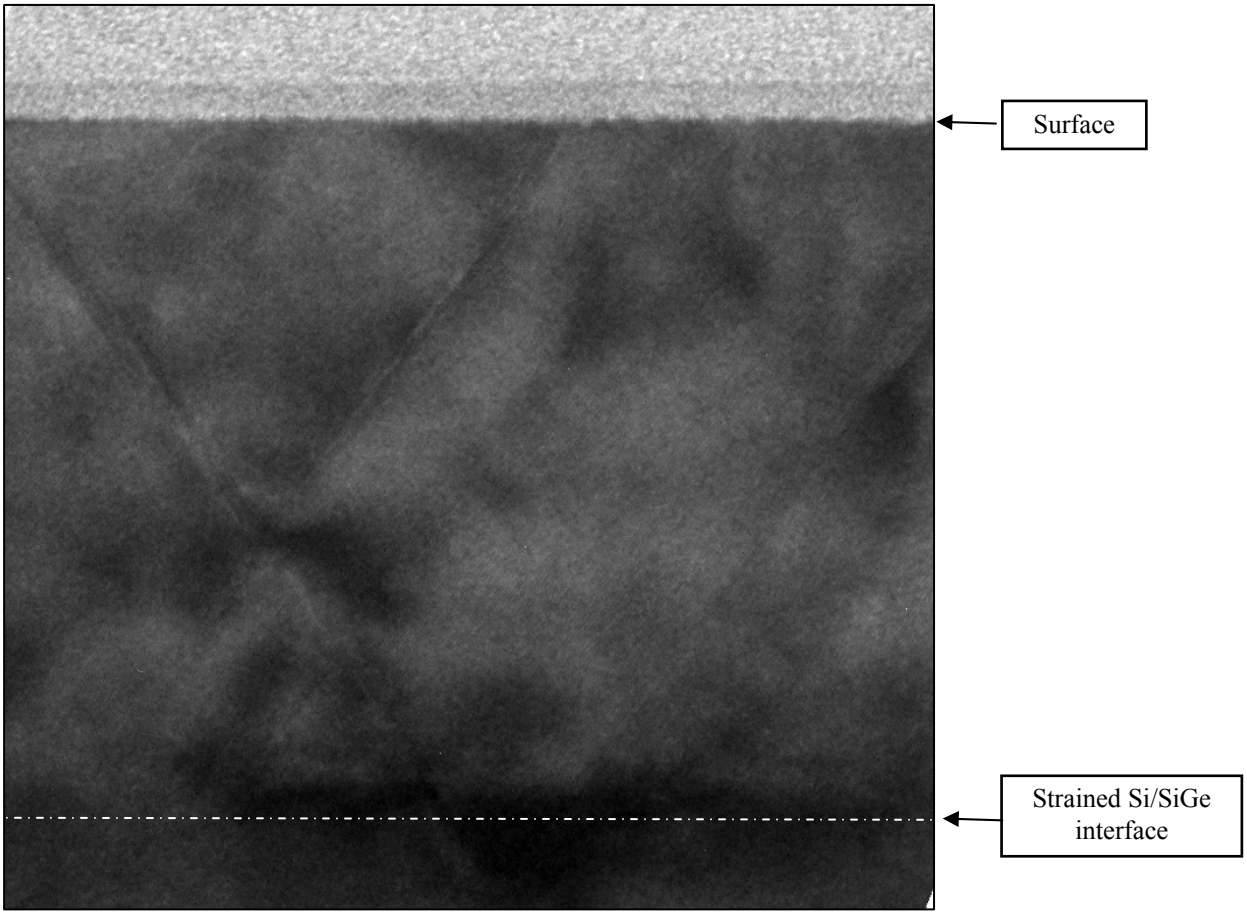

Figure 3-13a. XTEM of stacking faults observed in the strained silicon layer of the $Si_{0.7}Ge_{0.3}$ sample implanted with 12 keV Si^+ and annealed at 800 °C for 30 minutes.

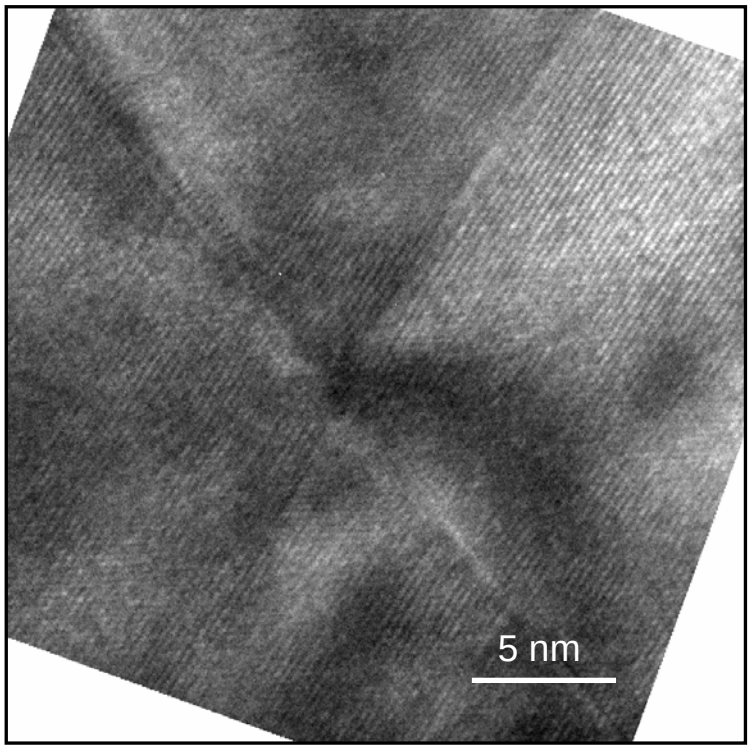

Figure 3-13b. High-Resolution XTEM of stacking faults observed in the strained silicon layer of the $Si_{0.7}Ge_{0.3}$ sample implanted with 12 keV Si^+ and annealed at 800 °C for 30 minutes.

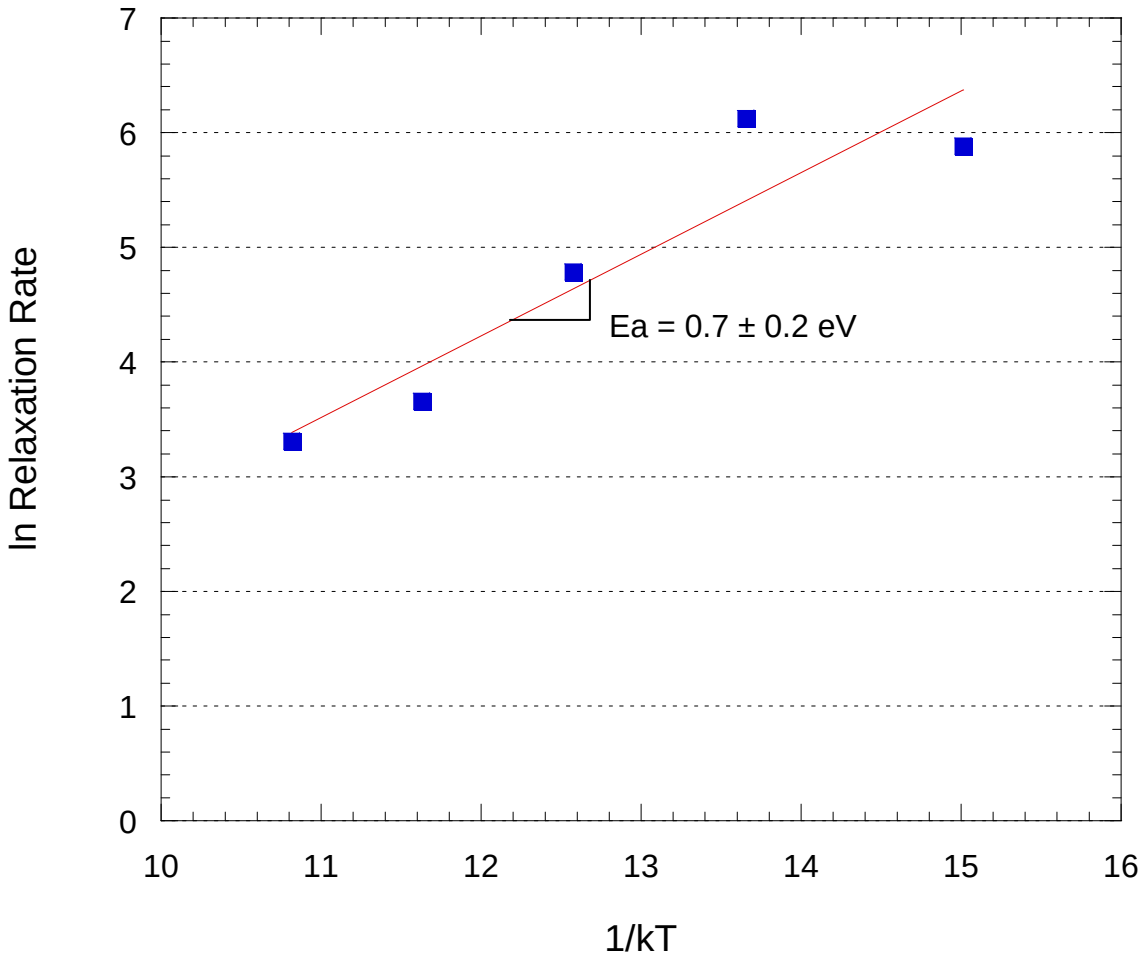

Figure 3-14. Plot of ln relaxation rate vs. 1/kT for 12keV Si^+ implanted strained silicon on relaxed $Si_{0.7}Ge_{0.3}$ sample. Linear regression of data is shown in red.

CHAPTER 4
TENSILE STRAIN: PROXIMITY EFFECT

With the introduction of strain technology in CMOS devices, the effects of strain on the individual fabrication processes have been increasingly important to determine. The work in this chapter investigates the use of amorphizing implants in tensile strained Si regions. Specifically, to investigate whether the proximity of the a-c interface and Si/SiGe interfaces affect strain relaxation.

Epitaxially strained silicon layers were grown on virtual SiGe substrates and were used as test vehicles to study the effect of strain on SPER. Since epitaxial layers were used to study this effect, it is also important to design a study explore the effect of the Si/SiGe interface on the relaxation process as the strain is elastically accommodated by the lattice mismatch at the heterostructure interface. Results in the previous chapter showed that the EOR evolution seemed to be altered in the presence of tensile strain when compared to Si control; the evolved dislocation loops in the strained structures were smaller in size and number. This indicated that, in conjunction with a certain level of strain, excess interstitials were providing a source for the generation of extrinsic stacking faults which then nucleated misfit dislocations. The additional misfit dislocations then promoted further relaxation than annealing alone. The possibility of excess interstitials acting as a source for misfit dislocation nucleation will be further explored in this chapter by varying the implant energy thereby, varying the implant damage proximity to the Si/SiGe interface.

Experimental Design

Strained Si structures were grown on relaxed $Si_{1-x}Ge_x$ (Ge fractions of 0, 10, 20, and 30) virtual substrates via Molecular Beam Epitaxy (MBE) at the University of Aarhus, Denmark. 100mm 0.005-0.020 ohm-cm (100) n-type Czochralski-grown silicon wafers were used for

substrate wafers. Virtual substrates with low threading dislocation densities were grown with compositionally graded buffer layers which incorporated Ge at a rate of 10 at.% per micrometer at temperatures of 750 °C to 800 °C [Fit91]. A 630 nm thick fully relaxed $Si_{1-x}Ge_x$ layer of corresponding composition was then grown on top of the buffer layer, followed by a 50 nm strained silicon capping layer. The strain of the structures was experimentally determined using the in-plane lattice parameters, $a_{Si\text{-}cap}$ and a_{SiGe}, obtained from HRXRD and the relationship in Equation 4-1.

$$\% \text{ Strain Relaxation} = (a_{Si\text{-}cap} - a_{SiGe}) / a_{Si} - a_{SiGe} \times 100\% \qquad (4\text{-}1)$$

The silicon results from this analysis show that the capping layers grown on $Si_{1-x}Ge_x$ with Ge fractions of 0, 10, 20 and 30 correspond to a Si layer strain of 0, 0.37, 0.74, and 1.1% strain, respectively. XTEM analysis was also used in order to verify proper growth of strained films. The structures were then ion-implanted with 5, 12, and 18 keV Si^+ ions at a fluence of 1×10^{15} atoms/cm^2, generating an amorphous layer ~15, 30, 40 nm thick, with varying proximity to the epitaxial interface while confining them within the strained layer. An isothermal study at 800°C for 5, 30, and 300 minutes was then carried out.

This experiment studied the effect of implantation damage proximity to the epitaxial interface on strain relaxation for the highest strain case only. Ion implantation is a non-conservative process which introduces excess point defects into the material. At temperatures between 600 and 800 °C, excess point defects recombine and the remaining excess interstitials agglomerate to form 311 defects. On further annealing, the 311 defects dissolve and contribute to the formation and coarsening of dislocation loops. These defects at all stages are termed End-Of-Range (EOR) damage [Bon98, Cri00, Lam99, Nod00, Uem99]. Since it is likely that strain relieving misfit dislocations may be nucleated at or near the EOR damage created by ion

implantation, the proximity of the EOR damage to the Si/SiGe interface may influence the number and type of defects formed and hence affect the degree of strain relaxation. Thus, this experiment varied both strain and implant energy in order to investigate the effect of the proximity of the EOR to the epitaxial interface on strain relaxation as a function of initial strain. Once annealed, the strain state and crystalline quality was characterized.

A Pananalytical MRD X'Pert was used to obtain HRXRD rocking curves and reciprocal space maps to determine the degree of strain relaxation for each sample. Previous studies have also employed rocking curves to study the strain relaxation observed in the strained silicon capping layer using pseudomorphic Si/ $Si_{1-x}Ge_x$ structures [Cro04, Phe05]. However, further investigation has determined space maps to be a preferable technique for the measurement of annealed samples. Reciprocal Space Maps (RSM)s are compilations of rocking curves taken at a range of ω positions to create a 2D map of intensity in the vicinity of the Bragg reflection. The RSMs allows the observation of very low intensity peaks from the strained silicon layer that rocking curves do not clearly obtain. Using these maps, the relaxation of the layer can be directly observed by monitoring the shift of the strained silicon peak toward the silicon substrate. Additionally, the crystalline integrity of the layer can also be monitored by observing any broadening of the peak that would indicate a disordered or defected layer [Pie04]. Therefore, space maps are preferred for multilayered structures because the lattice parameters can be obtained from peak position and the degree of relaxation obtained directly.

A JEOL 2010F high-resolution transmission electron microscope (HRTEM) and a JEOL 200CX TEM were used to study cross-sections of the regrown layer (XTEM). Samples were prepared using a Dual-Beam FEI Strata DB 235 Focused Ion Beam. XTEM measurements were used to confirm the amorphous layer depth and layer thicknesses. Plan-view (PTEM) samples

were also prepared and imaged using a JEOL 200CX operating at 200kV using g_{220} weak-beam dark-field (WBDF) imaging to quantify dislocation density.

Results

As-Implanted Sample Analysis

Analysis of the as-grown samples can be found in the previous chapter. The experiment presented in this chapter varied the implant energy in order to change the proximity of the a-c interface to the epitaxial interface. All implants were tailored to be strictly confined within the strained layer. Previous work suggests that the amorphization threshold decreases with increasing Ge concentration due to a decrease in binding energy [Hay92, Lie93, O'Ra96]. However, since all implants were conducted within the Si capping layer and not through to the SiGe layer, the amorphous depths were constant as a function of Ge fraction. XTEM of as-implanted Si on SiGe and Si control samples confirmed that amorphous depth did not vary with %Ge for this implant condition. The amorphous depths were within ± 1 nm for all samples within the error of XTEM measurement.

Proximity Effect Experiment

The effect of implant proximity to the defect density and degree of strain relaxation will be discussed for the highest strain case only. The PTEM micrographs, taken at g_{220} BF and WBDF, of the samples post implant and anneal at 800 ºC for 30 minutes is presented in Figure 4-1. The micrograph in (a) is a BF image after anneal alone, (b) is after 5keV implant and anneal, (c) is after 12keV implant and anneal, and (d) is after 18 keV Si^+ implant and anneal. In comparing these results, notice the misfit dislocation spacing after each anneal and implant condition. The anneal only and the 5 keV implant and anneal samples both have similar low densities and the largest average misfit spacing, i.e. lowest degree of relaxation. Once the samples are implanted with higher energies (closer proximity) and annealed, the average misfit spacing decreases

indicating a higher degree of strain relaxation is observed. The misfit dislocation density was quantified in terms of linear density as outlined in the procedure in Chapter Two.

The quantitative HRXRD and PTEM for samples annealed at 800 ºC for 30 minutes is presented in Figure 4-2 as a function of implant energy. The zero implant energy indicates data for the anneal only case. The HRXRD results show a similar trend to that seen in the quantitative PTEM results, indicating that the defect density is related to the degree of relaxation. The defect density of the anneal only and the 5 keV samples are similar in quantity and misfit spacing. Thus, if relaxation is contributed by formation of misfit dislocations, these two samples should exhibit the same degree of relaxation via XRD measurements. However, this is not the case. The as-grown plus anneal sample exhibited a 1% relaxation whereas the 5 keV samples exhibited a ~17% relaxation. In addition to misfit dislocations, the 5 keV samples also exhibited presence of stacking faults in the PTEM micrographs. Since both of these samples exhibited similar misfit dislocation densities, yet the 5 keV sample observed a higher degree of relaxation, suggests that the presence of stacking faults also contribute to a large percentage of the relaxation. The two higher implant energies, 12 and 18 keV, exhibit a greater density of misfit dislocations in conjunction with higher degree of relaxation. From these results, it is evident that with increasing proximity to the interface, a higher degree of strain relaxation is observed which is confirmed with the higher density of misfit dislocations.

Further investigation of the PTEM for the three different implant conditions in terms of anneal time allows better understanding of the dependence of strain relaxation on proximity. Figure 4-3 presents PTEM micrographs, taken under g_{220} WBDF conditions, for the highest strain case implanted with 5, 12, and 18 keV Si^+ and annealed for various times at 800 ºC. All micrographs were taken at the same magnification. Comparing samples annealed at the same

time, the misfit densities increase with increasing proximity (implant energy). This effect is also evident at longer anneal times. This trend of increasing misfit density with increasing proximity is more clearly depicted in the quantitative analysis of PTEM presented in Figure 4-4. Furthermore, the misfit density is observed to increase up to a saturation point at which it levels off. At this point, the strained layer is completely relaxed and there is no driving force for dislocations generation.

The higher the implant energy the closer the excess interstitials are placed with respect to the Si/SiGe interface. Assuming that the net excess interstitials are constant at these energies [Gut01b], the only variable to be considered is proximity of the excess interstitials to the interface. These results indicate that the placement of the a-c interface closer to the epitaxial Si/SiGe interface is highly influential on the degree of relaxation and density of misfit dislocations generated. These observations indicate that the Si/SiGe interface may acting as a sink for the excess interstitials and promote further relaxation as a result.

Discussion

The results discussed in the previous chapter suggested that strained silicon can be amorphized and regrown without strain relaxation for all $Si_{1-x}Ge_x$ compositions up to $Si_{0.8}Ge_{0.2}$ for anneals up to 800 ºC for 30 minutes. For the strained Si sample on $Si_{0.7}Ge_{0.3}$, the solid phase regrowth of the amorphous layer breaks down and results in the formation of regrowth related defects within the amorphous region which extended back down to the strained Si/ $Si_{1-x}Ge_x$ interface. Furthermore, the EOR evolution and population seemed to be altered in the presence of tensile strain when compared to the Si control; the evolved dislocation loops in the strained structures are smaller both in size and quantity. This indicates that, in conjunction with a certain level of strain, excess interstitials, a result of the implant, are providing a source for the generation of extrinsic stacking faults which then nucleate misfit dislocations. The possibility of

ion implantation produced excess interstitials acting as a source for misfit dislocation nucleation was further explored by varying proximity of the implant damage to the epitaxial interface while still confining it within the strained layer.

In developing this experiment, one must consider all variable parameters. A change in implant energy with constant fluence and species will change the a-c interface depth. Additionally, the net interstitial profile will also change. However, with the energy range used in this experiment previous work by Gutierrez et al. [Gut01b] suggests that the net interstitial population is constant. Therefore, the net excess interstitial population of the implants in this experiment is assumed to be constant. Therefore, placing the implant closer to the interface places the net excess interstitials closer to the interface while the net interstitial population is held constant. This experiment was specifically designed to determine if the interface acts as a sink for point defects.

Results in this chapter have shown that proximity of the implant damage to the heterostructure interface influences both misfit dislocation density and degree of strain relaxation. The closer the damage proximity to the heterostructure interface the higher degree of relaxation combined with a higher misfit dislocation density is observed. Thus, it is plausible that the interface may be acting as a sink for the excess interstitials which then drives further relaxation when the damage is placed closer to the heterostructure interface. Additionally, the results in the previous chapter showed that the end-of-range damage population decreased in conjunction with an increase in misfit dislocations. Therefore, it is plausible that the proximity of the damage to the interface influences both trapped interstitial concentration as well as the degree of relaxation. However, future studies below 800 ºC are recommended to explore the

end-of-range evolution and trapped interstitial concentration as a function of damage proximity to the interface to fully understand the role of excess interstitials to the relaxation process.

Conclusions

The results in this chapter have shown that the implant damage proximity to the Si/SiGe interface impacts the degree of relaxation and misfit dislocation density. After a constant anneal time and temperature, 800 ºC for 30 minutes, and varying implant energy (proximity) the misfit dislocation spacing is observed to decrease with increasing proximity. Therefore, exhibiting a higher density and observed relaxation as confirmed by HRXRD measurements. Further analysis using isothermal anneals and PTEM showed that the misfit dislocations are observed to increase in density for the two lower implant energy cases. The highest energy case, already observed complete relaxation at 30 minutes and exhibits constant misfit dislocation density with further annealing. The PTEM and HRXRD results are consistent and confirm data observed.

In summary, this experiment has determined that misfit dislocation density and strain relaxation depends significantly on the proximity of the initial a-c interface. The closer proximity of the damage to the Si/SiGe interface, the higher the degree of relaxation and higher misfit dislocation density is observed. Additionally, the results in the previous chapter showed that the end-of-range damage population decreased in conjunction with an increase in misfit dislocations. These results indicate that close proximity of the damage to the interface could influence both trapped interstitial concentration as well as the degree of relaxation. Therefore, from these results it can be inferred that the epilayer interface may be acting as a sink for point defects when the implant damage is placed in close proximity. To confirm this claim, future studies below 800 ºC are recommended to explore the end-of-range evolution and trapped interstitial concentration as a function of damage proximity to the interface to fully understand the role of excess interstitials to the relaxation process.

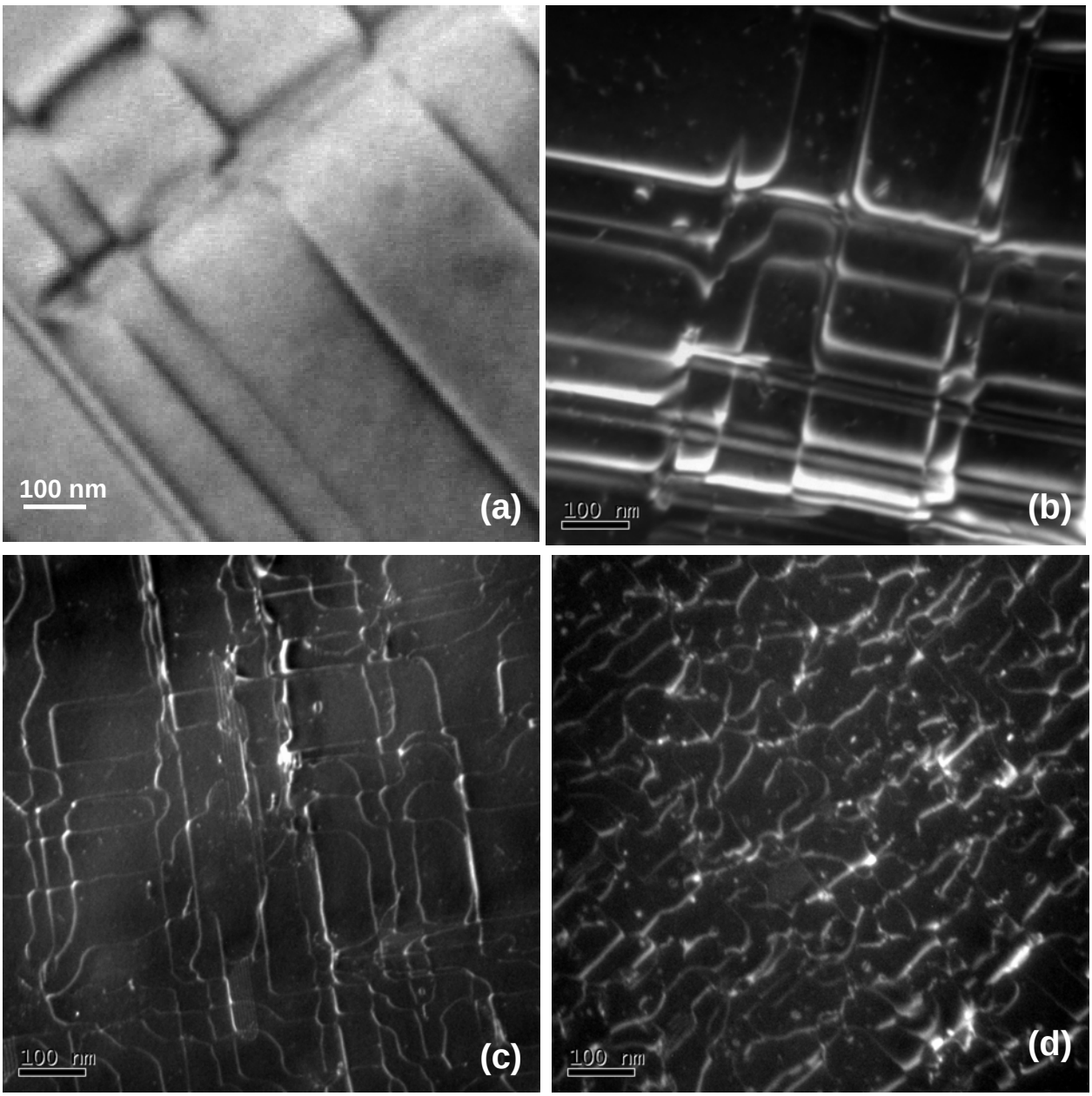

Figure 4-1. PTEM images for (a) Si control sample and Si on $Si_{0.7}Ge_{0.3}$ samples implanted with (b) 5 keV Si^+ (c) 12 keV Si^+ and (d) 18 keV Si^+ and annealed for 30 minutes at 800 ºC.

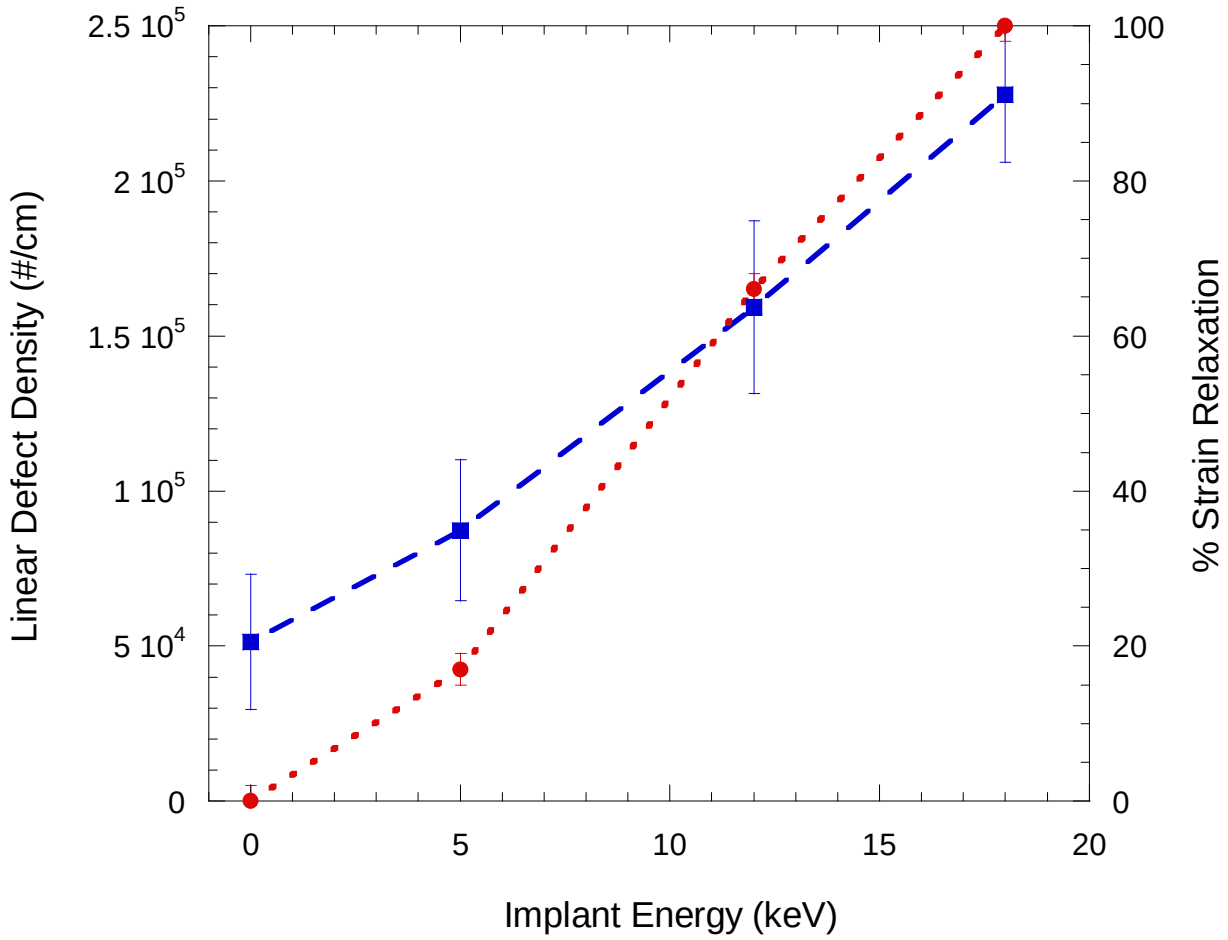

Figure 4-2. Strain relaxation (circles) and linear defect density (squares) as a function of implant energy after 800 ºC 30 minute anneal. Zero implant energy indicates data for as-grown plus anneal case.

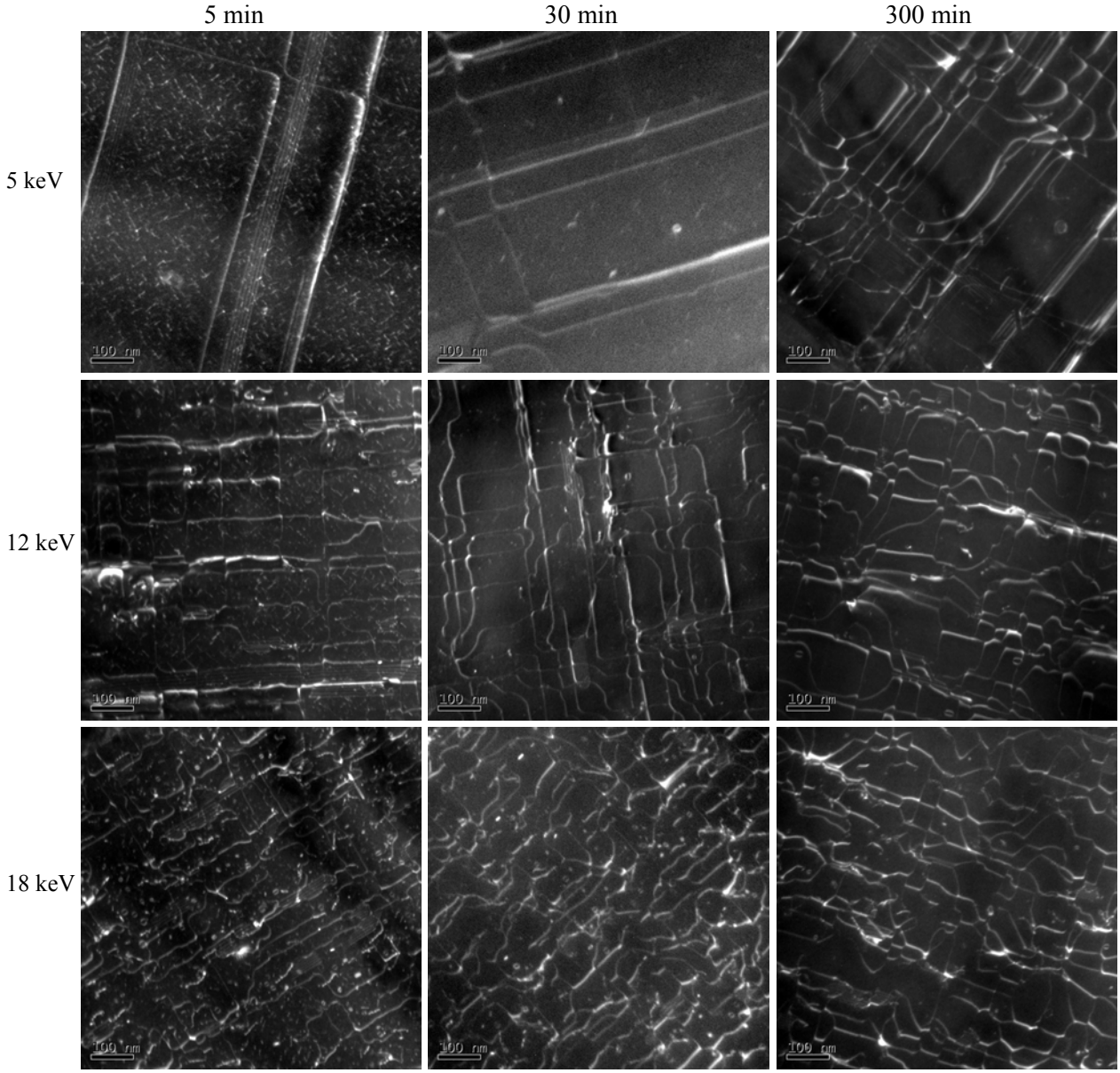

Figure 4-3. PTEM images for strained Si on $Si_{0.7}Ge_{0.3}$ samples implanted with 5, 12, and 18 keV Si^+ and annealed for 5, 30, and 300 minutes at 800 ºC.

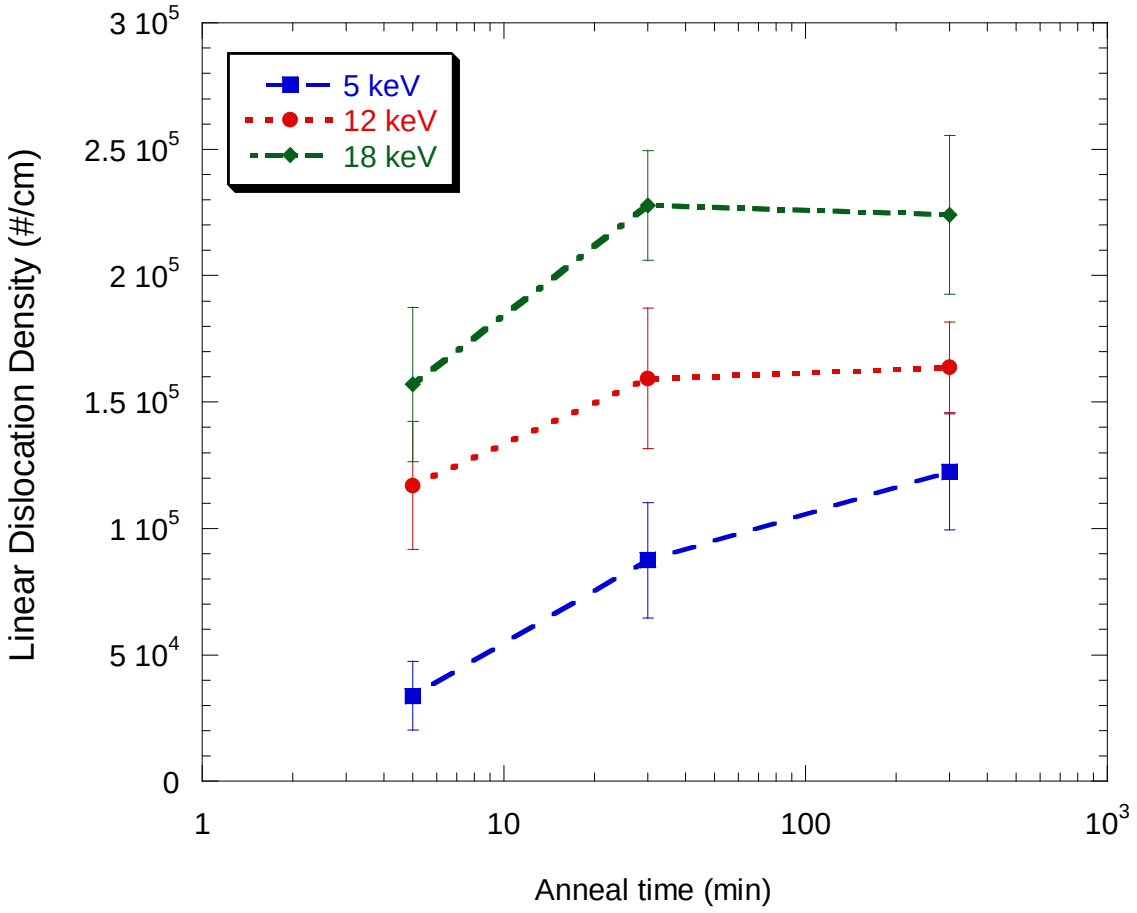

Figure 4-4. Linear dislocation density quantified using PTEM for strained Si on Si0.7Ge0.3 samples implanted with 5, 12, and 18 keV Si+ and annealed for 5, 30, and 300 minutes at 800 ºC.

CHAPTER 5
COMPRESSIVE STRAIN: DEFECT NUCLEATION AND STRAIN RELAXATION

With the introduction of strain technology in CMOS devices the effect of strain on the individual fabrication processes has become increasingly important. Specifically, understanding the upper strain limit for successful regrowth under compression is critical to device processing. This chapter outlines experiments to determine the magnitude of compressive strain that may be used in conjunction with amorphizing implants without inducing strain relaxation.

In these experiments, epitaxially strained silicon germanium layers are grown on silicon substrates as test structures to study the effect of compressive strain on Solid Phase Epitaxial Regrowth (SPER). The first experiment is designed to study the mechanism by which defects nucleate and cause strain relaxation during SPER. The defect nucleation study was performed using lower temperature anneals in order to observe the a-c interface prior to complete growth. The second experiment was designed to investigate the interaction of excess interstitials, a result of the implant, with the relaxation process. This study was performed using an isochronal experiment in which the relaxation and defects microstructure is monitored during the early stages of nucleation and growth and the latter stages of coarsening as seen in Si (if present in SiGe). In summary, by monitoring the quantity of dislocations in strained vs. unstrained samples and studying the kinetics of the dislocation growth process the relationship between the strain relaxation process and SPER can be further clarified.

Experimental Design

The experimental structures were grown using Reduced Pressure Chemical Vapor Deposition (RPCVD). Pseodomorphically strained 50 nm $Si_{1-x}Ge_x$ was deposited on Si (001) substrate with alloy compositions of 0, 16, 22, and 26 % germanium. The as-grown structures were characterized using TEM and XRD techniques in order to ensure proper growth of strained

films. All Post growth, the structures were implanted with Si^+ with an energy of 12 keV at a fluence of $1x10^{15}$ atoms/cm^2 to generate a 30 nm continuous amorphous layer confined within the strained layer. Anneals were performed in a quartz-tube furnace under an inert N_2 ambient environment. The experiments were designed to study specific factors that may affect the relaxation process.

The first experiment consisted of an isothermal study at 500 ºC performed to investigate defect nucleation and propagation in the strained film. Anneal times were 15, 30, and 45 minutes. With these times and temperature, the regrowth velocity is slow enough that the amorphous-crystalline (a-c) interface will be captured before complete regrowth has taken place. This allows observation of defects as they nucleate and grow with the use of XTEM and PTEM. Only the highest and lowest strained samples, implanted with an energy of 12keV, were used for this experiment. Additionally, a preanneal of 400°C for 60 minutes was conducted prior to the 500ºC anneal to relax and planarize the a-c interface before initiation of SPER. Analysis of the preanneal, shown in Appendix B, planarized the a-c interface prior to regrowth. Similar low temperature preanneals, also have been conducted to planarize the a-c interface in prior work [Kin03, Ban00].

The second experiment consisted of a 30 minute isochronal study to investigate the interaction of extended defects and their evolution with the relaxation process. Temperatures of 500, 575, 650, 725 and 800 ºC were used. In implanted Si, the supersaturation of interstitials lead to evolution and agglomeration of extended defects when annealed above 650 °C. If present in strained SiGe, the effect of the evolution of these extended defects will be studied. The highest Ge, 26%, sample implanted with 12keV Si^+ was used in this isochronal study.

A Pananalytical MRD X'Pert was used to obtain XRD Rocking Curves (RC) and Reciprocal Space Maps (RSM) to obtain the degree of relaxation observed post anneal. A JEOL 2010F high-resolution transmission electron microscope (HRTEM) and a JEOL 200CX TEM were used to study cross-sections (XTEM) of the regrown layer. Samples were prepared using a Dual-Beam FEI Strata DB 235 Focused Ion Beam. XTEM measurements were used to confirm the amorphous layer depth and layer thicknesses. Plan-view (PTEM) samples were also prepared and imaged using a JEOL 200CX operating at 200kV using g_{220} weak-beam dark-field imaging to quantify dislocation density.

Results and Discussion

As-Grown Sample Analysis

The XRD (004) RC for the as-grown structures are shown in Figure 5-1. The position of the diffraction peak depends on Ge composition and strain relaxation in the layer. The oscillation near the SiGe Bragg peak is due to different scattering factors along the Qz axis which arise from the difference in atomic species across the boundary layer. The thickness of the SiGe layer can be calculated using the peak-to-peak distance of the oscillations provided that the material is pseudomorphically strained [Bir03]. Therefore, PTEM (not shown) was used to determine if the strained layers were grown pseudomorphically. The 16 and 22% Ge samples showed no misfit dislocation formation and were completely pseudomorphic. The 26% Ge sample, however, was partially pseudomorphic and exhibited a 0.77% relaxation calculated using misfit spacing [Mat74]. XRD RC analysis, however, indicated 0% relaxation for the same sample due to sensitivity limitations of the X-ray technique [Bir03]. The pseudomorphic/non-pseudomorphic conditions of these samples are in good agreement with the observations of People and Bean [Peo85].

All as-grown samples were analyzed using XRD RC, X-Ray Reflectivity (XRR) and TEM cross-section to verify Ge concentrations and layer depth. Simulation of the experimental x-ray spectra from RC and XRR configurations yields Ge concentration, thickness, and roughness measurements of the SiGe layers. XTEM analysis of the samples was also used to directly measure the thickness of the layer. A summary of these results are in Table 5-1. The Ge concentrations were within ± 1 at% of nominal for each wafer. The thickness measurements obtained from the X-Ray simulations and the XTEM results agree well when the strained layers are completely pseudomorphic (16 and 22% Ge). The 26% Ge sample, however, is partially pseudomorphic as determined by PTEM. The discrepancy between the layer thickness measured via X-ray techniques and the XTEM could indicate higher error in X-ray measurement due to scattering from defects at the interface. To accurately model the parameters for partially relaxed layers, the degree of relaxation must be known and measured using an alternate technique.

As-Implanted Sample Analysis

All samples discussed in this chapter were implanted with a 12 keV Si^+ implant at a fluence of $1x10^{15}$ atoms/cm^2. The implants were tailored to generate a continuous amorphous region confined within the strained layer as shown in Figure 5-2. XTEM of as-implanted SiGe and Si samples confirmed that amorphous depth did not vary with %Ge for this implant condition. The amorphous depths were within ±1 nm for all samples this is within the error of XTEM measurement.

Defect Nucleation/Interface Roughness Study

All strain conditions formed defects and observed strain relaxation post SPER. The mechanism of defect introduction and the morphology of the amorphous-crystalline interface were studied using an isothermal study performed at 500 ºC. At this temperature, the regrowth velocity is slow enough such that images of the a-c interface at various stages prior to complete

regrowth can be captured. Samples were annealed for 15, 30, and 45 minutes and XTEM was used to observe the progression of SPER.

Figure 5-3 shows XTEM images, taken under on-axis bright field conditions, of the advancing a-c front transitions from a planar interface (as-implanted) to one that is rough as SPER progresses. The roughening process is also dependent on the degree of strain; a higher peak to valley amplitude is observed with increasing magnitude of initial strain. This roughening effect has been previously observed in compressively strained Si films [Bar04] and in metastable strained SiGe films [Ang07, Cor96] during SPER and in high dose Ge^+ implants into Si to form SiGe [Cri96, Eli96]. A defect-free regrown layer and a planar advancing a-c interface, however, has been shown in relaxed SiGe films with up to a 38% Ge concentration [Kri95a]. Additionally, Antonell et al. [Ant96] showed that incorporating C into SiGe prior to amorphization delayed the onset of dislocation formation and promoted planar a-c interface growth due to strain compensation effects. These results indicate that the roughening of the advancing a-c front is a strain effect and not a Ge chemical effect.

As the a-c front advances towards the surface under compressive strain, an increase in roughness is observed due to competing elastic and strain energies, similar to the perturbation observed in epitaxial growth via MBE or CVD. Balancing these energies yield a minimum wavelength of the perturbation as determined by previous research [Sro89]. It is also well known that SPER velocity is dependent on growth direction. The [110] and [111] growth velocities are 3 times and 25 times slower, respectively, than [001] as determined by Csepregi [Cse78]. Thus, once the a-c interface has roughened significantly, the slower growing [110] and [111] fronts retard the overall regrowth velocity as the initial magnitude of strain is increased. This effect can be observed by comparing Figure 5-3 (a) for 16% Ge and (b) for 26% Ge.

Additionally, it is can be firmly concluded that roughness is enhanced at higher strain magnitudes.

The roughening, in turn, causes defect formation as the misoriented facets meet and nucleate defects during SPER. PTEM analysis, using g_{220} WBDF conditions, shown in Figure 5-4, was used in order to determine the Burger's vector of the defect. The dislocations are perfect dislocations of a/2<110> type which have been reported in prior works [Cri96, San84] and are termed "hairpin" dislocations. The mechanism of the nucleation and growth of these defects have been postulated by T. Sands [San84]. Typically, these dislocations were so great in number that it does not allow imaging of underlying misfit dislocations (cross-hatch pattern), a result of strain relaxation, located at the epitaxial interface. Of the large quantity of PTEM samples analyzed, one sample happened to etch down to the interface and revealed the presence of misfit dislocations. The PTEM image of this sample is shown in Figure 5-5. By examining this image, it can be observed that the hairpin defects are much greater in number and closer in spacing than the misfit dislocations. Thus, it is important to note that the hairpin defects may obstruct the imaging and quantification of misfit dislocations.

In summary, this experiment showed that the a-c interface roughens due to strain and that the roughness increases as the magnitude of strain is increased. Also, defects are nucleated during SPER through the meeting of growth fronts of different orientations. These defects were determined to be hairpin dislocations and are so vast in number that they can obstruct imaging of misfit dislocations.

Temperature Dependence Study

The relaxation behavior of 26% Ge, 12keV samples was studied using a series of 30 minute isochronal anneals performed at 500, 575, 650, 725 and 800 ºC. This experiment was designed to study the evolution and agglomeration of supersaturated interstitials and their

interaction with the relaxation process. Crosby et al. [Cro05] studied the evolution of these extended defects as a function of Ge in relaxed SiGe alloys. The samples studied were implanted with Si^+ below the amorphization threshold. In low Ge concentration samples, the dissolutions rates were similar to that of Si. At intermediate concentrations, 25% and 35% Ge, the dislocation loops appear relatively stable. Above 50% Ge, the dislocation loops become unstable. This study aims to determine if the dislocation loops are stable in strained SiGe films and how they influence relaxation. XRD RCs were obtained to determine strain relaxation post implantation and anneal. Additionally, PTEM and XTEM were used to study the defect microstructure and depth.

PTEM quantification was used to obtain dislocation density. All samples displayed an extended dislocation network in the form of a large connected array rather than individual dislocations. A linear (rather than area) quantity was therefore measured for more accurate quantification. Figure 5-6 shows a series of PTEM images as a function of anneal temperature. The spacing of the hairpin dislocations, and thus the linear dislocation density quantified in Figure 5-7, do not depend on the anneal temperature. Additionally, the sample in Figure 5-6(a) shows hairpin dislocation present when regrowth has not been completed. This sample was partially regrown yet hairpins are observed. These results suggest that the defects nucleate as the SPER process progresses and remain stable at higher temperatures. Additionally, unlike the results from Crosby et al. [Cro05], no extended defects were observed in any samples of this study. This suggests that the roughness of the a-c interface, not point defects, is a dominant factor in defect formation in strained SiGe alloys.

The hairpin dislocations are nucleated when the misoriented facets of the rough a-c interface meet and propagate as the a-c interface propagates towards the surface. It is also

observed, using XTEM, (not shown) that these defects do not glide down to the epitaxial interface. The defective layer is contained between the depth of defect nucleation and the surface for lower strain cases and extends to the entire layer in the highest strain case. This will be further discussed in the next chapter.

XRD RC for the isochronal study is shown in Figure 5-8. The SiGe peak is observed to broaden and the interference fringes are absent after higher temperature anneals. This is an indication of larger variation of SiGe lattice parameter and a disturbance of the epitaxial interface. Thus, the film is undergoing strain relaxation. Further investigations of the highest temperature anneal, 800 °C for 30 minutes, using RSM shows that the strain state of the SiGe film is gradient in nature. The RSM spectrum, in Figure 5-9, shows that the SiGe peak is broadened and extends from full relaxed to fully strained state. Also, the elongation of the peak shape in the direction of the relaxation line (refer to Figure 2-5 for clarification) indicates the layer is mosaic in nature. For all samples exhibiting this gradient, the highest intensity peak was used to quantify strain relaxation. When this average strain relaxation plotted in Figure 5-10 is compared to the defect density shown in Figure 5-7, the results do not similar trends. This discrepancy between the XRD and TEM data is discussed further in the next chapter.

This can be further understood by considering two mechanisms of relaxation. The first is that the relaxation occurring at the Si/SiGe interface is due to the lattice mismatch not being accommodated elastically and nucleating misfit dislocations [Mat74, Peo85]. Second, the relaxation observed in the SiGe layer is due to the defects nucleated via roughening of the a-c interface during regrowth and when the facets of the interface meet observed in this work and others [Ang07, Hon92, Lee93]. XRD measures the first type of relaxation and the second is observed using XTEM and PTEM. This fact causes some discrepancy in comparing the XRD

and TEM results for these samples. More specifically, this discrepancy is due to the localized defect-free region and highly defective region, causing a strain gradient.

This experiment has shown the defect nucleation is dominated by the a-c roughness. The experiment has also shown that hairpin dislocation density is stable and not a function of temperature. It does not correlate, therefore, with the strain relaxation observed via XRD which increases as anneal temperature is raised.

Conclusion

The results in this chapter have shown four main points. First, the a-c interface roughens due to compressive strain and this roughness increases when the magnitude of strain is increased. The roughness is a strain effect previously reported in both compressively strained Si [Bar04] and in metastable SiGe films [Ang07, Lee93]. It is also similar to the effect seen in compressively strained epitaxial layers grown via deposition techniques [Sro89]. With increasing initial strain in the film, there is a more strain energy to compensate by decreasing elastic energy. The balance of these energies yields a minimum wavelength of the roughness for the a-c interface.

Second, defects are nucleated during SPER by the competition of the different direction growth fronts. Using $g \cdot b$ analysis, these defects were determined to be hairpin dislocations with Burgers vector of a/2 <110> which were first observed by T. Sands [San84]. These defects were later observed in metastable SiGe SPER [Ang07] and in Si samples implanted with high dose Ge^+ to form SiGe via SPER [Cri96]. The a-c interface in these other structures also exhibited roughness similar to these observations.

Third, in relation to the tensile case discussed in previous chapters, the critical strain for SPER breakdown is much lower in compression. The a-c interface roughness in compressions is the main cause for both defect nucleation and a lower critical strain in compression versus

tension. The rough a-c interface allows defect nucleation at much lower compressive strain than defect nucleation by yielding in tension. This is also the main cause for the difference in defect type observed. The regrowth related defects observed in compression were a/2<110> type dislocation network, while the defects in tension were stacking faults. The roughening a-c interface in SiGe films does not allow the film to reach its yield point. Instead, defects are introduced which relax the strain and a driving force towards further dislocation nucleation no longer exists.

Fourth, the experiment has also shown that hairpin dislocation density is stable and not a function of temperature over the range studied. It does not correlate, therefore, with the strain relaxation observed via XRD which increases as the anneal temperature is raised. The defects nucleate at the meeting of the facets of the rough a-c interface and propagate towards the surface with the advancing front. It is also observed that these defects do not glide down to the epitaxial interface. The defective layer is contained between the depth at which defect nucleation occurred and the surface. At lower strain, there lies a defect-free layer which retained its initial strain with a highly defective layer near the surface which is fully relaxed. The experiment in the next chapter will discuss how this defect-free layer is influenced by both initial magnitude of strain and the proximity of the a-c interface to the epitaxial interface.

Sample Conditions		XRR				RC		XTEM
Thickness	%Ge	X^2	Thickness (nm)	Roughness (A)	Density (g/cc)	Thickness (nm)	% Ge	Thickness (nm)
50	16	1.60E-02	49.3	7	2.91	49.9	15.6	50.0
50	22	1.58E-02	48.4	10	3.08	47.0	21.6	47.0
50	26	4.20E-02	57.7	9	3.21	58.0	26.0	51.0

Table 5-1. Summary of XRR and RC spectra simulations compared to XTEM measurements.

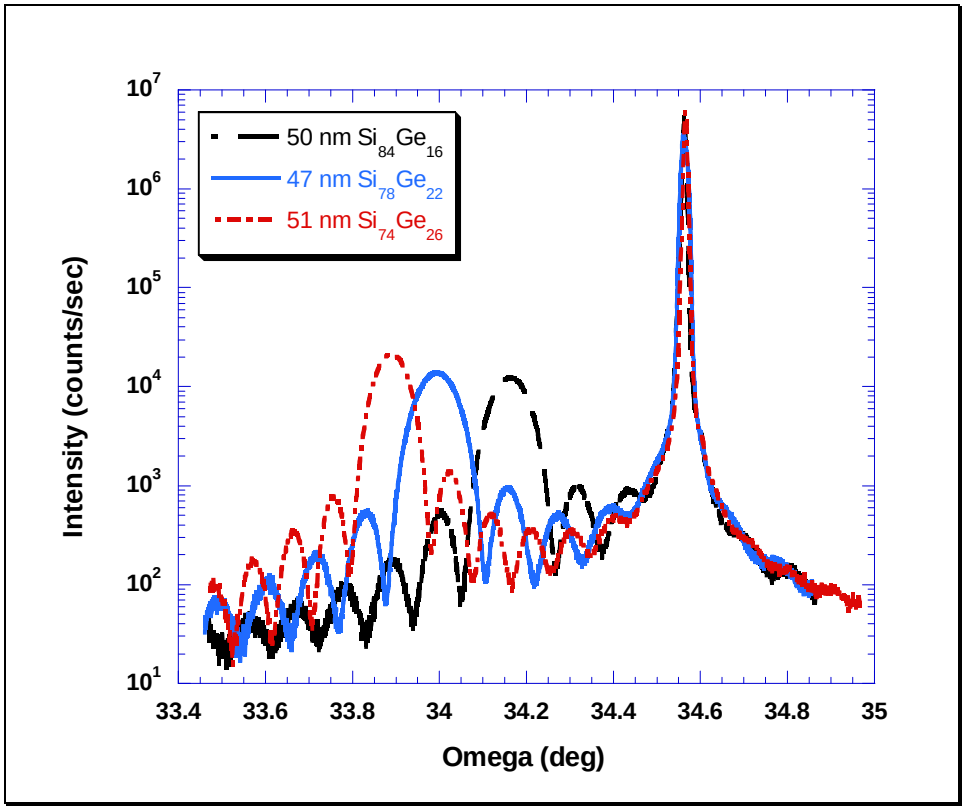

Figure 5-1. XRD (004) rocking curves for all as-grown strained SiGe on Si samples.

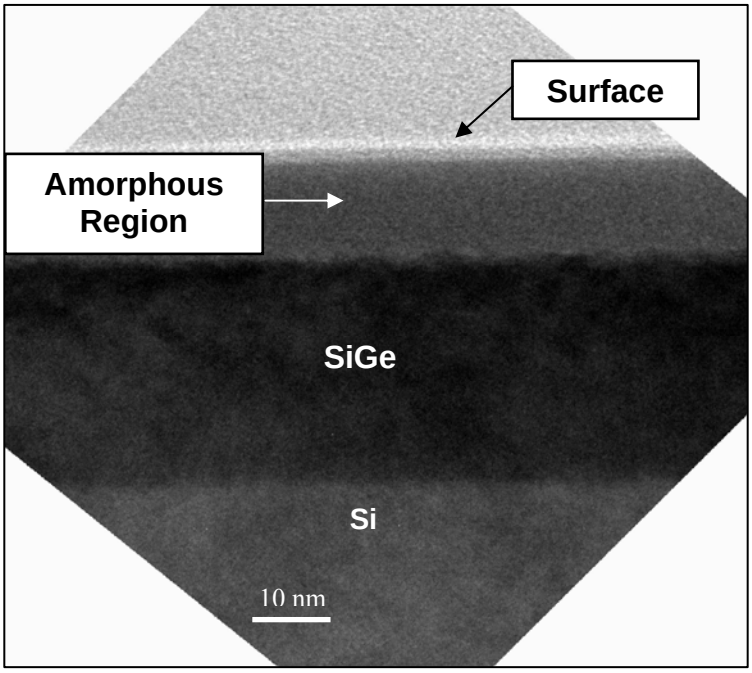

Figure 5-2. Cross-section of as-implanted strained SiGe on Si samples.

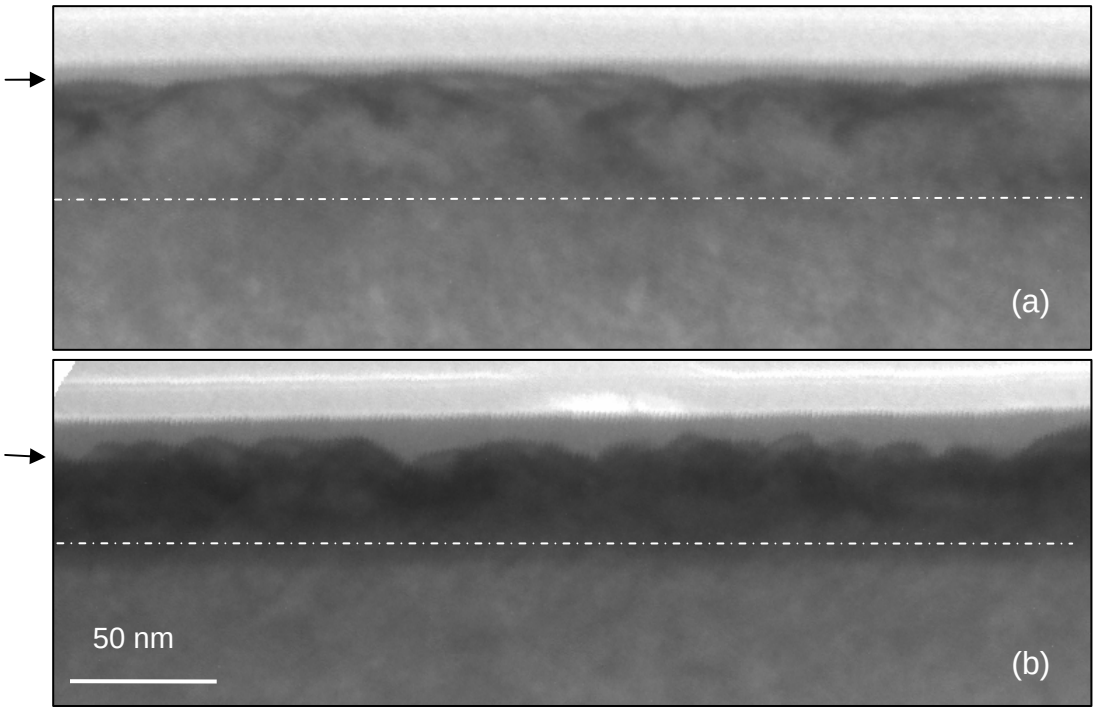

Figure 5-3. XTEM of strained $Si_{1-x}Ge_x$ on Si samples implanted with 12keV Si^+ annealed at 500 ºC for 45 minutes (a) x= 16 (b) x= 26. Arrows indicate a-c interface and hatched white lines indicate epitaxial interface.

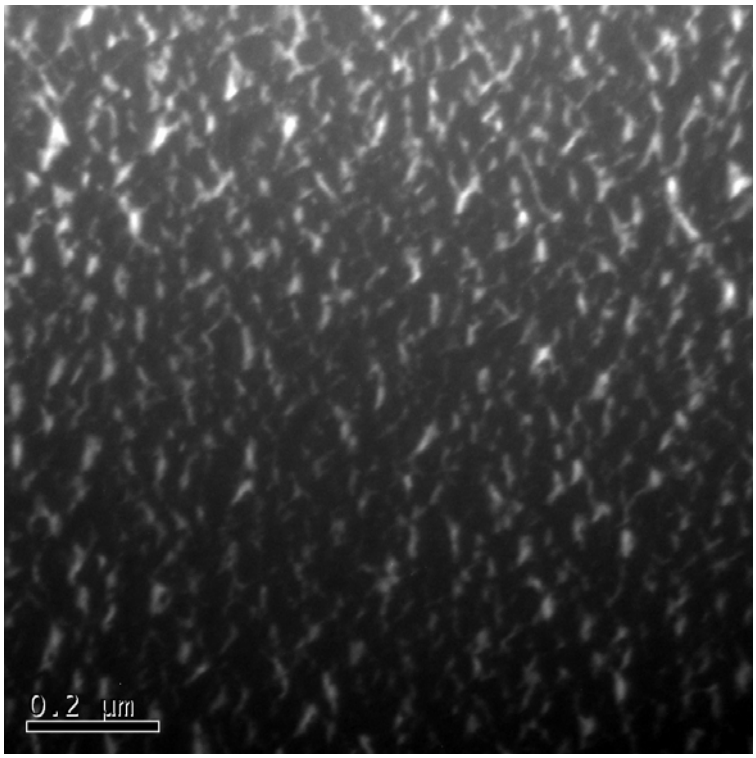

Figure 5-4. PTEM image of strained $Si_{0.74}Ge_{0.26}$ on Si samples implanted with 12 keV Si^+ and annealed for 45 minutes at 500 ºC.

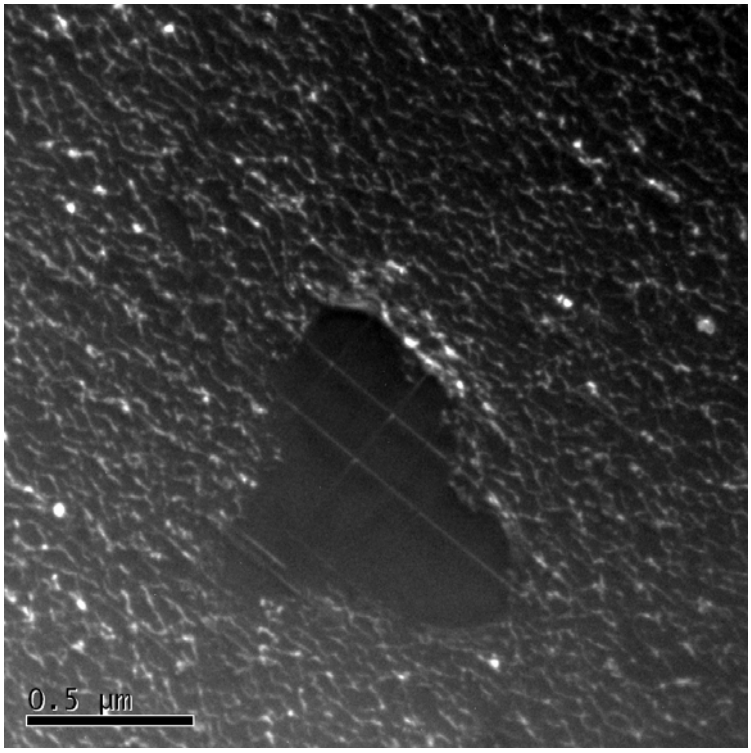

Figure 5-5. PTEM image of strained $Si_{0.74}Ge_{0.26}$ on Si samples implanted with 12 keV Si^+ and annealed showing region etched down from surface to the SiGe/Si interface, reveling the misfit dislocations that contribute to strain relaxation.

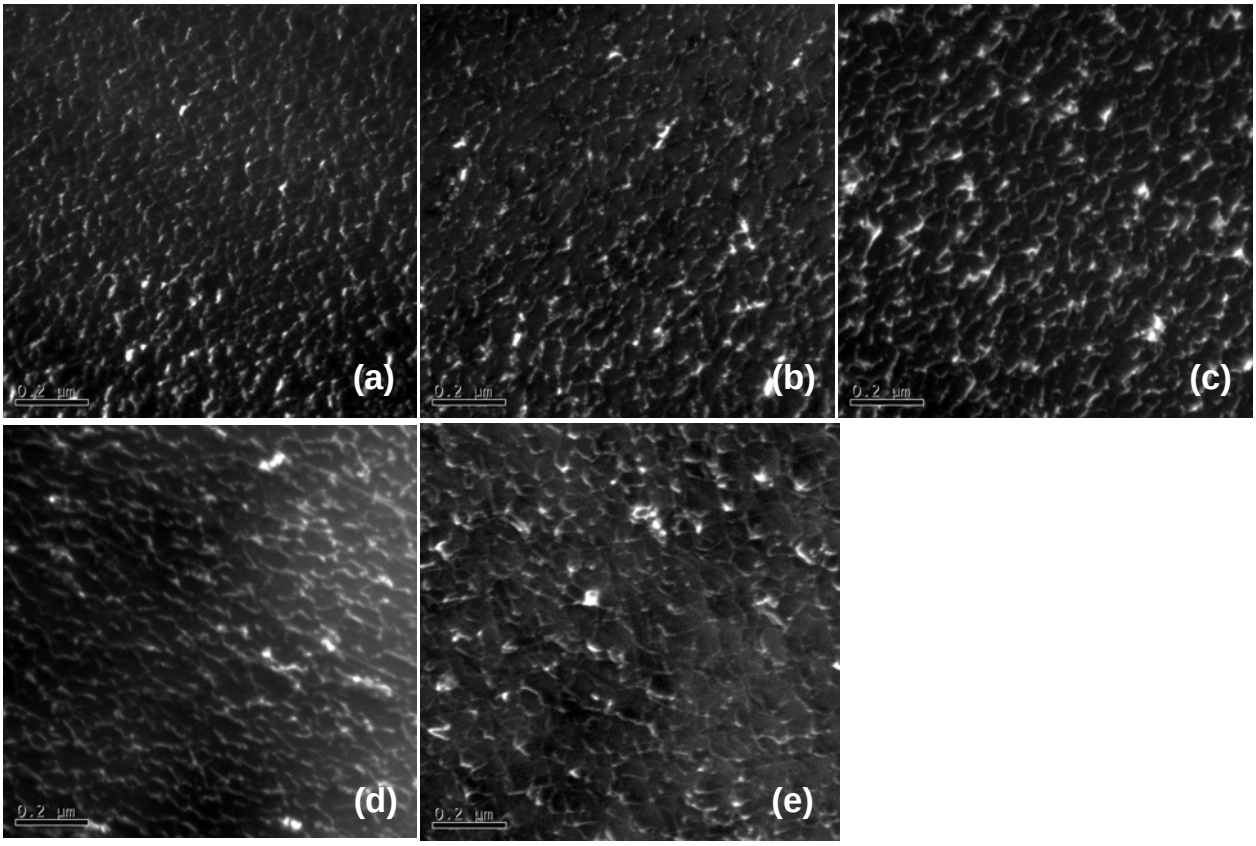

Figure 5-6. PTEM images of strained $Si_{0.74}Ge_{0.26}$ on Si samples implanted with 12 keV Si^+ and annealed at (a) 500ºC (b) 575ºC (c) 650ºC (d) 725ºC (e) 800ºC all for 30 minutes.

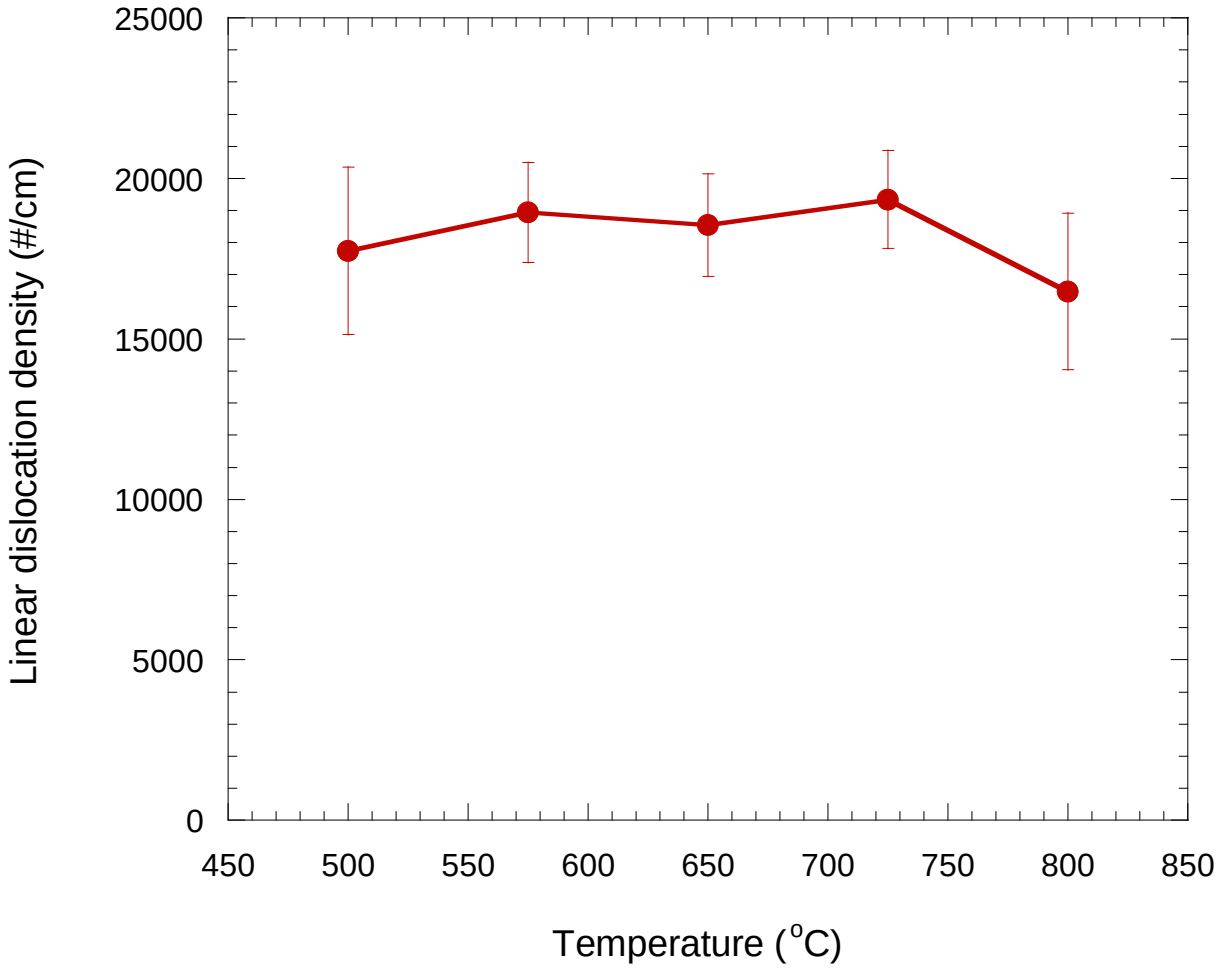

Figure 5-7. Linear dislocation density quantified using PTEM for strained $Si_{0.74}Ge_{0.26}$ on Si samples implanted with 12 keV Si^+ and annealed for 30 minutes at temperatures ranging from 500 to 800 ºC.

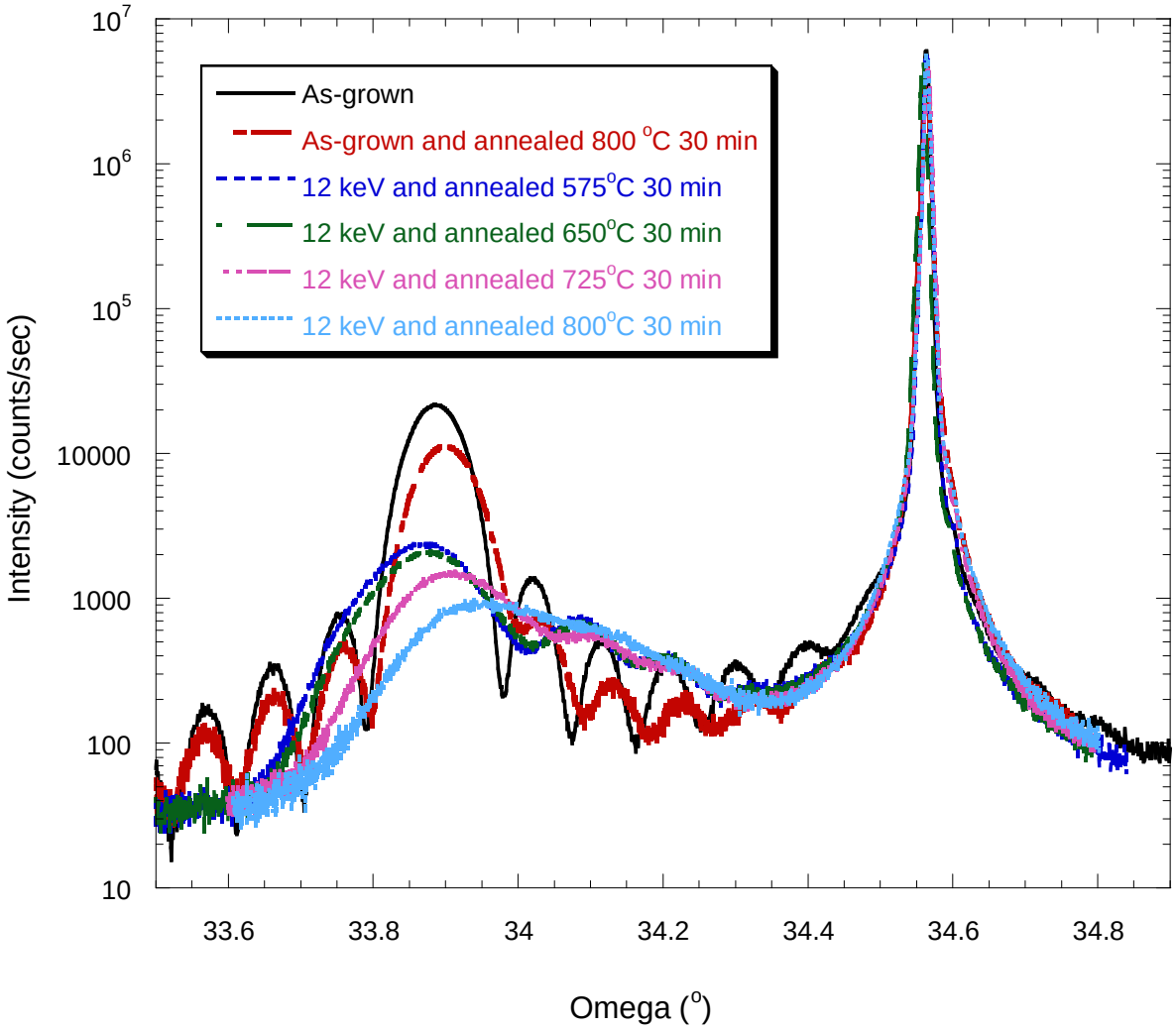

Figure 5-8. XRD RC spectra for strained $Si_{0.74}Ge_{0.26}$ on Si samples implanted with 12 keV Si^+ and annealed for 30 minutes at temperatures ranging from 500 to 800 ºC.

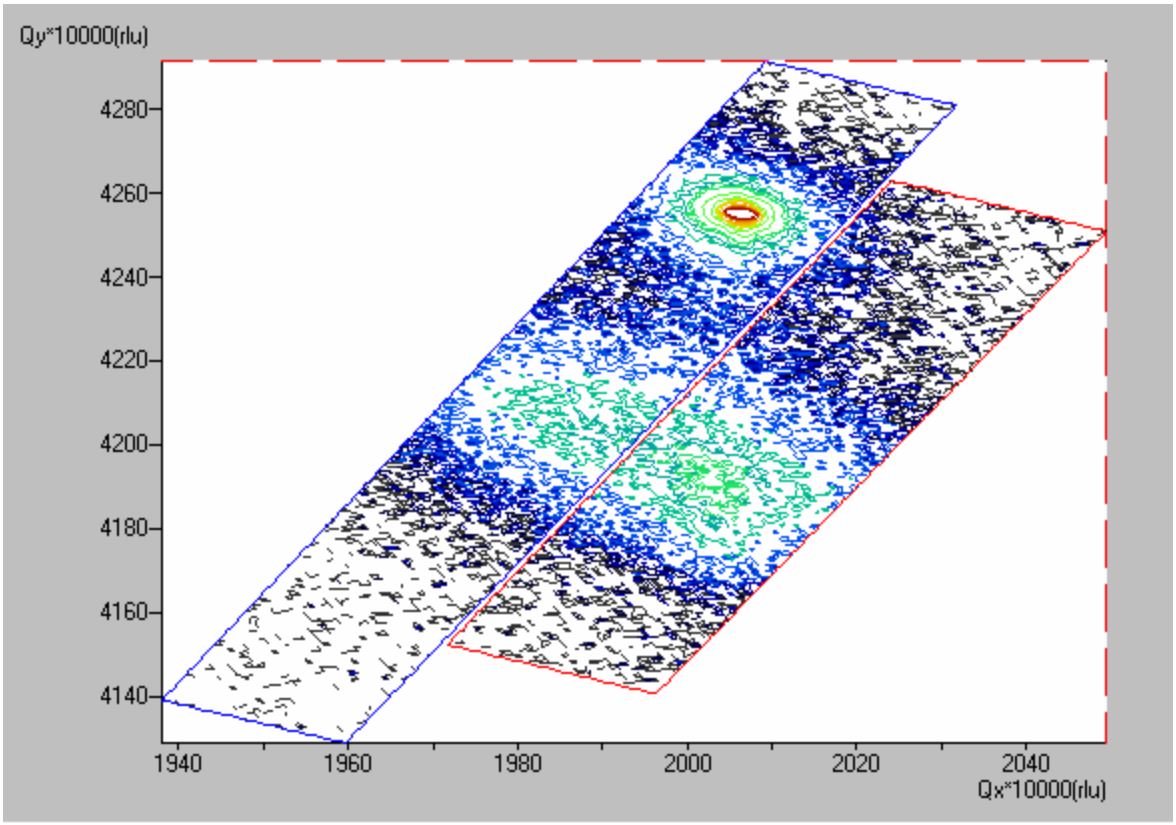

Figure 5-9. HRXRD (113) reciprocal space map for strained $Si_{0.74}Ge_{0.26}$ on Si samples implanted with 12 keV Si^+ and annealed at 800 ºC for 30 minutes.

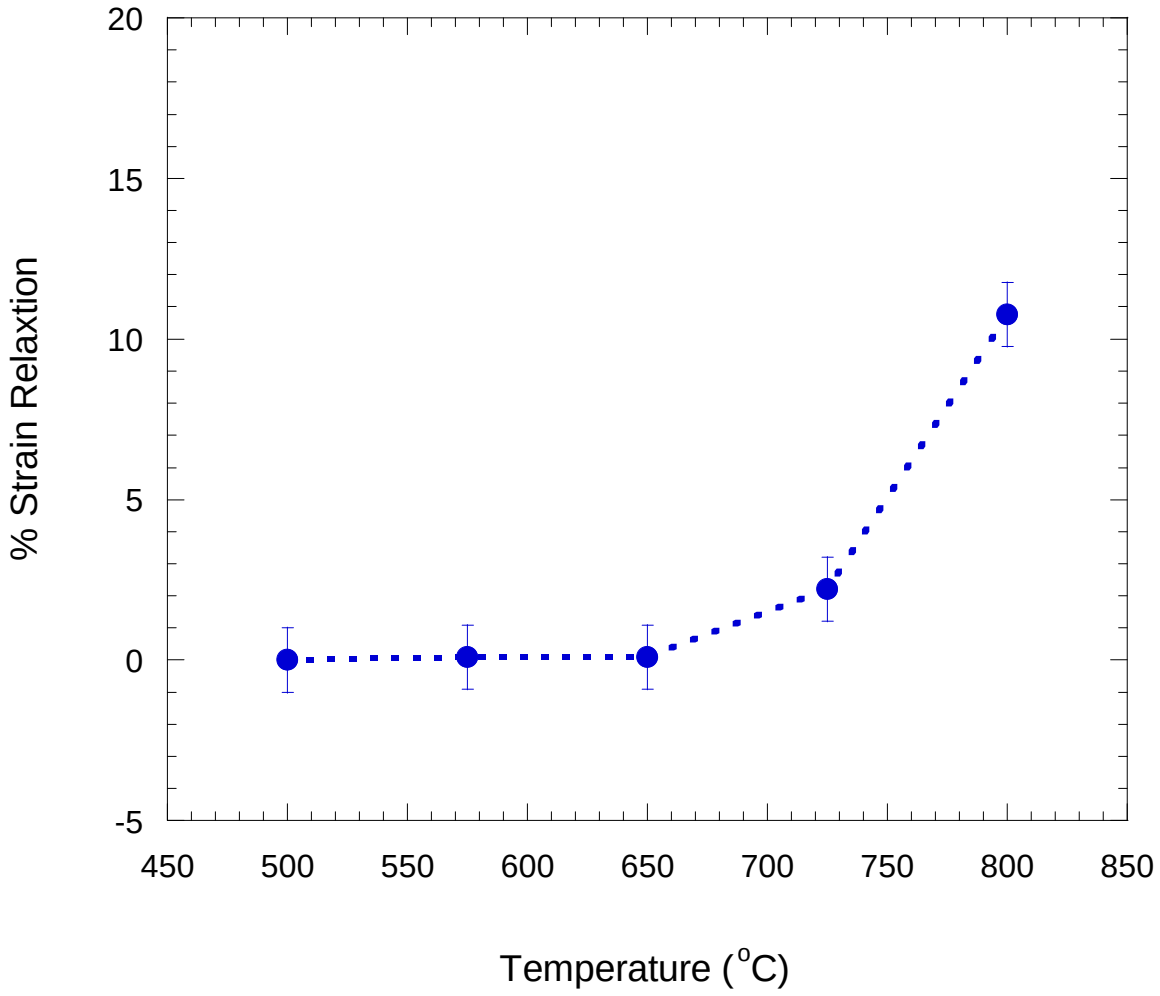

Figure 5-10. Average strain relaxation from RC data for strained $Si_{0.74}Ge_{0.26}$ on Si samples implanted with 12 keV Si^+ and annealed for 30 minutes at temperatures ranging from 500 to 800 ºC.

CHAPTER 6
COMPRESSIVE STRAIN: PROXIMITY EFFECT

The epitaxial interface of the strained silicon germanium structures used in this work may act as a sink for excess interstitials generated during implantation and thus influence strain relaxation during SPER. It is imperative, therefore, to understand if the proximity of the a-c interface to the epitaxial interface impacts defect nucleation and thus strain relaxation. To determine if such an effect is occurring, this experiment varies the depth of the amorphous layer by varying the implant energy. The quantity of dislocations and degree of relaxation will be monitored to determine if any relationship is present.

Experimental Design

Structures for this experiment were grown using Reduced Pressure Chemical Vapor Deposition (RPCVD) at Texas Instruments, Inc. Pseodomorphically strained 50 nm $Si_{1-x}Ge_x$ was deposited on Si (001) substrate with alloy compositions of 0, 16, 22, and 26 at% germanium. Post growth, the structures were Si^+ ion implanted with varying energies of 5, 12, and 18 keV at a fluence of $1x10^{15}$ atoms/cm^2 to generate continuous amorphous layers with varying proximity to the epitaxial interface while confining them within the strained layer. Once implanted, samples were annealed in a quartz-tube furnace under an inert N_2 ambient environment.

An isothermal study at 800°C for 5, 30, and 300 minutes was carried out to study the effect of the proximity of implantation damage and its evolution to the epitaxial interface on strain relaxation. Ion implantation is a non-conservative process which introduces excess point defects in the system. At temperatures between 600 and 800 °C, the excess point defects recombine and the remaining excess interstitials agglomerate and become 311 defects. On further annealing, the 311 defects dissolve and contribute to the coarsening of dislocation loops. These defects are termed End-Of-Range (EOR) [Bon98, Cri00, Lam99, Nod00, Uem99]. At temperatures above

800ºC, dislocations loops in the EOR coarsen at the expense of smaller loops and 311s. Since it is likely that strain relieving misfit dislocations may be nucleated at or near the EOR damage created by ion implantation, the proximity of the EOR damage to the Si/SiGe interface may influence the number and type of defects formed and hence affect the degree of strain relaxation. Thus, this experiment varied both strain and implant energy in order to investigate the effect of the proximity of the EOR to the epitaxial interface on strain relaxation as a function of initial strain. Once annealed, the strain state and crystalline quality will be characterized.

A Pananalytical MRD X'Pert was used to obtain XRD Rocking Curves (RC) and Reciprocal Space Maps (RSM) to obtain the degree of relaxation observed post anneal. A JEOL 2010F high-resolution transmission electron microscope (HRTEM) and a JEOL 200CX TEM were used to study cross-sections (XTEM) of the regrown layer. Samples were prepared using a Dual-Beam FEI Strata DB 235 Focused Ion Beam. XTEM measurements were used to confirm the amorphous layer depth and layer thicknesses. Plan-view (PTEM) samples were also prepared and imaged using a JEOL 200CX operating at 200kV using g_{220} weak-beam dark-field (WBDF) imaging to quantify dislocation density.

Results

As-Implanted Sample Analysis

Analysis of the as-grown samples can be found in the previous chapter. The experiment in this chapter varies the implant energy in order to change the proximity of the a-c interface to the epitaxial interface. All implants were tailored to be confined within the strained layer. Previous work suggests that the amorphization threshold decreases with increasing Ge concentration due to a decrease in binding energy [Hay92, Lie93, O'Ra96]. The amorphous depths of the implants in this work were measured using XTEM and are presented in Figure 6-1. XTEM of as-implanted SiGe and Si samples confirmed that the amorphous depths varied with higher Ge

concentrations and higher implants energies, in agreement with prior findings. The varying initial amorphous depth complicates the experiment by altering the final interstitial profile and thus will alter the quantity of excess interstitials. If this is the case, and if the defect nucleation and density is dependent on the number of interstitials present, the effect will be observed in the quantitative PTEM study.

Proximity Effect Experiment

Two major variables were varied in this experiment: magnitude of strain and implant proximity. First, the result will be presented in terms of strain. All Ge compositions were implanted with 12 keV Si^+ and annealed at 800 ºC for 30 minutes. The XRD (left column) and XTEM (right column) data for all concentrations of Ge is presented in Figure 6-2. XRD (004) RC of the as-grown and as-grown annealed cases are accompanied with the implanted and annealed case to confirm that any enhanced relaxation is due to the SPER process alone. The as-grown and annealed sample shows no change in peak position but has a slight decay in peak amplitude due to the formation of misfit dislocations as seen in PTEM (not shown). With increasing Ge, this effect is accompanied with a slight peak shift indicating a slight relaxation due to anneal alone.

After implantation and anneal of the 16% Ge sample, thickness fringes are still present in the XRD RC spectra indicating that the epitaxial interface is still accommodated elastically, presented in Figure 6-2 (a). As the Ge composition is increased, Figure 6-2 (c) and (e), an absence of these fringes is observed indicating that the interface has been compromised. Also, with increasing strain, the defects increase in density and the degree of strain relaxation increases. The percent strain relaxation indicated above the XRD spectra is the average relaxation of the implanted and annealed case. The average degree of strain relaxation increases with increasing strain as shown by the peak broadening and peak shift in the RC spectra. This

increased relaxation and decreased crystalline quality is confirmed using XTEM images. For the 16% Ge sample, Figure 6-2 (b), the defects are near the surface and do not propagate down to the interface. Thus, negligible strain relaxation was observed. In the case of the highest strained sample, 26% Ge, the defects propagate down towards the interface, as seen in Figure 6-2 (f) and is accompanied with a higher magnitude of strain relaxation. The quantity and depth of the regrowth related defects also increases with increasing Ge, as observed by comparing Figure 6-2 (b,d, and f). This is observed with the increasing relaxation and decreased crystalline quality in the XRD data as a function of Ge content.

A similar comparison is made in terms of implant proximity. The XRD and XTEM data of the 16% Ge samples implanted with 5, 12, and 18 keV Si^+ and annealed for 30 minutes at 800 ºC are presented in Figure 6-3. For the 5 and 12 keV implanted samples, all of the peak oscillations are still present and indicate that the interface is still intact though these samples show an additional decay in amplitude due to defects present in the regrown layer. A slight peak shift is also observed and indicates strain relaxation less than 1%. The 18 keV implanted case, with the closest proximity to the interface, shows a larger peak shift indicating greater relaxation and an absence of the fringes indicating that the interface uniformity has been disrupted. In Figure 6-3 (b-d), XTEM corroborates the XRD results by showing an increase in both depth and density of regrowth related defects with increasing interface proximity (increasing implant energy). These results suggest that the degree of relaxation is largely dependent on proximity of the a-c interface to the epitaxial interface.

Further examination of all samples using PTEM elucidates the defect microstructure and density. All samples in the experimental matrix were annealed at 800 ºC for 5, 30, and 300 minutes. The PTEM for the 30 minutes annealed samples are shown in Figure 6-4. PTEM

images provide a two dimensional representation of the defects; defects that extend deeper into the substrate will appear to have longer segments. This is observed with increasing proximity (implant energy). The results observed in XTEM are further confirmed in these PTEM images. For the 16% Ge case, the quantity of defects appears smaller in the lower implant energies due to the dependence of defect formation on the depth of the implant. The same can be said for the higher Ge samples, the defect segments appear to be longer with increasing implant energy, therefore, the defects extend deeper into the layer.

One advantage of PTEM is the ability to observe the microstructure and to quantify the defects. A linear dislocation density is quantified perpendicular to the direction of the g vector. The defect density calculated in this manner is presented in Figure 6-5 and is accompanied with the relaxation data from the XRD RC. The strain relaxation and proximity both have a linear relationship to initial strain (% Ge) and show the effect of proximity on the relaxation process. The stability of these defects was examined with isothermal anneals. The defect density for the 18keV case, annealed at 800 °C for 5, 30, and 300 minutes, is presented in Figure 6-5. This plot shows that neither the microstructure nor the defect density changes with further annealing. These results indicate that the defects are quite stable at 800 ºC. Finally, the average degree of relaxation for the proximity experiment is summarized in Figure 6-7. The increase in relaxation is observed as the a-c interface is placed closer to the interface and as the initial strain level (% Ge) is increased.

In summary, the results show that the relaxation and subsequent defects are dependent on both initial strain magnitude and proximity of the implant to the epitaxial interface. The implications of these results will be discussed in the next section.

Discussion

Most of previous SPER experiments have been conducted using highly metastable SiGe layers of more than 200 nm thick and amorphizing implants passing through the Si/SiGe interface [Ang07, Hon92, Lee93]. The results from these experiments showed defect nucleation once the a-c interface passed the Matthews-Blakeslee (M-B) critical thickness [Mat74]. The authors of these works attributed the defect nucleation and subsequent strain relaxation to be related to the theoretical critical thickness. Additionally, similar work was done in thinner layers, around 30nm, with amorphous layers also passing through the Si/SiGe interface [Chi89, Rod97]. The results from these experiments also showed a relationship to the theoretical critical thickness. Rodriguez et al. conducted an experiment with both doped and undoped samples and found that the doped samples regrew past the M-B critical thickness before defects were nucleated. The authors, therefore, concluded that the critical thickness was altered due to a decrease in strain with dopant incorporation [Rod97]. According to M-B criteria, all of the experimental structures in this work are grown in a metastable state with the strained SiGe layer thicker than the critical value. If a similar relationship to M-B critical thickness is observed upon regrowth, the strained samples in this study should regrow with no defects or loss of strain within the following distances from the Si/SiGe interface: 16% 20nm, 22% 13 nm, and 26% 10 nm [Mat74]. Above these values, defects should nucleate and extend to the surface of the wafer.

The proximity experiment results, however, are contrary to the previous findings. The defect-free thickness (critical thickness) for all samples in this study is plotted against M-B critical thickness in Figure 6-8. The M-B criterion is observed for samples with lower strain and implant energy combination. However, at a critical strain and implant energy combination, defects are observed below the theoretical calculations. The difference in relaxation mechanism is key to the understanding of this discrepancy. M-B criterion is based on an energy balance in

which the stability is described by relative energies of the two competing interfacial structures. The energy to generate a dislocation and the elastic energy for strain compensation is balanced to determine the critical thickness [Mat74, Van63]. The assumption is that the strain is accommodated by generation of 60° misfit dislocation. However, as seen in the results from the prior chapter, the relaxation is accompanied by defect nucleation due to the roughening of the a-c interface. Furthermore, these defects are regrowth-related. The nucleation of defect introduction is this work is not similar to the kink model and generation of misfits as described by M-B and thus cannot be used to determine the critical thickness for SPER breakdown observed in these samples.

As predicted by Srolovitz and discussed in Chapter 5, the a-c interface increases in roughness until an equilibrium perturbation is reached [Sro89]. Hairpin dislocations are formed when the competing growth fronts of the rough a-c interface meet during regrowth. Therefore, shallower implants like the 5 keV do not have time to reach this equilibrium before regrowth is complete, resulting in a lower wavelength than the deeper implanted samples. Since the equilibrium wavelength dictates when the defects are nucleated, shallower implants will nucleate a lower number of defects. With the deeper 12 and 18 keV implants the layers are deep enough to reach their equilibrium wavelength before regrowth is complete. This explains why a higher number of defects are observed when deeper implants are performed. Also, by comparing the PTEM in Figure 6-3, it can be seen that the defect density reaches saturation with a deep enough implant. This corresponds to the equilibrium value of the roughness wavelength. Furthermore, the stability of the defect density at longer anneal times, presented in Figure 6-5, indicates that once the defects are nucleated as the a-c perturbation reaches equilibrium and SPER commences, no further growth or evolution of the defects is observed. More importantly, there is no evidence

of the regrowth defects gliding down to the interface upon further annealing as observed in the tensile strain case and discussed in Chapters Three and Four. Instead, below the critical strain and proximity the defects are contained within the layer.

These observations support the conclusion that the relaxation behavior is different when implants are contained within the layer than when they are performed though the layer. According to the critical thickness criteria, the proximity of the implant should not play a major rule in the relaxation or depth of defect nucleation. Regrowth should always be defect-free below the critical thickness. This difference is likely due to the localized strain increase due to implantation and the regrowth taking place within the strained layer itself. Specifically, the impact of the implant to the strain state must be considered. Placing the implant within the layer will impact the strain magnitude of the layer [Gla97, Kri95b, Lie95]. The point defects generated by the implant add to the overall magnitude of strain and place it in a higher state of compression. Thus, the proximity of the projected range in relation to the epitaxial interface will impact the amount of strain in the material. This, in turn, impacts the location of defect nucleation as observed. Another variable to consider with varying implant energy is the net interstitial population contributing to defect nucleation. Prior work by Gutierrez [Gut01b] and King [Kin03] have shown that the net interstitials do no change as a function of energy at these low energies and the proximity of the damage to the surface does not have an effect on the trapped interstitial population. Since the interstitials in the strained SiGe sample did not agglomerate as observed in Si, the trapped interstitial population could not be determined.

Another important observation is that the regrowth-related hairpin defects are seen to extend deeper into the film than the original a-c interface. This has not been reported in prior work. As the anneals were done at a higher temperature, a higher thermal budget was seen by

the samples after regrowth was complete. It is thus possible that another mechanism was being activated once regrowth was complete, namely dislocation climb. Climb generally occurs at temperatures greater than half of the materials melting point [Hir68, Rea53] which is true for this case. Climb is a point defect diffusion process and occurs by diffusion of either vacancies or interstitials. It is assumed that a large number of free interstitials exist within the SiGe layer since no agglomeration of point defects is observed. These "free" interstitials are thus readily available for mediating motion and elongation of the hairpin defects below the original a-c interface. This reasoning could explain the discrepancy in the XRD and PTEM data presented in Figures 5-7 and 5-10, where the dislocation density remains constant as a function of anneal temperature but the XRD data shows further relaxation after annealing above 700 °C. To confirm this hypothesis, further experiments are needed that alter the point defect population while keeping the proximity constant.

Conclusion

The relaxation of the regrown layer is quite different when the strain is in a state of compression versus tension. For the compressive state, results have shown that defects were nucleated when the competing growth fronts of the rough a-c interface meet during SPER. The a-c interface roughness is shown to increase with increasing initial strain. The defect density also shows a similar trend. Therefore, it is evident that there is a correlation between a-c interface roughness and defect density. These defects are also stable and reach saturation beyond a critical strain and implant depth. The defect nucleation is highly dependent on both strain and proximity of the implant. Additionally, lower strain and shallower implant depths cause the formation of a localized layer of defects that do not extend down to the epitaxial interface even after further annealing. While this region above the a-c interface regrows with poor crystalline quality and an abundance of hairpin dislocations, these dislocations remain confined within the

regown region and do not affect the strain at the Si/SiGe interface. The hairpin dislocations do, however, cause some localized strain relaxation as observed with XRD measurements. At higher strain (above 22% Ge) and implant energies (above 12 keV), the entire SiGe layer is defective and further strain relaxation is observed. Overall, this is contrary to the tensile case where the regrowth defects always extend down to the epitaxial interface after regrowth regardless of the initial a-c interface position. These regrowth related defects were observed to nucleate misfit dislocations and cause further relaxation than annealing alone (no implants).

It is therefore plausible to conclude that the critical thickness is varied when the implant is contained within the layer versus one that is performed though the layer. This is likely due to the localized strain increase due to implantation and the regrowth taking place within the strained layer itself. Additionally, when implants are performed within the layer, the proximity of the a-c interface placement with respect to the epitaxial interface plays an important role in both defect nucleation and strain relaxation. Furthermore, the assumptions upon which the Mathews-Blakeslee critical thickness was calculated cannot be applied to the present case. The relaxation mechanism itself is quite different as discussed.

In summary, prior works have extensively studied strain relaxation and SPER in supercritical SiGe films where implants were conducted through the Si/SiGe interface. However, the effect of implant proximity to the Si/SiGe interface and how it affects defect nucleation and relaxation for implants within the layer was not well understood. This work investigates this effect and has deemed it inappropriate to apply Matthews-Blakeslee's criteria to these sample conditions. Matthew-Blakeslee's criteria are calculated under equilibrium conditions. However, once the implant is conducted within the strained layer, it is a non-equilibrium process and Matthews-Blakeslee criteria cannot be applied. Also, prior work has

been deficient in determining the relationship between defect microstructure and strain relaxation upon SPER. This work has shown a correlation between defect density and strain relaxation. Additionally, the results in this study conclude that the a-c interface roughening is the dominant factor in the defect nucleation and that the defects were a/2<110> type dislocations.

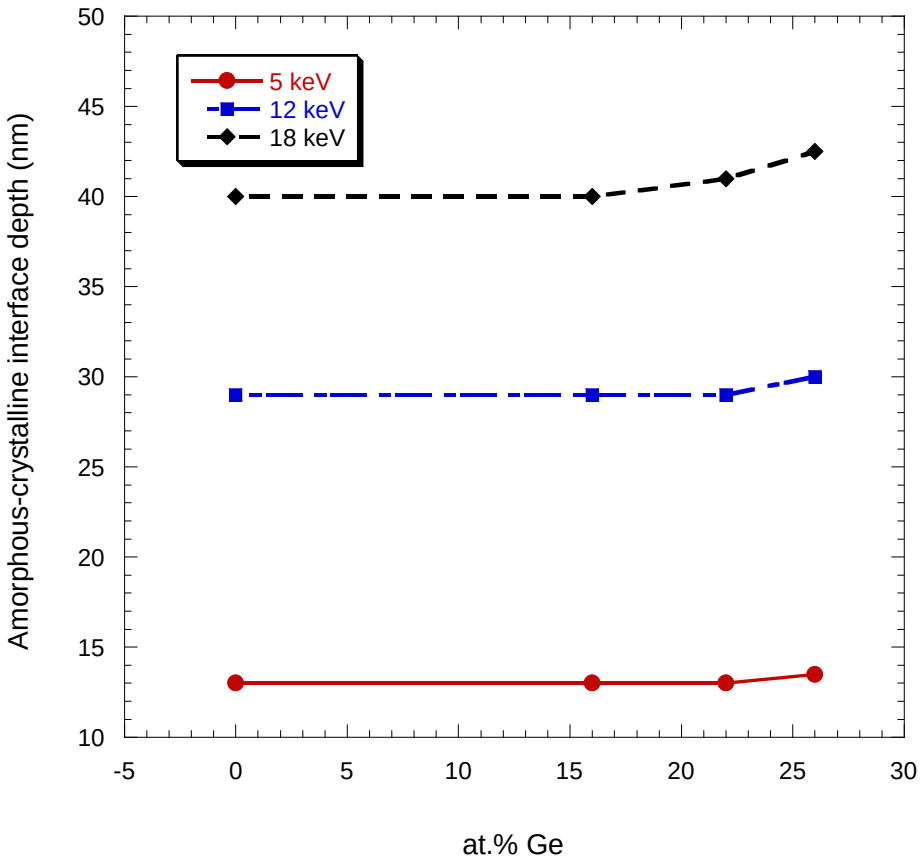

Figure 6-1. Amorphous depth measurements using XTEM for all strained $Si_{1-x}Ge_x$ on Si samples implanted with 5, 12, and 18 keV Si^+ shown as a function of Ge concentrations.

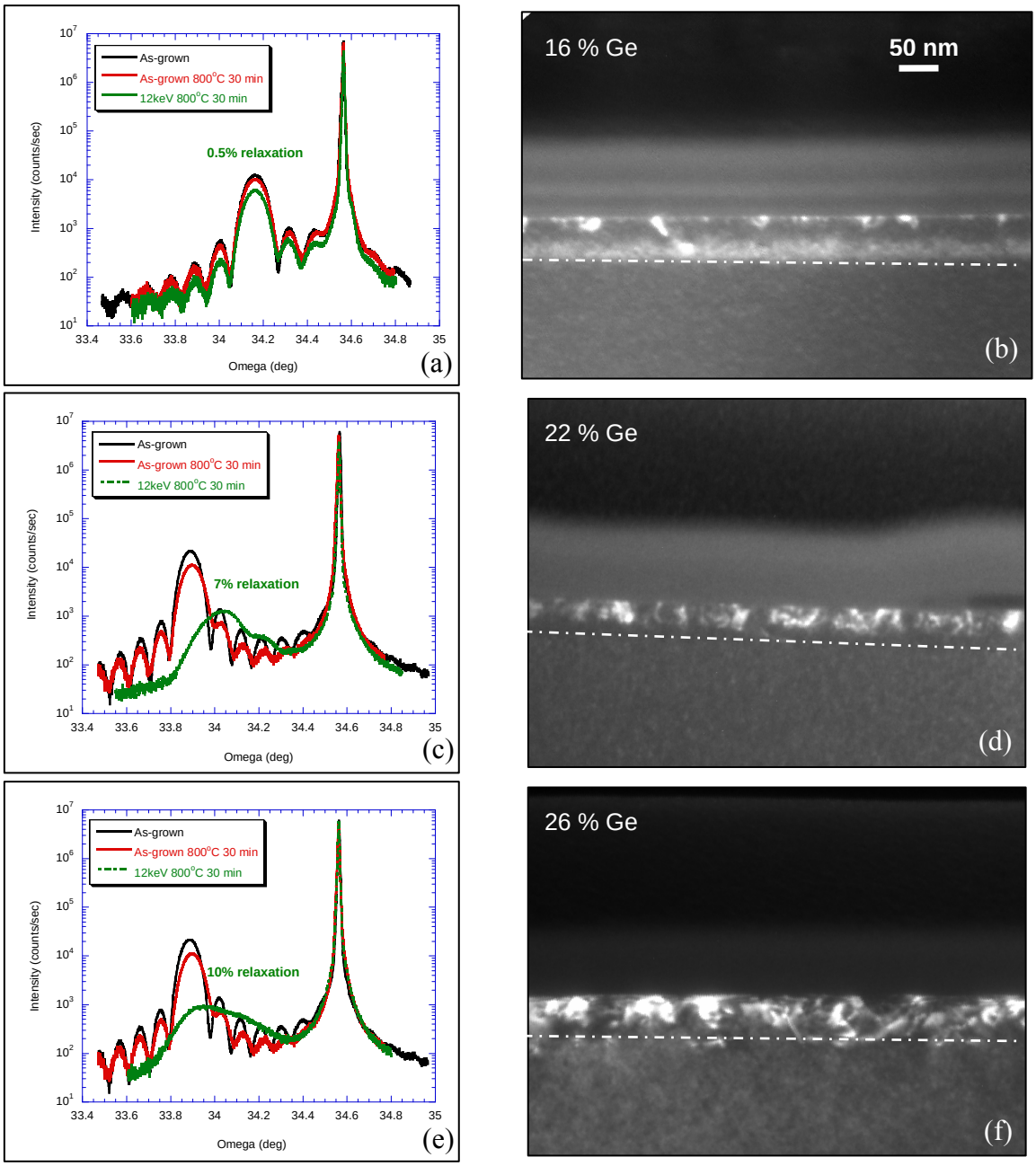

Figure 6-2. All 12keV Si^+ implanted with varying Ge concentration (a) 16% (b) 22% (c) 26% XRD RC on the left with corresponding XTEM on the right.

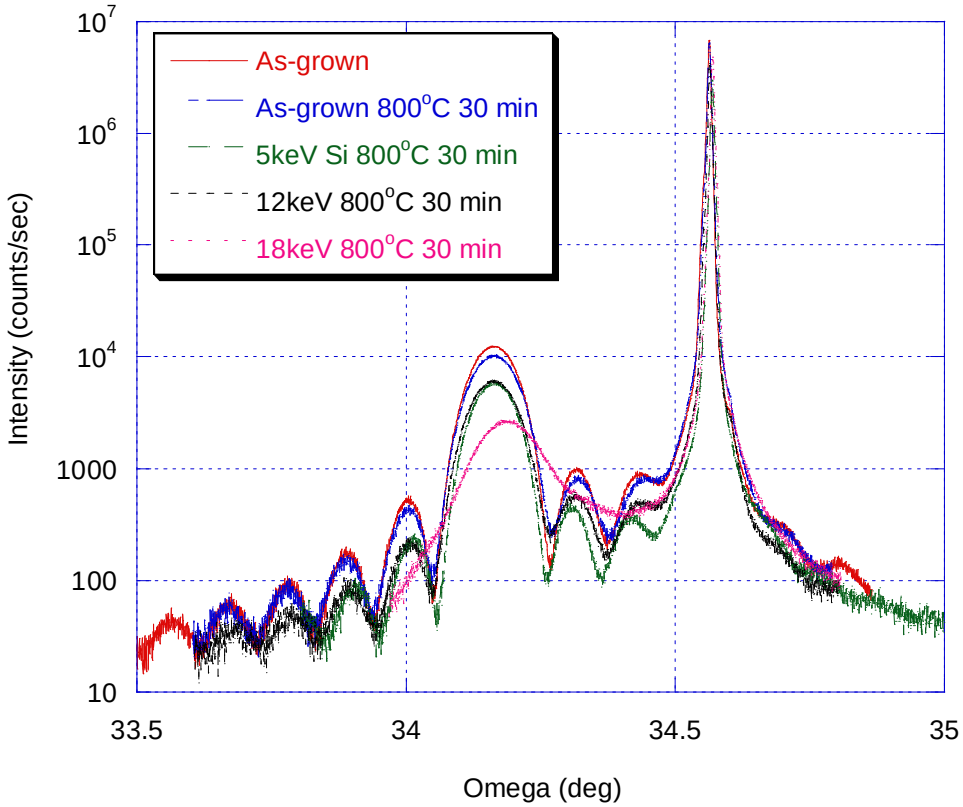

(a)

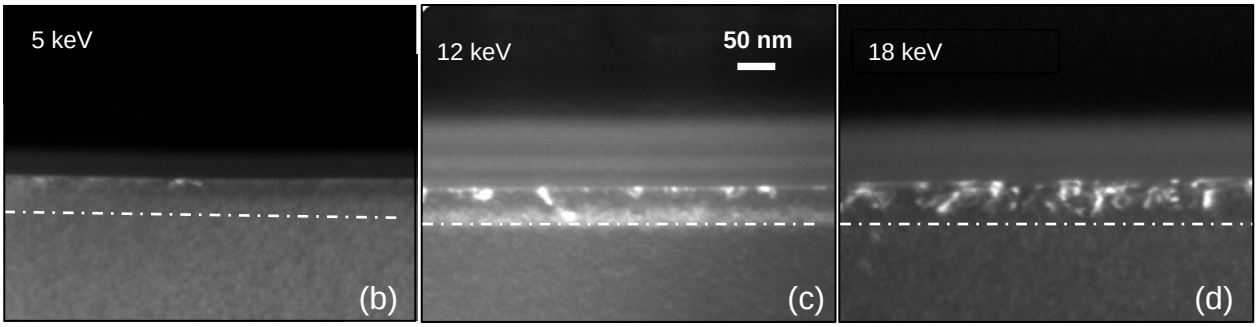

Figure 6-3. (a) XRD (004) RC of 5, 12, and 18keV 16% Ge samples. PTEM of 16% Ge sample implanted with (b) 5keV (c) 12keV and (d) 18keV Si^+ implants. All samples annealed for 30 minutes at 800 ºC.

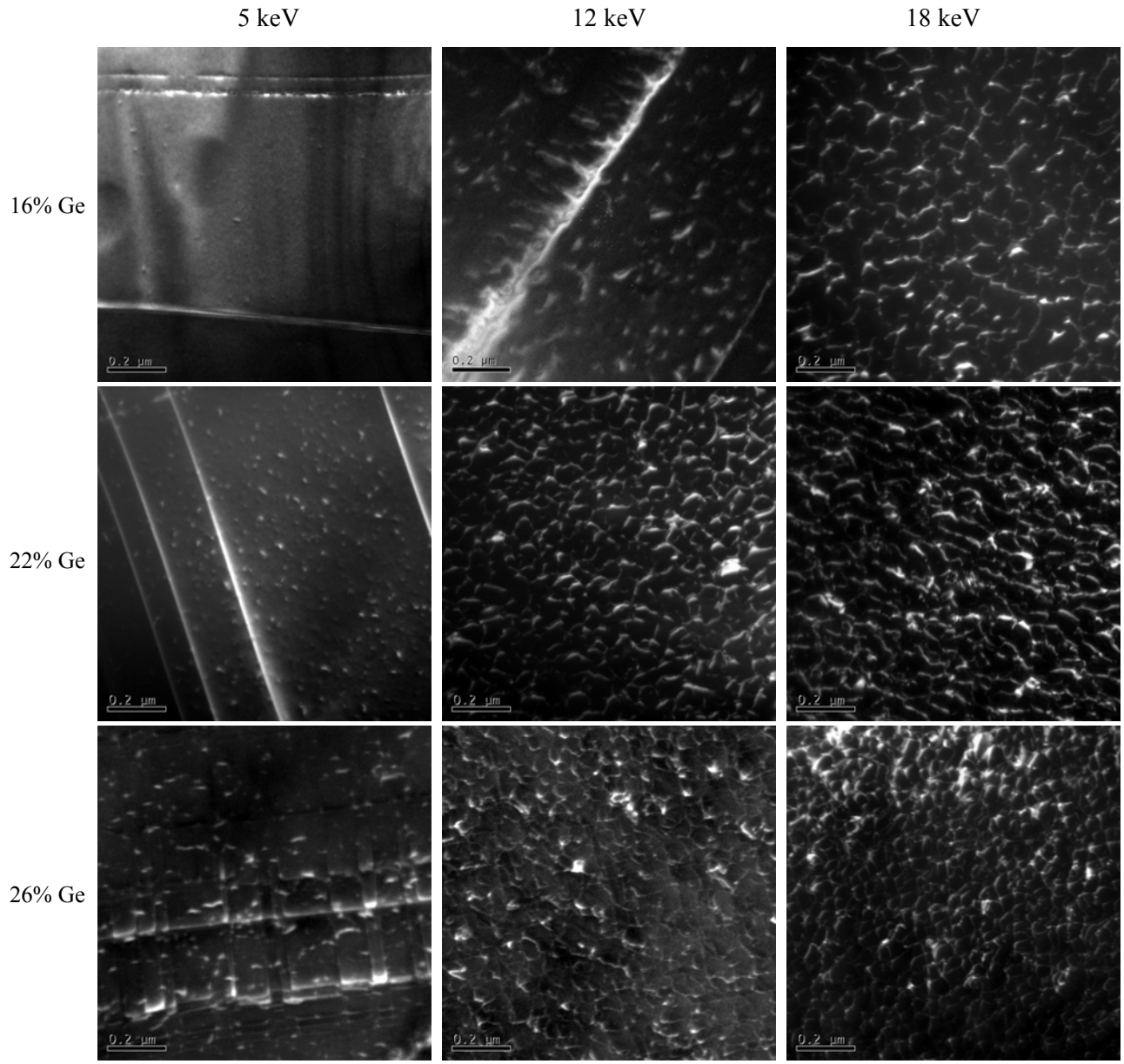

Figure 6-4. PTEM of 5, 12, and 18keV Si^+ implanted samples annealed at 800 ºC for 30 minutes as a function of germanium concentration.

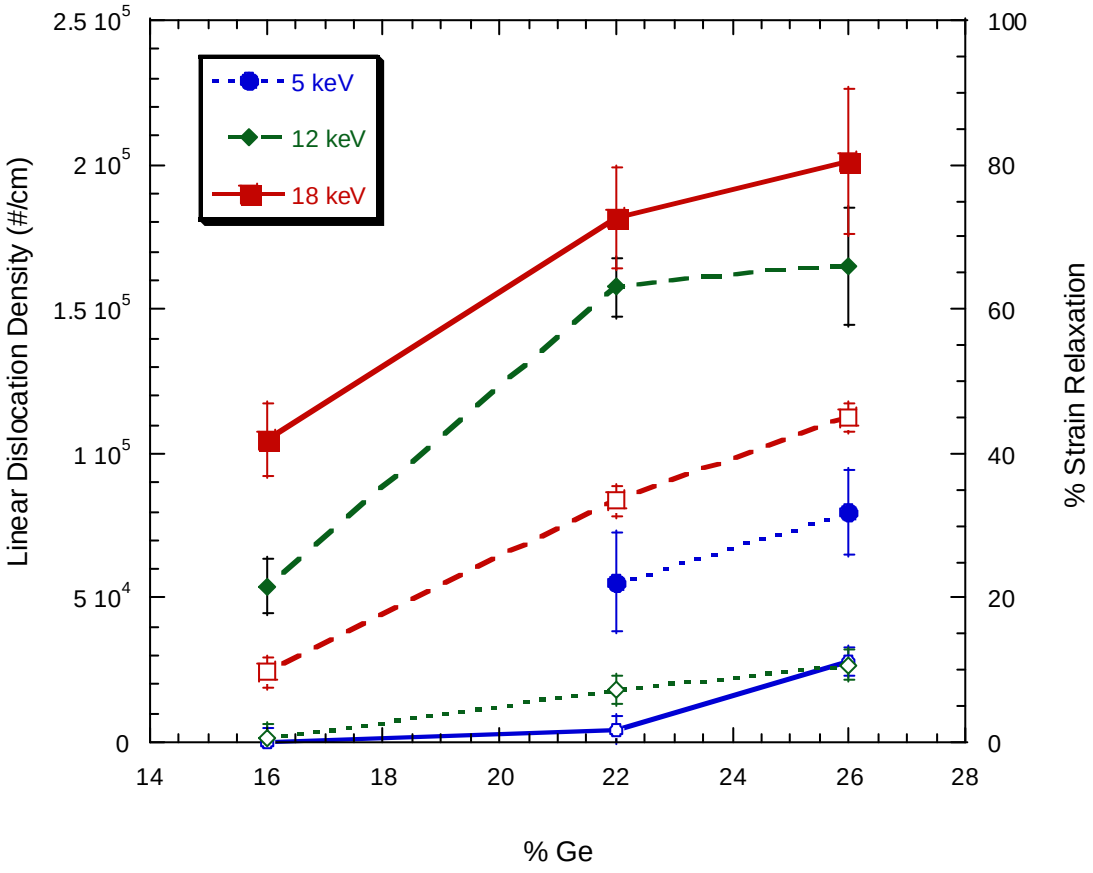

Figure 6-5. Linear dislocation density (filled markers) and %Strain Relaxation (unfilled markers) for 5, 12, and 18keV Si^+ implanted samples annealed at 800 ºC for 30 minutes as a function of germanium concentration.

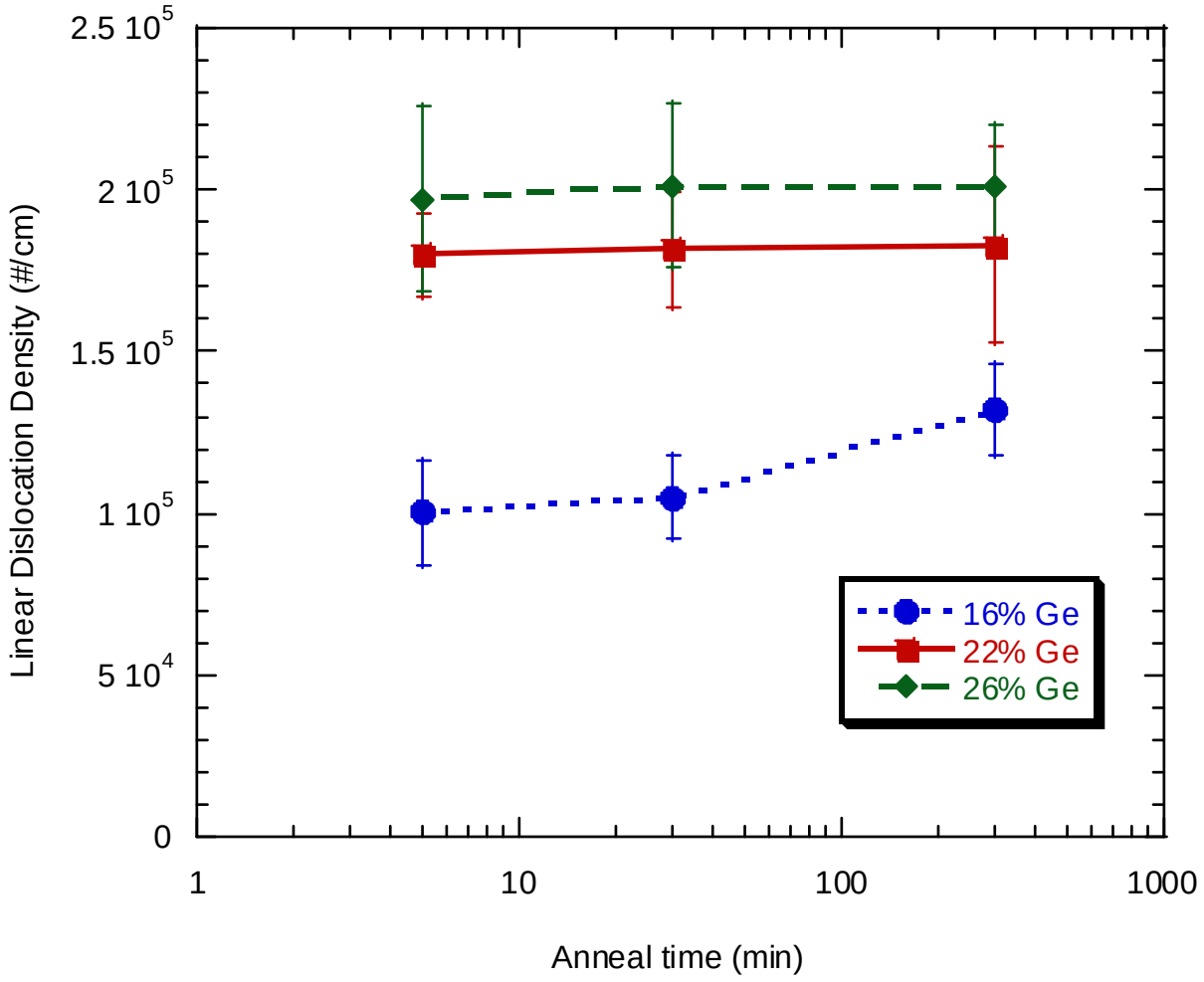

Figure 6-6. Linear dislocation density of 18keV Si^+ implanted samples annealed at 800 ºC for all germanium concentration.

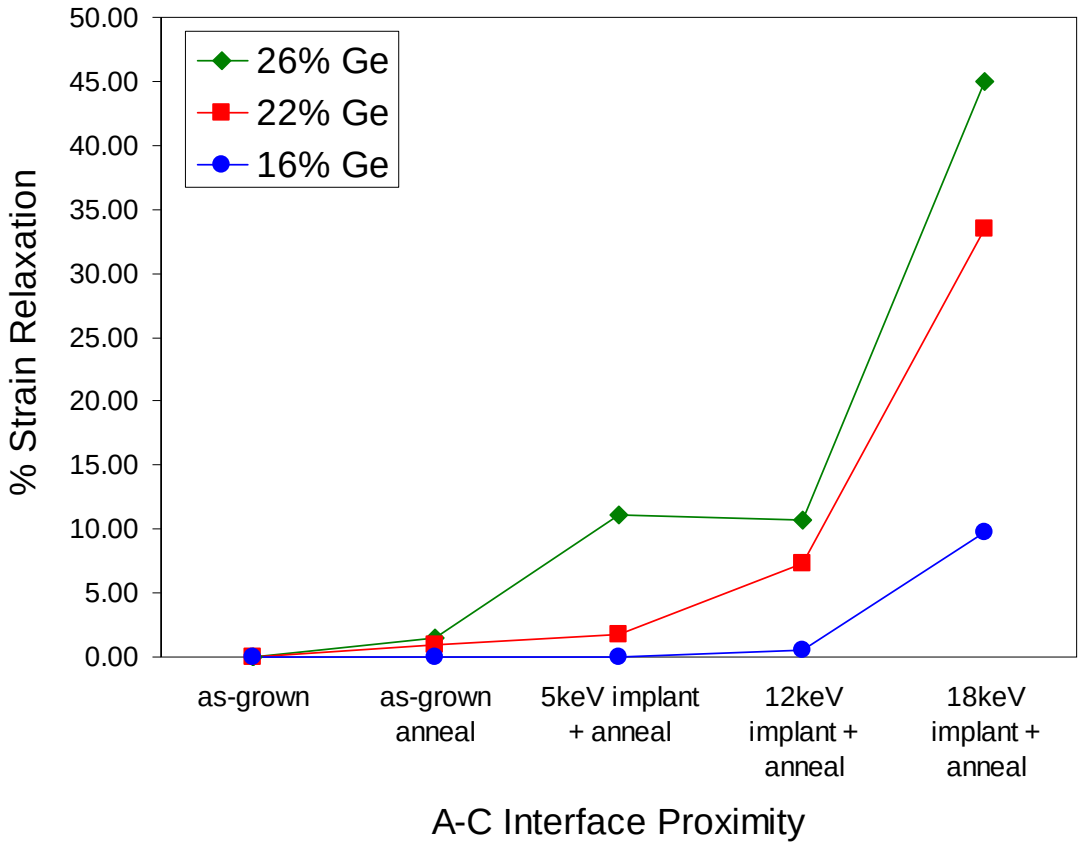

Figure 6-7. Summary of %Strain relaxation obtained from XRD RC data for all samples annealed at 800 ºC 30 minutes.

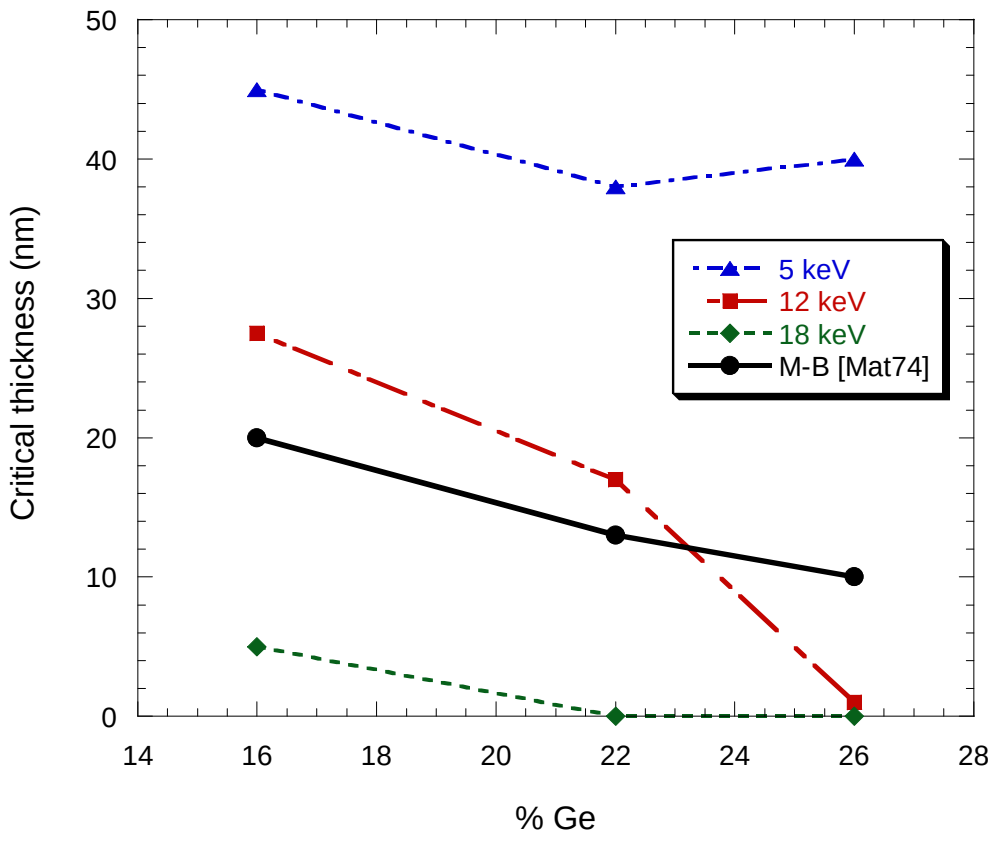

Figure 6-8. Critical thickness, measured using XTEM, for all samples conditions annealed at 800 °C for 30 minutes.

CHAPTER 7
SUMMARY AND COMPARISION

Overview

The effect of an amorphizing implant contained within a strained layer has not yet been studied, nor has the crystalline quality or thermal stability of such an amorphized region. These effects may be important for future device structures, as arsenic and phosphorus, both self-amorphizing implants, are often used to create channel extensions in NMOS devices. Additionally, Solid Phase Epitaxial Regrowth (SPER) is carried out under strain in stress memorization techniques. The purpose of this work is to study the effect of these processing conditions as a function of strain, especially concerning the degree of relaxation, stability after amorphization and regrowth, crystalline quality of the regrown layer, and proximity of implant to the heterostructure interface.

Si/SiGe heterostructures were used to study the effect of strain post amorphization and regrowth. All tensile strained layers in this study are in a metastable state because of the low temperature growth procedure. Additionally, all compressively strained layers are also metastable according to Matthews-Blakeslee criteria.

Summary

Tensile Strain Case

Tensile strained Si structures were grown on relaxed $Si_{1-x}Ge_x$ (Ge fractions of 0, 10, 20, and 30) virtual substrates via Molecular Beam Epitaxy (MBE). A 630 nm thick fully relaxed $Si_{1-x}Ge_x$ layer of corresponding composition was then grown on top of the buffer layer, followed by a 50 nm strained silicon capping layer [Gai00]. The strain of the structures was experimentally determined using lattice parameters, obtained from HRXRD. The results from this analysis

show that the capping layers grown on $Si_{1-x}Ge_x$ with Ge fractions of 0, 10, 20 and 30 correspond to a Si layer strain of 0, 0.37, 0.74, and 1.1% strain, respectively.

The structures were then implanted with Si^+ at an energy of 5, 12, or 18 keV and a fluence of $1x10^{15}$ atoms/cm^2 to generate continuous amorphous layers confined within the strained layer. Next, isothermal and isochronal anneals were performed in a quartz-tube furnace under an inert N_2 ambient environment. These experiments were carried out to determine specific factors that affect the relaxation process.

The results for the tensile case study are discussed in Chapter Three and Four and are summarized here. Under biaxial tension there is a critical strain for SPER breakdown that lies between 0.74 and 1.1% strain. Thus, strained silicon can be amorphized and regrown without strain relaxation for all $Si_{1-x}Ge_x$ compositions up to $Si_{0.8}Ge_{0.2}$ (0.74% strain). For the 1.1% strained ($Si_{0.7}Ge_{0.3}$) sample, the solid phase regrowth of the amorphous layer breaks down and results in the formation of regrowth related defects within the amorphous region. These defects then extend back down to the strained Si/ $Si_{1-x}Ge_x$ interface upon completion of regrowth. This is the first observation of regrowth related defects extending below the amorphous/crystalline interface. Additionally, the EOR evolution and population seems to be altered in the presence of tensile strain; the evolved dislocation loops are fewer in number especially in the relaxed Si on $Si_{0.7}Ge_{0.3}$ sample. This indicates that, in conjunction with a certain level of initial strain, excess interstitials are providing a source for the generation of extrinsic stacking faults which then nucleate misfit dislocation. Thus, implantation increases misfit dislocation density and promotes further relaxation than annealing alone. The possibility of excess interstitials acting as a source for misfit dislocation nucleation was further explored in the proximity experiment. In summary,

these results indicate that a critical misfit strain between 0.74% and 1.1% results in a breakdown of the SPER process and the formation of extended regrowth related defects.

These defects nucleated as the a-c interface progresses towards the interface during SPER, forming regrowth related defects. Once fully regrown, these defects propagate down to the interface, promoting enhanced strain relaxation of the layer than annealing alone. The regrowth related defects are primarily stacking faults rather than the traditionally observed hairpin dislocations. Since strain relaxation was only observed when these regrowth related defects were present, the results suggest that these defects are contributing significantly to enhanced relaxation of the strained layer.

Furthermore, the relaxation process is a thermally activated glide process with activation energy of 0.7 ± 0.2 eV. This value is significantly less than the 2.2 eV activation energy for dislocation glide observed in bulk Si. The difference is theorized to be due to the formation term in this work being negligible since the defects are formed as a result of SPER breakdown. Thus, the activation energy in this work is dominated by the migration term. Overall, the relaxation process is concluded to be a result of dislocation nucleation and propagation via dislocation glide initiated by the SPER breakdown.

Finally, the results in Chapter Four have shown that the implant damage proximity to the Si/SiGe interface impacts the degree of relaxation and misfit dislocation density. After a constant anneal time and temperature, 800 ºC for 30 minutes, and varying implant energy (proximity) the misfit dislocation spacing is observed to decrease with increasing proximity. Therefore, exhibiting a higher density and observed relaxation as confirmed by HRXRD measurements. Further analysis using isothermal anneals and PTEM showed that the misfit dislocations are observed to increase in density for the two lower implant energy cases. The

highest energy case, already observed complete relaxation at 30 minutes and exhibits constant misfit dislocation density with further annealing. The PTEM and HRXRD results are consistent and confirm data observed.

In summary, this experiment has determined that the proximity of the initial a-c interface depends significantly on misfit dislocation density and strain relaxation. The closer proximity of the damage to the Si/SiGe interface, the higher the degree of relaxation and higher misfit dislocation density is observed. Additionally, the results in the Chapter Three showed that the end-of-range damage population decreased in conjunction with an increase in misfit dislocations. These results indicate that close proximity of the damage to the interface could influence both trapped interstitial concentration as well as the degree of relaxation. Therefore, it can be inferred that the epilayer interface may be acting as a sink for point defects when the implant damage is placed in close proximity. To confirm this claim, future studies below 800 ºC are recommended to explore the end-of-range evolution and trapped interstitial concentration as a function of damage proximity to the interface to fully understand the role of excess interstitials to the relaxation process.

Compressive Strain Case

Compressive strain experimental structures were grown using Reduced Pressure Chemical Vapor Deposition (RPCVD). Pseodomorphically strained 50 nm $Si_{1-x}Ge_x$ was deposited on Si (001) substrate with alloy compositions of 0, 16, 22, and 26 % germanium. The structures were then implanted with Si^+ at an energy of 5, 12, or 18 keV and a fluence of $1x10^{15}$ atoms/cm^2 to generate continuous amorphous layers confined within the strained layer. Next, isothermal and isochronal anneals were performed in a quartz-tube furnace under an inert N_2 ambient environment. These experiments were carried out to determine specific factors that affect the relaxation process.

The results for the compressive case study are discussed in Chapter Five and Six and are summarized here. First, the a-c interface roughens due to compressive strain and this roughness increases when the magnitude of strain is increased. The roughness is a strain effect previously reported in both compressively strained Si [Bar04] and in metastable SiGe films [Ang07, Lee93]. It is also similar to the effect seen in compressively strained epitaxial layers grown via deposition techniques [Sro89]. With increasing initial strain in the film, there is more strain energy to compensate by decreasing elastic energy. The balance of these energies yields a minimum wavelength of the roughness for the a-c interface. This roughness was not observed in the tensile case.

Defects are nucleated during SPER by the competition of the different direction growth fronts. Using $g \cdot b$ analysis, these defects were determined to be hairpin dislocations with Burgers vector of a/2 <110> which were first observed by T. Sands [San84]. These defects were later observed in metastable SiGe SPER [Ang07] and in Si samples implanted with high dose Ge^+ to form SiGe via SPER [Cri96]. The a-c interface in these other structures also exhibited roughness similar to these observations.

In relation to the tensile case discussed in previous chapters, the critical strain for SPER breakdown is much lower in compression. And the mechanism by which defects are nucleated is altered. Additionally, no stacking faults were generated in the compressively strained SiGe films unlike the tensile Si counterpart. However, the dominant factor in the defect nucleation in the strained SiGe samples is the roughening of the a-c interface nucleating defects as the facets meet.

Experimental results have also shown hairpin dislocation density is stable and not a function of temperature over the range studied. It does not correlate, therefore, with the strain relaxation observed via XRD which increases as the anneal temperature is raised. The defects

nucleate at the meeting of the facets of the rough a-c interface and propagate towards the surface with the advancing front. It is also observed that these defects do not glide down to the epitaxial interface. The defective layer is contained between the depth at which defect nucleation occurred and the surface. At lower strain, there lies a defect-free layer which retained its initial strain with a highly defective layer near the surface which is fully relaxed. The proximity experiment results discussed how this defect-free layer is influenced by both initial magnitude of strain and the proximity of the a-c interface to the epitaxial interface.

The relaxation of the regrown layer is quite different when the strain is in a state of compression versus tension. For the compressive state, results have shown that defects were nucleated when the competing growth fronts of the rough a-c interface meet during SPER. The a-c interface roughness is shown to increase with increasing initial strain. The defect density also shows a similar trend. Therefore, it is evident that there is a correlation between a-c interface roughness and defect density. These defects are also stable and reach saturation beyond a critical strain and implant depth. The proximity experiment shows that the defect nucleation is highly dependent on both strain and proximity of the implant to the epilayer interface. Additionally, lower strain and shallower implant depths cause the formation of a localized layer of defects that do not extend down to the epitaxial interface even after further annealing. While this region above the a-c interface regrows with poor crystalline quality and an abundance of hairpin dislocations, these dislocations remain confined within the regown region and do not affect the strain at the Si/SiGe interface. The hairpin dislocations do, however, cause some localized strain relaxation as observed with XRD measurements. At higher strain (above 22% Ge) and implant energies (above 12 keV), the entire SiGe layer is defective and further strain relaxation is observed. Overall, this is contrary to the tensile case where the regrowth defects

always extend down to the epitaxial interface after regrowth regardless of the initial a-c interface position. These regrowth related defects were observed to nucleate misfit dislocations and cause further relaxation than annealing alone (no implants).

It is plausible to conclude that the critical thickness is varied when the implant is contained within the layer versus one that is performed though the layer. This is likely due to the localized strain increase due to implantation and the regrowth taking place within the strained layer itself. Additionally, when implants are performed within the layer, the proximity of the a-c interface placement with respect to the epitaxial interface plays an important role in both defect nucleation and strain relaxation. Furthermore, the assumptions upon which the M-B critical thickness was calculated cannot be applied to the present case. The relaxation mechanism itself is quite different as discussed.

In summary, prior works have extensively studied strain relaxation and SPER in supercritical SiGe films where implants were conducted through the Si/SiGe interface. However, the effect of implant proximity to the Si/SiGe interface and how it affects defect nucleation and relaxation for implants within the layer was not well understood. This work investigates this effect and has deemed it inappropriate to apply Matthews-Blakeslee's criteria to these sample conditions. Matthew-Blakeslee's criteria are calculated under equilibrium conditions. However, once the implant is conducted within the strained layer, it is a non-equilibrium process and Matthews-Blakeslee criteria cannot be applied. Also, prior work has been deficient in determining the relationship between defect microstructure and strain relaxation upon SPER. This work has shown a correlation between defect density and strain relaxation. Additionally, the results in this study conclude that the a-c interface roughening is the dominant factor in the defect nucleation and that the defects are a/2<110> type dislocations.

Comparison

The relaxation of the regrown layer is quite different when the strain is in a state of compression versus tension. The main reasoning behind the difference is in the manner in which the defects are nucleated. The advancing a-c interface is planar under tension and is observed to roughen under compression. This roughness was observed to increase with increasing initial strain value. Thus, the mechanism of defect nucleation differed for each case. In tension, it was observed to be caused by the formation of regrowth related defects. These defects then glide down to the Si/SiGe interface and promote further growth of misfit dislocations. In compression, the defects nucleated when differently oriented growth fronts meet. These defects are perfect dislocations and are termed hairpins and have been observed previously. In both cases, the defects were observed to propagate below the original a-c interface; the first observations of such an event. In tension, the defects are concluded to be mediated via dislocation glide mechanism. In compression, it is hypothesized to be dislocation climb. Further analysis is needed to confirm this claim.

Future Work

Dissolution rate of {311} defects under tension. In this work, defect evolution of the EOR under tensile strain was observed to be altered. Under tensile strain, {311}s are stable after 45 minutes at 800 °C while they are only stable in unstrained Si for 5 minutes at this temperature. Thus, the dissolution rate of {311} dislocation seems to have been affected by tensile strain. It is known that interstitials are more stable in tension than in compression. Antonell et al. showed that increasing biaxial tensile strain significantly reduces the activation energy of interstitial formation [Ant90]. In order to study the true effect of tensile strain on {311} dissolution, utilization of a strained structure without the close proximity of a sink, as exists in this work, is needed.

Confirmation of climb mechanism in compression. The results from the samples in compression suggest that the hairpin dislocations are propagating towards the epilayer interface via dislocation climb motion. Climb is mediated though diffusion of point defects. One method to confirm both the dislocation climb mechanism and the role of excess interstitials to the relaxation process under compression is to design an experiment such that the net interstitial population is altered yet the implant species and a-c interface depth is kept constant. This experiment can be carried out by the use of low temperature implantation. Lowering the implant temperature increases the amorphization efficiency thereby producing a deeper a-c interface depth with less energy compared to an equivalent implant carried out at room temperature. Designing the experiment in this manner will not increase complexity of the experiment by introducing additional variables whose effect cannot be determined. This was found to be the case with the $B_{18}H_{22}$ cluster implant experiment discussed in Appendix C.

APPENDIX A
STRESS-STRAIN CONVERSION

The experimental results in this work may be discussed in terms of either stress or strain. The selection of strain as the metric of choice is preferred since it can be directly calculated from XRD results and using Bragg's law to obtain lattice parameters of the layer and substrate. In the event the reader would like to compare the results herein to a work that presents results in terms of stress, the equivalent stress values in GPa for both the strained Si and strained SiGe structures are presented in Tables A-1 and A-2, respectively.

Table A-1. Stress-strain conversions for strained Si on $Si_{1-x}Ge_x$.

	Strain	*Stress*
Si on Si0.9Ge0.1	0.0037	0.62 GPa
Si on Si0.8Ge0.2	0.0074	1.25 GPa
Si on Si0.7Ge0.3	0.0110	1.86 GPa

Table A-2. Stress-strain conversions for strained $Si_{1-x}Ge_x$ on Si.

	Strain	*Stress*
$Si_{0.84}Ge_{0.16}$ on Si	-0.0065	-1.10 GPa
$Si_{0.78}Ge_{0.22}$ on Si	-0.0090	-1.52 GPa
$Si_{0.74}Ge_{0.26}$ on Si	-0.0107	-1.81 GPa

APPENDIX B
AMORPHOUS-CRYSTALLINE INTERFACE RELAXATION

Strained 50 nm $Si_{1-x}Ge_x$ was deposited on Si (001) substrate with alloy compositions 26% Ge and strained Si was deposited on $Si_{1-x}Ge_x$ virtual substrate with alloy composition of 30% Ge. The as-grown structures were characterized using TEM and XRD techniques in order to ensure proper growth of strained films. Post growth, the structures were implanted with Si^+ with an energy of 12 keV at a fluence of $1x10^{15}$ atoms/cm^2 to generate a 30 nm continuous amorphous layer confined within the strained layer. Anneals were performed in a quartz-tube furnace under an inert N_2 ambient environment.

The experiment consisted of an isothermal study at 500 ºC performed to investigate defect nucleation and propagation in the strained film. Anneal times were 15, 30, and 45 minutes. With these times and temperature, the regrowth velocity is slow enough that the amorphous-crystalline (a-c) interface will be captured before complete regrowth has taken place. This allows observation of defects as they nucleate and grow with the use of XTEM. The result from this experiment is discussed in Chapter five. Additionally, a preanneal of 400°C for 60 minutes was conducted prior to the 500ºC anneal to relax and planarize the a-c interface before initiation of SPER, this is also called a relaxation anneal. XTEM micrographs of the preanneal, shown in Figure B-1, planarized the a-c interface prior to regrowth. Similar low temperature preanneals, also have been conducted to planarize the a-c interface in prior work [Kin03, Ban00]. The roughness of the a-c interface post regrowth is similar to samples annealed without the relaxation anneal. These results conclude that the relaxation anneal prior to SPER does not change the a-c interface morphology.

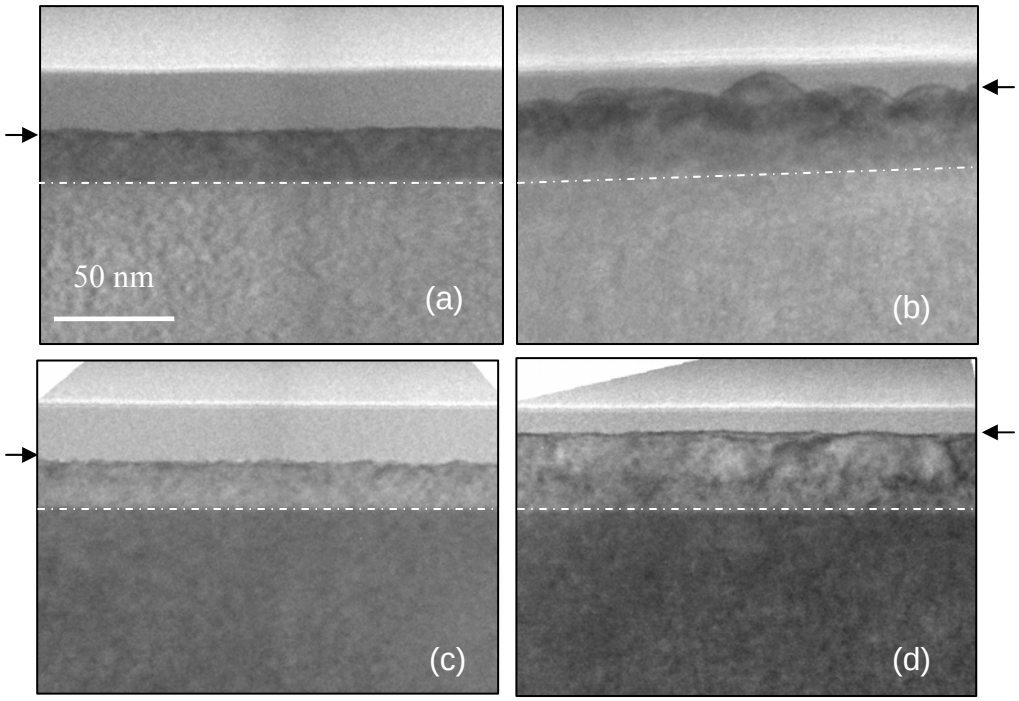

Figure B-1. XTEM of samples implanted with $B_{18}H_{22}$ cluster (a) 26% Ge annealed for 400 ºC 60 minutes (b) 26% Ge annealed for 400 ºC 60 minutes followed by 500 ºC 30 minutes (c) 30% Ge annealed for 400 ºC 60 minutes (d) 30% Ge annealed for 400 ºC 60 minutes followed by 500 ºC 30 minutes. Arrows indicate a-c interface and hatched white lines indicate epitaxial interface.

APPENDIX C
BORON CLUSTER EXPERIMENT: EFFECT OF EOR POPULATION

P-type devices are traditionally implanted first with a Pre-Amorphizing Implant (PAI) prior to boron implantation to avoid channeling of the smaller boron atom through the silicon lattice thus achieving shallower junctions. Octadecaborane ($B_{18}H_{22}$) cluster ion enables the elimination of the PAI step due to its ability to amorphize the implanted region while achieving shallower junctions [Heo06, Kru06, Sek07]. The goal of using this cluster ion is to reduce the End of Range (EOR) damage from the PAI which causes leakage currents and enhanced diffusion.

The octadecaborane was implanted into the highest tensile (Si) and highest compression (SiGe) samples. The implant was carried out at a fluence of $1 \times 10^{15}/cm^2$ at an equivalent energy of 4 keV. This implant generated an amorphous layer ~ 15 nm in depth, XTEM shown in Figure C-1, the same depth as the 5 keV conventional Si^+ implant as discussed in the experimental chapters of this work. The as-implanted amorphous-crystalline (a-c) interface is not as planar as a conventional implant. It is observed to be quite non-uniform as shown in a high resolution XTEM image, Figure C-2. Rough initial a-c interface has been shown by previous work to nucleate defects upon regrowth [San84]. Since the strain samples in this work already nucleate regrowth related defects, it is difficult to separate out the rough a-c interface versus the strain contribution.

PTEM images, taken under g_{220} WBDF conditions, are presented in Figure C-3 for the highest tensile and highest compressive case implanted with either 5 keV Si^+ or $B_{18}H_{22}$ cluster implants and annealed at 800 °C for 30 minutes. The misfit dislocation spacing (or density) difference between the implant conditions is not significant enough to determine whether the boron cluster case observed a reduction. This is true for both strain cases. Analysis using XRD

is used to further study this difference. The degree of relaxation obtained from lattice parameters measured via XRD is shown in Figure C-4. In compression, according to XRD results, no difference is degree of relaxation is observed. However, in tension, the conventional implant undergoes a higher degree of relaxation than the boron cluster case. This difference is not noticeable in the PTEM images, the difference between the two cases should exhibit an average misfit spacing difference of ~30 nm. Furthermore, from results presented in Chapter Four, the effect of excess interstitials to the degree of relaxation is enhanced with closer proximity to the Si/SiGe layer. To fully understand and determine a difference, the B cluster implant must be placed closer to the epilayer interface at a proximity where further relaxation was observed.

In summary, the highest tensile and highest compressive samples were implanted with either conventional Si^+ or B^+ cluster implant to yield amorphous layers of the same depth. The B cluster implant was used to reduce the EOR, thus reducing the amount of excess interstitials available to contribute to relaxation. The results show inconclusive data, the difference in degree of relaxation and misfit density is not significant enough to determine an affect. The implant needed to be generated closer to the interface where the relaxation and misfit density was enhanced (refer to proximity results in chapters Four and Six). To fully understand the dependence of interstitial population to the relaxation process, an ideal experiment would involve same species implantation with identical a-c interface depth while changing the net interstitial population. Additionally, implanting boron into the strained samples adds an additional variable to the experiment, whose influence is difficult to separate out.

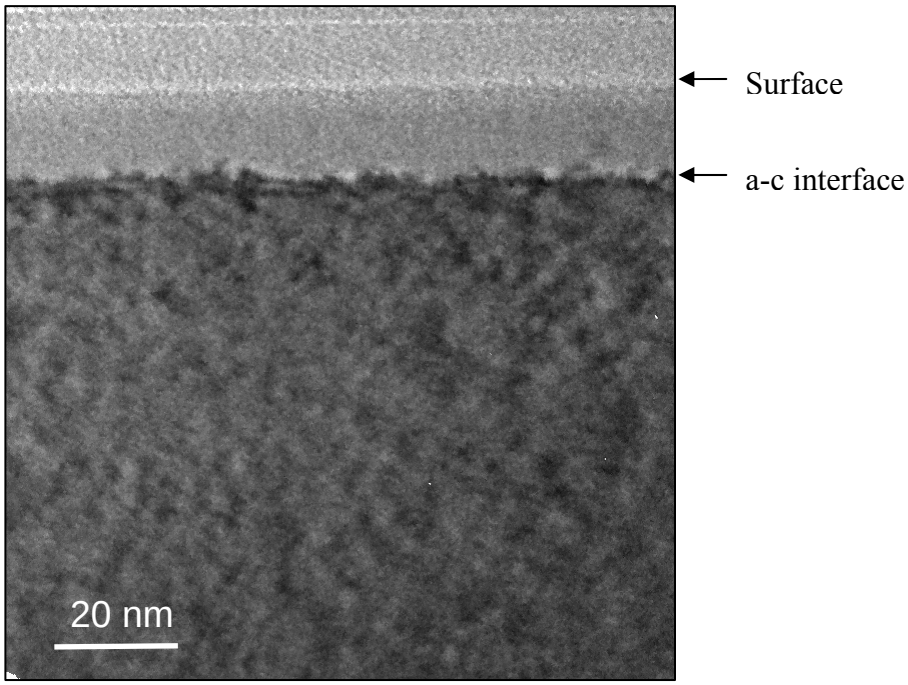

Figure C-1. XTEM of as-implanted with $B_{18}H_{22}$ cluster at equivalent energy of 4 keV into Si (100) substrate.

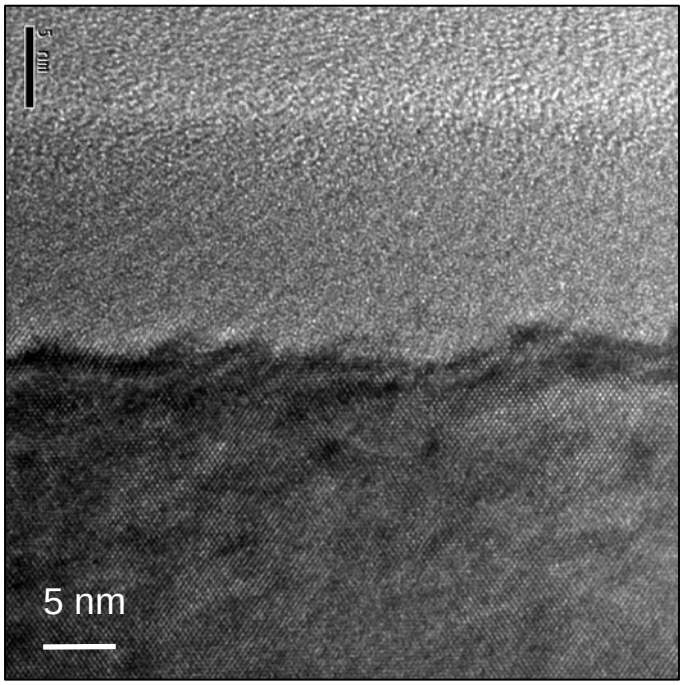

Figure C-2. High-resolution XTEM of as-implanted $B_{18}H_{22}$ at equivalent energy of 4 keV into Si (100) substrate showing a rough a-c interface.

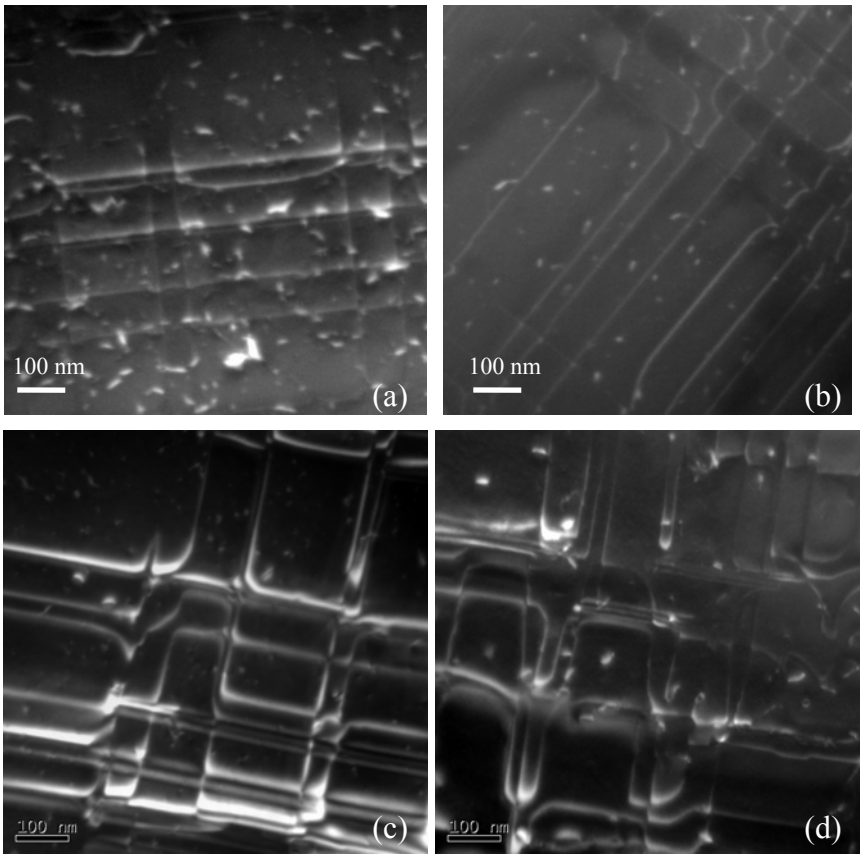

Figure C-3. PTEM images of (a) strained $Si_{0.74}Ge_{0.26}$ on Si implanted with 5 keV Si^+ and (b) implanted with $B_{18}H_{22}$ and of (c) strained Si on $Si_{0.7}Ge_{0.3}$ implanted with 5 keV Si^+ and (d) implanted with $B_{18}H_{22}$. All samples annealed at 800 ºC for 30 minutes.

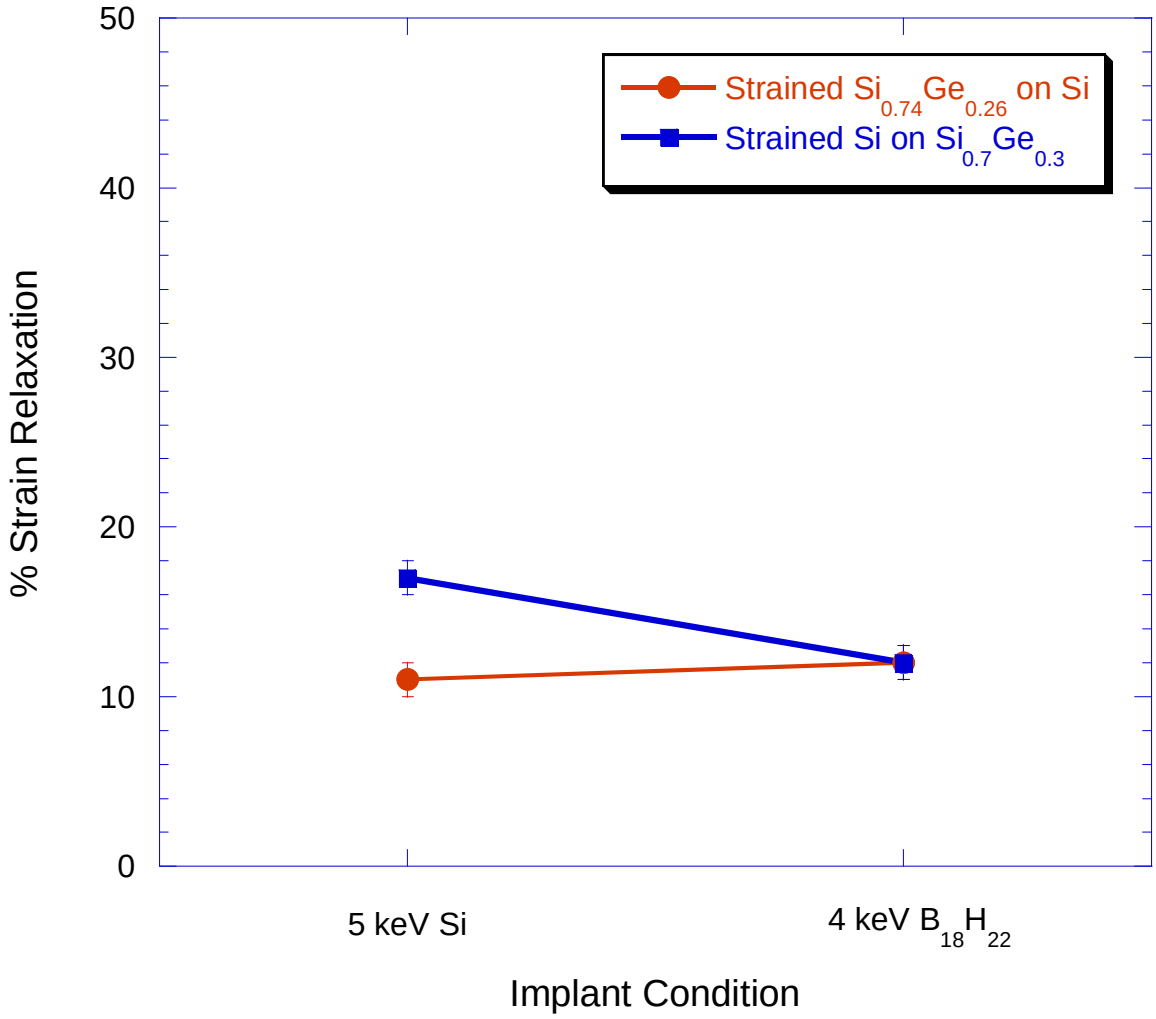

Figure C-4. Strain relaxation quantified using XRD data for highest tensile and compressive strain samples implanted with 5 keV Si^+ and 4keV equivalent $B_{18}H_{22}$ annealed for 30 minutes at 800 °C.

LIST OF REFERENCES

[Alb95] M. Albrecht, S. Christiansen, H.P. Struck, Phy. Status Solidi A, 150, 453 (1995)

[Ale68] H. Alexander and P. Haasen, Solid State Phys. 22, 27 (1968)

[Ang07] D. D'Angelo, A. M. Piro, A. Terrasi, M. G. Grimaldi, S. Mirabella, and C. Bongiorno, J. Appl. Phys. 101, 103508 (2007)

[Ant90] A. Antonelli and J. Bernholc. Mater. Res. Soc. Symp. Proc. 163, 523 (1990)

[Ant96] M. J. Antonell, K. S. Jones, and T. E. Haynes, J. Appl. Phys. 79, 7646 (1996)

[Ban00] H. Banisaukas. PhD. Thesis. University of Florida (2000)

[Bar83] W. J. Bartels, J. Vac. Sci. Tech. B1, 338 (1983)

[Bar04] W. Barvosa-Carter, M. J. Aziz, A.-V. Phan, T. Kaplan, and L. J. Gray, J. Appl. Phys. 96, 5462 (2004)

[Bea87] J. C. Bean, L. C. Feldman, A. T. Fiory, S. Nakahara, I. K. Robinson, J. Vac. Sci. Technol. A, 2, 436 (1987)

[Bir03] M. Birkholz, Thin Film Analysis by X-Ray Scattering, Wiley-Vch, Germany, 2003, pp. 297-311

[Bon98] C. Bonafos, D. Mathiot, and A. Claverie. J. Appl. Phys. 83, 3008 (1998)

[Bul79] C. Bull, P. Ashburn, G. R. Booker, K. H. Nickholas, Sol. State Electron 22, 95 (1979)

[Cap92] M. A. Capano, Phys. Rev. B, 45, 11768 (1992)

[Cha05] V. Chan, K. Rim, M. Ieong, S. Yang; R. Malik, Y. W. Teh, M. Yang, Qiqing, Custom Integrated Circuits Conference, 2005. Proceedings of the IEEE, pp. 667, 18-21 Sept. 2005

[Che74] D. Cherns, PhD dissertation, University of Cambridge (1974)

[Che04] C.-H. Chen, T. L. Lee, T. H. Hou, C. L. Chen, C. C. Chen, J. W. Hsu, K. L. Cheng, Y. H. Chiu, H.J. Tao, Y. Jin, C. H Diaz, S. C. Chen, M.-S. Liang, VLSI Technology, 2004. Digest of Technical Papers, pg. 56, 15-17 June 2004

[Chi89] B. T. Chilton, F. J. Robinson, and D. A. Thompson, Appl. Phys. Lett., 54(1) 42 (1989)

[Chr81] L. A. Christel, J. F. Gibbons, and T. W. Sigmon, J. Appl. Phys., 52(11), 7143 (1981)

[Cof00] S. Coffa, S. Libertino, and C. Spinella, Appl. Phys. Lett., 76(3), 321 (2000)

[Cor96] F. Corni, S. Frabboni, R. Tonini, and G. Ottaviani, J. App;. Phys., 79(7) 3528 (1996)

[Cri96] F. Cristiano, A. Nejim, B. de Mauduit, A. Claverie and P. L. F. Hemment, Nuclear Instruments and Methods in Physics Research Section B: Beam Interactions with Materials and AtomsVolume 120, Issues 1-4, , Proceedings of the E-MRS '96 Spring Meeting Symp. I on New Trends in Ion Beam Processing of Materials, 2 December 1996, pg. 156

[Cri00] F. Cristiano, J. Grisolia, B. Colombeau, M. Omri, B. de Mauduit, A. Claverie, L. F. Giles, and N. E. B. Cowern. J. Appl. Phys. 87, 84 (2000)

[Cro04] R. T. Crosby, K. S. Jones, M. E. Law, A. F. Saavedra, J. L. Hansen, A. N. Larsen and J. Liu, Mat. Res. Soc. Symp. Proc. 810 (2004)

[Cro05] R. T. Crosby, PhD. Thesis. University of Florida (2005)

[Cse76] L. Csepregi, J. W. Mayer and T.W. Sigmon. Appl. Phys. Lett., 29(2), 92 (1976)

[Cse78] L. Csepregi, E.F. Kennedy, J.W. Mayer and T.W. Sigmon. J. Appl. Phys., 49(7), 3906 (1978)

[Cow94] N. E. B. Cowern, G. F. A. van de Galle, P. C. Zalm, and D. W. E. Vabdenhoudt. Appl. Phys. Lett. 65, 2981 (1994)

[Dea73] G. Dearnaley, J. H. Freeman, R. S. Nelson and J. Stephen. Ion Implantation (1973)

[Dis64] J. P. Dismukes, L. Ekstrom, and R. J. Paff, J. Phys Chem., 68(10), 3021 (1964)

[Dod87] B. W. Dodson and J. Y. Tsao, Appl. Phys. Lett., 51, 1325 (1987)

[Dod88] B. W. Dodson and J. Y. Tsao, Phy. Rev. B. 38, 12383 (1988)

[Dro82] R. Drosd and J. Washburn, J. Appl. Phys. 53, 397 (1982)

[Eag94] D. J. Eaglesham, P. A. Stolk, H.-J. Gossmann, and J. M. Poate, Appl. Phys. Lett., 65(18), 2305 (1994)

[Edi75] J. W. Edington. Practical Electron Microscopy in Materials Science. Ed. 4, Macmillian, London, 1975, pg. 6

[Ell95] R. G. Elliman P. Kringhoj, and J. M. Glasko, Nuclear Inst. And Methods B, 96, 276 (1995)

[Ell96] R. G. Elliman, and W. C. Wong, Appl. Phys. Lett. 69 (18) 2677 (1996)

[Fah89] P. M. Fahey, P. B. Griffin, and J. D. Plummer, Rev. Mod. Phys. 61, 289 (1989)

[Far86] B. Y. Farver, Y. L. Iunin, and V. I. Nititenko, Phys. Status Solidi, 97, 469 (1986)

[Few82] P. F. Fewster, J. Appl. Cryst. 15, 275 (1982)

[Fit91] E. A. Fitzgerald, Y.-H. Xie, M. L. Green, D. Brasen, A. R. Kortan, J. Michel, Y.-J. Mii, and B. E. Weir, Appl. Phys. Lett. 59, 811 (1991)

[Fri87] I. J. Fritz, Appl. Phys. Lett., 51(14), 1080 (1987)

[Fre87] L. B. Freund: J. Appl. Mech. 54, 553 (1987)

[Gai00] P. I. Gaiduk, A. Nylandsted Larsen and J. Lundsgaard Hansen, Thin Solid Films, 367, 120 (2000)

[Gla97] J. M. Glasko, and R. G. Elliman, J. D. Fitz Gerald and P. Kringhoj, Nuclear Inst. And Methods B, 127/128, 397 (1997)

[Gil99] L. F. Giles, M. Omri, B. de Mauduit, A. Claverie, D. Skarlatos, and D. Tsoukalas, Nuclear Inst. and Meth. B, 148, 273 (1999)

[Gus01] E. Gusev, D. Buchanan, E. Cartier, A. Kumar, D. DiMaria, S. Guha, A. Callegari, S. Zafar, P. Jamison, D. Neumayer, M. Copel, M. Gribelyuk, H. Okorn-Schmidt, C. D'Emic, P. Kozlowski, K. Chan, N. Bojarczuk, L.-A. Rannarsson, P. Ronsheim, K. Rim, R. Fleming, A. Mocuta, and A. Ajmera, Electron Devices Meeting, 2001. IEDM Technical Digest, pg. 20 (2001)

[Gut98] M. Yu. Gutkin, K. N. Mikaelyan, and I. A. Ovid'ko, Phys. Solid State, 40, 1864 (1998)

[Gut01a] M. Yu. Gutkin, K. N. Mikaelyan, and I. A. Ovid'ko, Phys. Solid State, 43, 42 (2001)

[Gut01b] A. F. Gutierrez.. M.S. Thesis. University of Florida (2001)

[Hag78] W. Hagen, H. Strunk, Appl. Phys. Lett. 17, 85 (1978)

[Hay92] T. E. Haynes and O. W. Holland. Appl. Phys. Lett. 61, 61 (1992)

[Heo06] S. Heo, D. Lee, H. T. Cho, W. A. Krull, and H. Hwang, Ion Implantation Technology 2006, Marseille, France, 11-16, June 2006

[Hir68] J. P. Hirth and J. Lothe, Theory of Dislocations, McGraw-Hill, New York, 1968

[Hof74] W. K. Hofker, H. W. Werner, D. P. Oostoek, and N. J. Koeman. Appl. Phys. Lett. 4, 25 (1974)

[Hon92] Q. Z. Hong, J. G. Zhu, and J. W. Mayer, J. Appl. Phys. 71, 1768 (1992)

[Hor05] M. Horstmann, A. Wei, T. Kammler, J. Hntschel, H. Bierstedt, T. Feudel, K. Frohberg, M. Gerhardt, A. Hellmich, K. Hempel, J. Hohage, P. Javorka, J. Klais, G. Koerner, M. Lenski, A. Neu, R. Otterbach, P. Press, C. Reichel, M. Trentsch, B. Trui, H. Salz, M. Schaller, H. J. Engelmann, O. Herzog, H. Ruelke, P. Hubler, R. Stephan, D. Greenlaw, M. Raab, N. Kepler, Electron Devices Meeting, 2005. IEDM Technical Digest, pg. 233, 5-7 Dec. 2005

[Hou91] D.C. Houghton, J. Appl. Phys. 70, 2136 (1991)

[Hul89] R. Hull, J. C. Bean, D. J. Werder, and R. E. Leibenguth, Phy. Rev. B. 40, 1681 (1989)

[Hul93] R. Hull, J. C. Bean, L. J. Peticolas, D. Bahnck, B. E. Weir, and L. C. Feldman, Appl. Phys. Lett. 73, 7407 (1993)

[Hwa91] D. M. Hwang, S. A. Schwarz, T. S. Ravi, R. Bhat, and C.Y. Chen, Phy. Rev. Lett. 66, 739 (1991)

[Ima83] M. Imai, K. Sumino, Philos. Mag A, 47, 599 (1983)

[Jai90] S. C. Jain, J.R. Willis, R. Bullough, Adv. in Phys. 39(2), 127 (1990)

[Jon88] K. S. Jones, S. Prussin and E.R. Weber. Appl. Phys. A. (USA), 34, 1 (1988)

[Jon97] K. S. Jones, K. Moller, J. Chen, and M. Puga-Lambers, J. Appl. Phys., 81 (9), 6051 (1997)

[Kas75] E. Kasper and H.J. Herzog, Thin Solid Films, 44, 357 (1975)

[Kin03] A.C. King. M.S. Thesis. University of Florida (2003).

[Koe01] S.J. Koester, K. Rim, J.O. Chu, P.M. Mooney, and J.A. Ott, Appl. Phys Lett. 79, 2148 (2001)

[Kri95a] P. Kringhoj, R. G. Elliman, M. Fyhn, S. Y. Shiryaev and A. Nylandsted Larsen, Nuclear Inst. And Methods B, 106, 346 (1995)

[Kru06] W. A. Krull, B. Haslam, T. Horsky, K. Verheyden, and K. Funk, Ion Implantation Technology 2006, Marseille, France, June 2006

[Kuk83] Y. Kuk, L. C. Feldman, and P. J. Silverman, Phys. Rev. Lett. 50, 511 (1983)

[Lam99] E. Lampin, V. Senez, and A. Claverie. J. Appl. Phys. 85, 8137 (1999)

[Lee93] C. Lee, T. E. Haynes, and K. S. Jones, Appl. Phys. Lett. 62(5), 501 (1993)

[LeG93] F. K. LeGoues, P.M. Mooney, J. Tersoff, Phys. Rev. B, 40, 1681 (1993)

[Lei01] C. W. Leitz, M. T. Currie, A. Y. Kim, J. Lai, E. Robbins, E. A. Fitzgerald, and M. T. Bulsara, J. Appl. Phys. 90, 2730 (2001)

[Lie93] D. Y. C. Lie, A. Vantomme, F. Eisen, T. Vreeland, Jr., M.-A. Nicolet, T.K. Carns, V. Arbet-Engels, and K. L. Lang. J. Appl. Lett. 74, 6039 (1993)

[Lie95] D. Y. C. Lie, J. H. Song, A. Vantomme, F. Eisen, M.-A. Nicolet, N. D. Theodore, T. K. Carns, and K. L. Wang, J. Appl. Phys. 77, 2329 (1995)

[Lin03] C. D. Lindfors. PhD. Thesis. University of Florida (2003)

[Liu95] J. Liu, M.E. Law, and K.S. Jones, Solid-State Electronics, 38(7), 1305 (1995)

[Mar87] P. M. J. Marée, J.C. Barbour, J. F. van der Veen, K. L. Kavanagh, C. W. T. Bulle-Lieuwma, and M. P. A. Viegers, J. Appl. Phys. 62, 4413 (1987)

[Mass90] T. B. Massalski, Binary Alloy Phase Diagrams, ASM International, Materials Park, OH (1990)

[Mat74] J. W. Matthrews and A. E. Blakeslee, J. Cryst. Growth, 29, 273 (1974)

[Mat91] M. Matsuura, J. M. Tonnerre, and G. S. Cargill III, Phys. Rev. B, 44, 3842 (1991)

[Mau94] B. de Mauduit, L. Laanab, C. Bergaud, M.M. Faye, Nuclear Inst. And Methods B, 84, 955 (1994)

[Moo65] G. E. Moore, Electronics 38, 114-117 (1965)

[Moo94] P. M. Mooney, F.K. LeGoues, J. Tersoff, J. Appl. Phys. 75, 3968 (1994)

[Mil05] A. Mills, III-Vs Review 18 (7), 28 (2005)

[Nar82] J. Narayan, J. Appl. Phys. 53, 8607 (1982)

[Nay96] D. K. Nayak, K. Goto, A. Yutani, J. Murota, and Y. Shiraki, IEEE Trans. Electron Devices 43, 1709 (1996)

[Nod00] T. Noda, S. Odanaka, and H. Umimoto. J. Appl. Phys. 88, 4980 (2000)

[O'Ra96] C. O'Rifeartaigh, R. C. Barklie, A. Nylandsted Larsen, F. Priolo, G. Franzo, G. Lulli, M. Bianconi, J. K. N. Lindner, F. Christiano, and P. L. F. Hemment. Nucl. Instr. Meth. Phys. Res. B. 120, 165 (1996)

[Ols85] G. L. Olson, Mat. Res. Soc. Proc., 35, 25 (1985)

[Ols88] G. L. Olson and J. A. Roth, Mat. Sci. Reports, 3, 1 (1988)

[Pat66] J. R. Patel and A. R. Chaudhuri, Phys. Rev, 143, 601 (1966)

[Pan96] G. Z. Pan, K. N. Tu, and S. Prussin, Appl. Phys. Lett., 68(12), 1654 (1996)

[Peo85] R. People and J. C. Bean, Appl. Phys. Lett. 47, 322 (1985)

[Pai91] D. C. Paine, N. D. Evans, and N. G. Stoffel, J. Appl. Phys, 70, 4278 (1991)

[Phe04] M. S. Phen, "The Effects of Stress on Dopant Activation and Defect Morphoogy," Semiconductor Research Corporation Annual Review, Raleigh, NC, 2004

[Phe05] M. S. Phen, R. T. Crosby, K. S. Jones, M. E. Law, J. L. Hansen, A. N. Larsen, Mat. Res. Soc. Symp. Proc. 864 (2005)

[Phe06] M. S. Phen, V. Craciun, K. S. Jones, J. L. Hansen and A. N. Larsen, Nuclear Inst. And Methods B, 253, 22 (2006)

[Pie04] U. Pietsch, V. Holy, and T. Baumbach, High-Resolution X-Ray Scattering: From Thin Films to Lateral Nanostructures, Springer-Verlag, New York, 2nd ed., 2004, p.205

[Poa84] J. M. Poate and J.S. Williams, Ion Implantation and Beam Processing, Academic Press, New York, 1984, p. 27

[Raa99] I. J. Raaijmakers, H. Sprey, A. Storm, T. Bergman, J. Italiano, and D. Meyer, J. Vac. Sci. Technol. B 17, 2311 (1999)

[Rab00] J. Rabier and J. L. Demenet, Phys. Stat. Sol., 222, 63 (2000)

[Rea53] W.T. Read, Dislocation in Crystals, McGraw-Hill, New York, 1953

[Rod97] A. Rodriguez, T. Rodriguez, A. Kling, J. C. Soares, M. F. da Silva, and C. Ballesteros, J. Appl. Phys. 82, 2887 (1997)

[Sam99] S. B. Samavedam, W. J. Taylor, J. M. Grant, J. A. Smith, P. J. Tobin, A. Dip, and R. Liu, J. Vac. Sci. Tech. B 17, 1424 (1999)

[San84] T. Sands, J. Washburn, R. Gronsky, W. Maszara, D. K. Sadana and G. A. Rozgonyi, Proc. 13th Int. Conf. on Defects in Semiconductors, The Metallurg. Sot. of AIME, Warrendale, PA, 1984, p.531

[Sek07] K. Sekar, W. A. Krull, T. N. Horsky, and D. C. Jacobson, Ion Implantation Technology 2007

[Sin05] D. V. Singh, J. W. Sleight, J. M. Hergenrother, Z. Ren, K. A. Jenkins, O. Dokumaci, L. Black, J. B. Chang, H. Nakayama, D. Chidambarrao, R. Venigalla, J. Pan, W. Natzle, B. L. Tessier, A. Nomura, J. A. Ott, M. Ieong, W. Haensch, Electron Devices Meeting, 2005. IEDM Technical Digest, pg. 505, 5-7 Dec. 2005

[Sin06] D. V. Singh, K. A. Jenkins, J. Sleight, Z. Ren, M. Ieong, W. Haensch, Electron Device Letters, IEEE , vol.27, no.3, pp. 191, March 2006

[Sro89] D. J. Srolovitz, Acta Metl. 38, 621 (1989)

[Ste07] M. Steinert, J. Acker, S. Oswald, K. Wetzig, J. Phys. Chem. C. 111, 2133 (2007)

[Sto95] P. A. Stolk, H. J. Gossmann, D. J. Eaglesham, D. C. Jacobson, J. M. Poate, and H. S. Luftman. Appl. Phys. Lett. 66, 568 (1995)

[Sug01] N. Sugii, J. Appl. Phys. 89, 6459 (2001)

[Sug04] N. Sugii, S. Irieda, J. Morioka, and T. Inada, J. Appl. Phys. 96, 261 (2004)

[Tam96] M. Tamura, Appl. Phys. A, A63 (2), 359 (1996)

[Tho04] S. E. Thompson, M. Armstrong, C. Auth, S. Cea, R. Chau, G. Glass, T. Hoffman, J. Klaus, M. Zhiyong, B. Mcintyre, A. Murthy, B. Obradovic, L. Shifren, S. Sivakumar, S. Tyagi, T. Ghani, K. Mistry, M. Bohr, Y. El-Mansy, Electron Device Letters, IEEE , vol.25, no.4, pg. 191, (2004)

[Tho06] S. E. Thompson, G. Sun, Y. S. Choi, and T. Nishida, Electron Devices, IEEE Transactions, vol.53, no.5, pp. 1010 (2006)

[Tsa87] J.Y. Tsao, B.W. Dodson, S.T. Picreaux, D.M. Cornelison, Phy. Rev. Lett. 59, 2455 (1987)

[Tup90] C. G. Tuppen, C. J. Gibbings, M. Hockly, S. G. Roberts, Appl. Phys. Lett. 56, 54 (1990)

[Uem99] M. Uematsu. Jpn. J. Appl. Phys. 38, L1213 (1999)

[Van63] Van der Merwe, J. Appl. Phys. 34(1), 117 (1963)

[Van05] W. Vandervorst, T. Janssens, B. Brijs, R. Delhougne, R. Loo, M. Caymax, B.J. Pawlak, M. Posselt. Appl. Phys. Lett. 86, 081915 (2005)

[Weg90] W. Wegscheider, K. Eberl, U. Menczigar, G. Abstreiter, Appl. Phys. Lett. 57, 875 (1990)

[Wil96] D. B. Williams and C. B. Carter, Transmission Electron Microscopy, Plenum Press, New York, NY, 1996, pp. 423

[Yon96] I. Yonenaga, K. Sumino, Appl. Phys. Lett. 69, 1264 (1996)

[Yon99] I. Yonenaga, Phys. Status Solidi A. 171, 41 (1999)

BIOGRAPHICAL SKETCH

Michelle S. Phen is the daughter of Shinthong Phen and Ramona Phen. Michelle was raised in Miami, Florida. She attended Barry University in Miami, Florida before transferring to the University in Florida in 2000. In May 2003, she was awarded a B.S. in Materials Science and Engineering Cum Laude with a specialty in Polymers. Upon graduation, she enrolled in graduate school to pursue a PhD. During her graduate studies, she interned at Texas Instruments, Inc (Dallas, Texas) during two separate fall semesters. Her first internship was with the High Performance Analog (HPA) package development group where she worked on failure analysis and development of new package technology. Her second internship was with the Silicon Technology Development group where she worked as a process development engineer on the SiGe and SALICIDE process line. Upon receiving her doctoral degree, she will begin employment at Intel Corporation.